# Direct Numerical Simulations of Boundary Layer Stability for Non-Ideal Fluids

Marios Christofi

Technische Universiteit Delft

# Direct Numerical Simulations of Boundary Layer Stability for Non-Ideal Fluids

by

Marios Christofi

to obtain the degree of Master of Science
at the Delft University of Technology,
to be defended publicly on Thursday February 25, 2021 at 02:00 PM.

| | | |
|---|---|---|
| Student number: | 4823710 | |
| Project duration: | January 15, 2020 – February 25, 2021 | |
| Thesis committee: | Dr. ir. R. Pecnik, | TU Delft, supervisor |
| | Prof. Dr. ir. J. Padding, | TU Delft |
| | Prof. Dr. ir. B. J. Boersma, | TU Delft |
| | Dr. ir. B. Bugeat, | TU Delft |

An electronic version of this thesis is available at http://repository.tudelft.nl/.

TU Delft

# ACKNOWLEDGEMENTS

At the very beginning of this project, I would like to express my honest gratitude to all the people who assisted in the completion of my thesis, through their continuous support and encouragement.

First and foremost, I would like to express my sincere appreciation to my supervisor, Dr. ir. Rene Pecnik for providing the opportunity of working on such an interesting topic. His constant support and willingness to discuss the problems encountered during the completion of this project, have been remarkable.

I would, also, like to thank ir. Simone Silvestri for his input on the programming part of the thesis, which has been extremely important and helpful.

My gratitude goes to Dr. ir. Jie Ren, for his availability and willingness to answer questions relevant to the topic of research.

I am thankful to Benjamin Bugeat and Pietro Carlo Boldini for their contribution, by providing insight on the principles of Linear Stability Theory.

Finally, I would like to extend my gratitude to my friends for making this period more pleasant and my family for their unconditional support during all the stages of my life.

*Marios Christofi*
*Delft, February 2021*

# ABSTRACT

The process in which a smooth laminar flow transits to a chaotic to a chaotic, turbulent state, is a topic of particular interest in the sectors of energy technology and aerodynamics. To study the different paths that can be followed during the transition process, various tools and methods have been developed. A preliminary investigation of the response of a laminar flow to an internal or external disturbance can be performed by applying *Linear Stability Theory* principles. In the recent years, the *Direct Numerical Simulations* of flows offer a more insightful method to study the transition process, since the flow fields are numerically solved using high computational power. Previous research has primarily focused on the stability and transition of *Ideal Gas* flows, with little attention to the effects of a highly *Non-Ideal* behaviour. The present work aims to develop a DNS code that can be used to investigate the stability of compressible boundary layers in the vicinity of the *Widom Line*.

For the initialization of a DNS, a two dimensional base flow profile is required. For the calculation of the base flow, a self-similar solution is obtained, using a `MATLAB` script that has been developed for the purpose of this study. The DNS code is developed in `FORTRAN`. An inviscid characteristic wave analysis is utilized for the implementation of the boundary conditions, along with numerical sponges to avoid reflections. To trigger the instabilities, periodic suction and blowing is incorporated. For the simulations of non-ideal fluids, a thermodynamic table interpolation tool is incorporated. For the validation of the results obtained by the DNS code, an in-house `MATLAB` script is used to for the calculation of the growth rate and fluctuation amplitude profiles using LST.

Initially, the `FORTRAN` code is used on ideal-gas simulations, to investigate how different computational parameters will affect the flow field. The parameters are related to mesh resolution, boundary conditions and numerical sponges.

To investigate the stability of non-ideal fluids, cases of different free-stream temperatures and Eckert numbers are simulated. The free-stream temperature is altered to control the non-ideal gas effects, whereas the Eckert number is used to control the compressibility effects. In general, the flow is stabilized as non-ideal gas and compressibility effects become more prominent. However, a second unstable mode is observed in the case where the temperature profile crosses the pseudo-critical point. This second mode has a higher growth rate of instabilities, compared to the first mode. All the results are validated using the LST predicted profiles.

# CONTENTS

# LIST OF FIGURES

# NOMENCLATURE

**Acronyms**

| | |
|---|---|
| $Pr$ | Prandtl number |
| $Re$ | Reynolds number |
| $Ec$ | Eckert number |
| $Ma$ | Mach number |
| 2D | Two dimensional |
| 3D | Three dimensional |
| DNS | Direct numerical simulations |
| FRBC | Fully-reflective boundary condition |
| LST | Linear stability theory |
| NRBC | Non-reflective boundary condition |
| ODE | Ordinary differential equation |
| PDE | Partial differential equation |
| RK | Runge-Kutta |
| TS | Tollmien-Schlichting |

**Symbols**

| | |
|---|---|
| $\alpha_i$ | Local growth rate |
| $\beta$ | Span-wise wave-number |
| $\boldsymbol{q}$ | Fluctuation vector |
| $\Delta t$ | Time step |
| $\delta$ | Boundary layer thickness order of magnitude |
| $\delta_{99}$ | Boundary layer thickness |
| $\eta$ | Self-similar wall-normal coordinate |
| $\eta_{targ}$ | Sound-sound reflectivity of sponge |

| | |
|---|---|
| $\gamma$ | Ratio of specific heats |
| $\kappa$ | Heat conductivity |
| $\lambda_i$ | Velocity of characteristic waves |
| $\lambda_w$ | Local stream-wise wavelength |
| $\mathscr{L}_i$ | Amplitude variation of characteristic waves |
| $\mu$ | Dynamic viscosity |
| $\nu$ | Kinematic viscosity |
| $\omega_i$ | Angular frequency of perturbation |
| $\rho$ | Density |
| $\sigma$ | Sponge strength |
| $\sigma_{bc}$ | Coefficient for inviscid characteristic boundary conditions |
| $\tau_{ij}$ | Viscous stress tensor |
| $\xi$ | Self-similar stream-wise coordinate |
| $c$ | Speed of sound |
| $C_p$ | Specific heat capacity |
| $E$ | Internal energy |
| $F$ | Dimensionless frequency of perturbation |
| $h$ | Enthalpy |
| $L$ | Length of flat plate |
| $l_0$ | Characteristic length |
| $L_x$ | Stream-wise domain length |
| $L_y$ | Wall-normal domain length |
| $L_z$ | Span-wise domain length |
| $L_{sp}$ | Sponge length |
| $n_x$ | Number of grid points in the stream-wise direction |
| $n_y$ | Number of grid points in the wall-normal direction |
| $n_z$ | Number of grid points in the span-wise direction |
| $p$ | Pressure |

| | |
|---|---|
| $q_j$ | Heat flux vector |
| $R$ | Ideal gas constant |
| $S$ | Sutherland's constant |
| $S_f$ | Grid stretching factor |
| $T$ | Temperature |
| $u$ | Stream-wise velocity |
| $v$ | Wall-normal velocity |
| $w$ | Span-wise velocity |
| $x$ | Stream-wise coordinate |
| $y$ | Wall-normal coordinate |
| $z$ | Span-wise coordinate |

**Superscripts and Subscripts**

| | |
|---|---|
| $\hat{u}$ | Fourier-transformed quantity |
| $u'$ | Fluctuation of a quantity |
| $u^*$ | Dimensional quantity |
| $u_i$ | Imaginary component |
| $u_r$ | Real component |
| $u_s$ | Static quantity |
| $u_t$ | Total quantity |
| $u_\infty$ | Free-stream quantity |
| $u_{max}$ | Maximum value |
| $u_{max}$ | Minimum value |
| $u_{pc}$ | Value at the pseudo-critical point |
| $u_{ref}$ | Reference value |
| $u_{sc}$ | Value at the critical point |
| $u_w$ | Wall quantity |

# 1

# INTRODUCTION

Hydrodynamic stability is a field that has its origins back in the 19$^{th}$ century and aims to study the response of a *laminar* flow to a disturbance of low or moderate amplitude [32]. In general, a disturbance triggers instabilities in the flow field, that might decay and the flow will return to its original state, hence the flow is characterized as *stable*. Another scenario is that the instabilities will keep growing in space and time, making the flow *unstable* and leading to a chaotic state, also referred to as *turbulence*. To illustrate the transition of a flow from laminar to turbulent, figure 1.1 is provided.

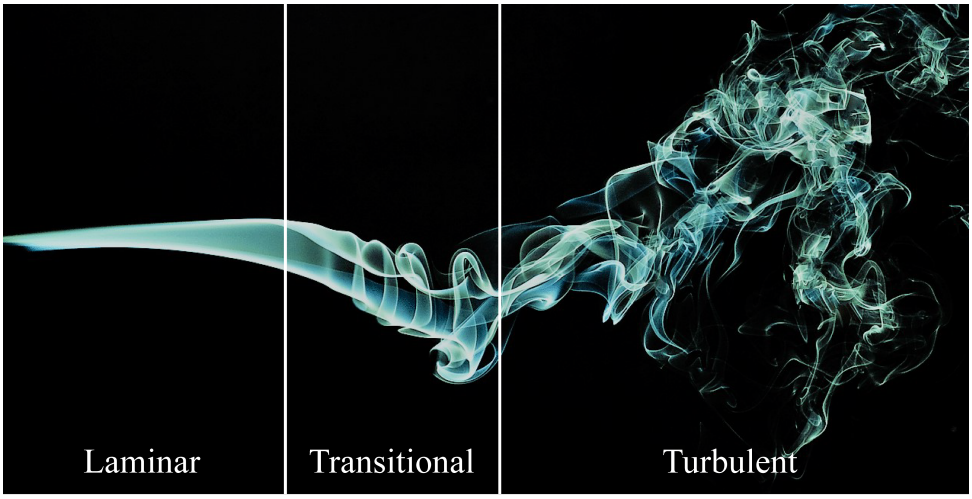


Figure 1.1: Illustration of laminar to turbulent transition of cigarette smoke, labelling the three different zones [36].

In the laminar region the flow is smooth, without the presence of instabilities. Once instabilities start to develop, the flow enters the transitional region, in which instabili-

ties grow in space and time, until secondary mechanisms further destabilize and lead to breakdown further downstream. Breakdown is the final step before the transition to turbulence. In the turbulent zone a chaotic behaviour is exhibited by the flow, accompanied by the presence of multiple vortices.

To mathematically describe the behaviour of any flow, a solution to the flow conservation equations (Navier-Stokes or Euler equations) is required. These equations are non-linear which makes it difficult to obtain an analytical solution. For simple geometries, obtaining an analytical solution might be possible through various assumptions and simplifications on the conservation equations. For more complicated problems, the utilization of numerical methods and computational techniques is required.

To study the turbulent behaviour of flows, researchers use various techniques. One technique employs temporal averaging of the flow variables and incorporates turbulence models to model the turbulent behaviour of flows as a steady-state solution, known as Reynolds-Averaged Navier-Stokes (RANS). Another common technique is Large eddy simulations (LES), which utilizes temporal and spatial averaging of the small features of the flow, while numerically solving the flow conservation equations on coarser grids, resolving the larger flow structures. These techniques are relatively cheap, in terms of computational power, and can be used to model various flow geometries. Although these methods provide information about the turbulent structures of the flow, the origins of turbulence cannot be determined. To obtain an accurate solution of the flow field, a massive amount of computational resources is required for the numerical integration of the conservation equations, through *Direct Numerical Simulations*. This method provides all the information that is required to determine the mechanisms that lead to turbulent transition as well as accurately resolves all flow structures. Since this method is computationally expensive, it is limited to the simulation of simple flow geometries.

Another technique that provides insight the transition to turbulence is *Linear Stability Theory*. This method is used to determine whether an external perturbation will grow inside the flow field, or decay. It is not a computationally expensive method since a linearized form of the conservation equations is solved as an eigenvalue problem to reveal the parameters related to a disturbance that will trigger growth of instabilities in the flow.

In recent research, the field of flow stability, control and transition to turbulence is deemed crucial. This area of research developed rapidly during the last century, in an attempt to delay the transition on airplane wings, since turbulence is the primary source of drag force, eventually increasing fuel costs. Nowadays, the stability of non-ideal fluid flows is an area that remains, mostly, unexplored. The incorporation of non-ideal fluids, like supercritical carbon dioxide in power cycles has a great potential in increasing thermal efficiency; the turbine efficiency of organic Rankine cycles can also improve[2], whereas higher efficiency of mixing and combustion in air breathing and liquid rocket engines can be achieved [38]. Hence the mechanisms of transition in non-ideal fluids need to be further explored and understood, so that broader utilization of such fluids is possible.

## 1.1. LITERATURE REVIEW

The investigation on stability of compressible ideal gas boundary layers was first initiated during the 1940s with the work of Lees and Lin [12], who proved that for an inviscid instability to occur in compressible flows, a generalized inflection point must exist in the velocity profile, similarly to what was stated by the work of Rayleigh for incompressible flows. It was, later, revealed by Mack that for high-speed flows, a second unstable mode occurs at a free-stream Mach number of 4, which belongs to the family of trapped acoustic waves and has a greater growth rate than the first viscous mode [15].

With the introduction of hypersonic vehicles, there was a rise in the interest of high-temperature chemical effects on boundary layer stability, during the 90s. Effects like dissociation and recombination of species, surface ablation, radiation or ionization are referred to as *real gas* effects and might occur at high temperatures. Malik and Anderson [16] investigated the instability of a Mack 10 boundary layer through linear stability analysis and found out that hypersonic effects tend to stabilize the first but destabilize the second Mack's mode. Further research in real gas effects involves the investigation of chemical reaction models by Franco, MacCormack and Lele [7] and Lyttle and Reed [14]. Surface roughness induced transition was investigated by Stemmer et al. [34] whereas surface ablation effects by Mortensen and Zhong [22]. More advanced research was conducted by the incorporation of parabolic stability equations (PSE) by Cang et al. [4], Johnson and Candler[8] and Malik [17]. The investigation of stability was further pursued using direct numerical simulations (DNS) by Marxen et al.(2013) [20], Marxen et al. (2014) [19] and Wang [37].

To model the behaviour of a fluid operating close to the thermodynamic critical point, complex equations of state are utilized. Since the incorporation of supercritical fluids in industrial applications [3] is an emerging topic of research, more interest is drawn on the characterization of turbulence and heat transfer. The first DNS of transcritical boundary layer was performed by Kawai [9] and revealed that turbulent mass flux terms are much higher compared to the case of an ideal gas, in the turbulent kinetic energy equation, for the same free stream Mach number. A review by Pizzarelli [25], showed that future applications, in terms of heat transfer, are limited due to the current knowledge of heat transfer deterioration in supercritical fluids. To investigate the stability of Poiseuille flows of highly non-ideal fluids, Ren et al. [28] performed a recent study based on linear stability analysis. Their work proved that for different thermodynamic regimes, flows might become more stable, unstable or inviscid unstable, compared to ideal gases in the same conditions. Another study conducted by Ren et al. [29], involved the linear stability analysis of non-ideal boundary layers, and the validation using DNS. It was revealed that for a fluid in transcritical conditions, a second unstable mode, with higher growth rate, occurs which is not related to Mack's second mode.

The largest part of literature is primarily focused on the behaviour of ideal gas flows and hypersonic or high temperature effects, which are more relevant in the sector of aerospace engineering. In the field of energy, examining the real gas effects on flow stability has more value, which serves as the motivation behind the present study.

## 1.2. RESEARCH OBJECTIVE

The primary focus of the present study is the development of a FORTRAN code that can be utilized for the direct numerical simulations of supercritical carbon dioxide boundary layers, for the investigation of transitional behaviour. Through this study, knowledge is gained on the optimal computational parameters that can be used for the setup of a DNS code. The work of Ren et al. [29] is used as the primary reference for the validation of the results presented.

By modifying an existing in-house DNS code that is used for the simulation of fully developed turbulent channel flows, a DNS code that can be used for boundary layers is developed. To modify the existing code, new boundary conditions, computational sponges and thermodynamic table interpolation tools are implemented.

To test the resulting code, the stability of an ideal gas boundary layer is investigated, by varying computational parameters and determining the optimal values that can be used for the simulations of non-ideal gases. For the validation of the DNS results, the predictions obtained by Linear Stability Theory are utilized.

After determining the optimal set of parameters, the stability of supercritical carbon dioxide boundary layers is investigated using DNS and validated with LST predictions. Although results provided by the two methods can be compared, they are not entirely identical since the latter method assumes a parallel flow.

## 1.3. THEORETICAL FRAMEWORK

The theoretical concepts adapted in this study are presented in this section. A brief explanation of laminar to turbulent transition is provided, along with a description of the fluid behaviour in the thermodynamic region of interest.

### 1.3.1. FLOW STABILITY AND TRANSITION

The various paths that can lead to turbulence have been identified and summarized by Morkovin [21] and are presented in figure 1.2. In general, transitional mechanisms are triggered by disturbances in the flow, which might be either acoustic or vortical. Depending on the intensity of the initial disturbance, a different path is followed.

One possible route that can lead to turbulence is the linear growth of instabilities caused by low amplitude disturbances that excite the natural modes of the flow. The growth of primary instabilities is succeeded by the formation of secondary instabilities that cause a breakdown of the laminar state, resulting to turbulence. In figure 1.2 it is marked as path a. Path b, corresponds to higher disturbance amplitudes. In this case, secondary instabilities are formed as a result of the linear superposition of the natural modes that grow for a short time, without the occurrence of primary instabilities. For disturbances of excessively high amplitude, all the mode excitation process is bypassed and a non-linear growth is exhibited which immediately generates turbulent structures.

Terms associated with the transition to turbulence are explained below.

- *Receptivity Mechanisms:* The mechanisms through which an external disturbance triggers the growth of instabilities in the flow. For strong external disturbances, non-linear growth might be induced, directly leading to turbulence. For weaker

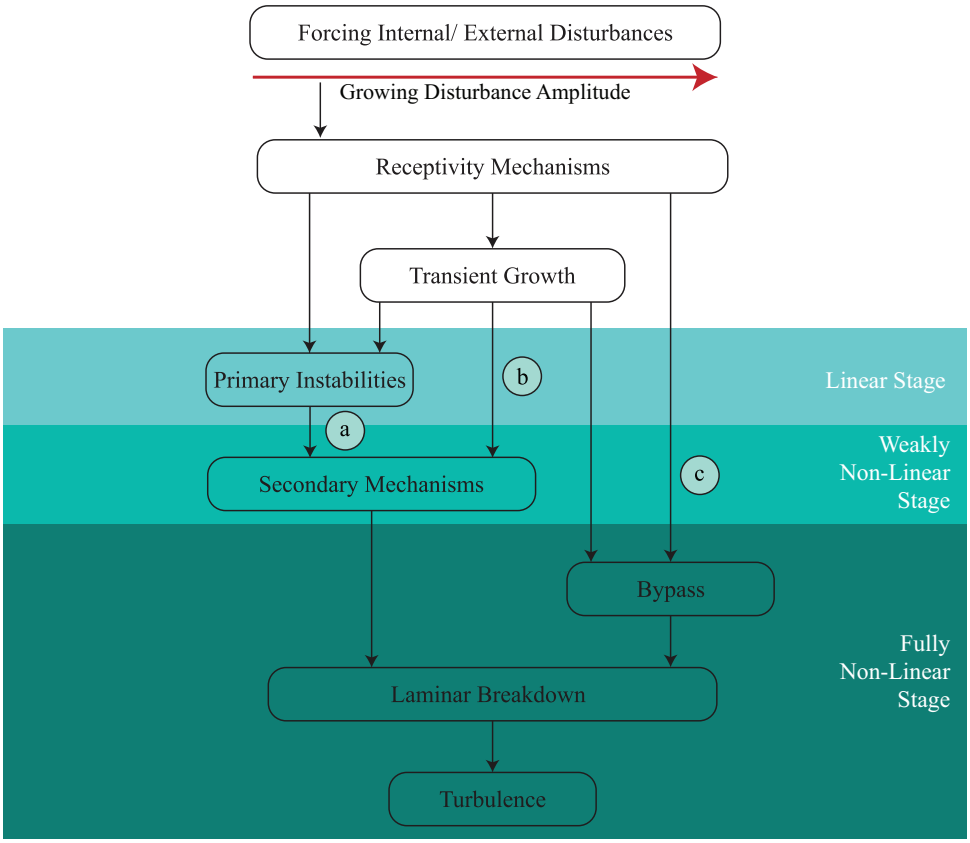


Figure 1.2: Routes of Laminar to Turbulent Transition [21].

disturbances, free disturbances within the flow are triggered, leading to a linear growth.

- *Primary Instabilities:* Refers to the initially excited modes, which grow within a linear regime. Depending on the amplitude of the external disturbance, the instabilities might either keep growing until the growth is no longer linear, for high disturbance levels. For lower disturbance levels, the primary instabilities might decay and the flow will return to its laminar state. The free disturbances that correspond to the natural modes of a boundary layer, are referred to as *Tollmien-Schlichting (TS) waves.*

- *Secondary Mechanisms:* Once the developing instabilities grow beyond the linear level, secondary mechanisms further destabilize leading to an exceedingly high growth rate until the eventual breakdown and transition to turbulence.

- *Breakdown:* Refers to the last stage before the transition to turbulence. In this stage, the exceedingly strong, non-linear instabilities break down and form com-

plex, chaotic structures that mark the transition to turbulence. Breakdown is associated with the emergence of multiple new time and length scales in the flow.

- *Turbulence:* A chaotic state that is reached after breakdown. It is characterised by a wide range of time and length scales in three dimensions, hence very complex.

- *Non-Linear Saturation:* This term refers to a state in which the instabilities no longer grow in space, indicating saturation. It is caused by the excessive growth of primary instabilities, however, instead of the emergence of secondary instabilities, the flow reaches a new periodic state which is more complicated compared to the initial laminar state.

For a boundary layer, the transitional behaviour that follows path a, is provided in figure 1.3. Initial disturbances trigger the growth of instabilities, in the linear regime. The instabilities keep growing until secondary mechanisms introduce more complex structures, in the weakly non-linear regime. In the non-linear regime, the excessive growth of secondary instabilities leads to breakdown, the formation of irregular structures and chaotic behaviour, indicating a turbulent flow.

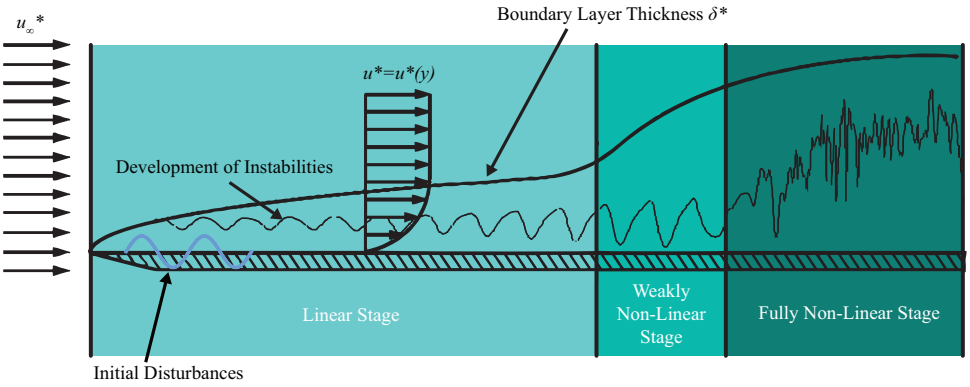


Figure 1.3: Laminar to turbulent transition for a flow over a flat plate.

The main focus of this study is centered around the linear regime. To study the stability of boundary layer flows, a weak initial perturbation is introduced to trigger the TS waves that grow in space and then decay. This behaviour can, also, be predicted using Linear Stability Theory which is used for the validation of the results of the direct numerical simulations.

### 1.3.2. CARBON DIOXIDE IN THE SUPERCRITICAL REGIME

To investigate how non-ideal gas properties affect the stability of boundary layer flows, supercritical carbon dioxide is selected. The critical pressure of carbon dioxide is $p^* = 74.77\ bar$, for the purposes of this study, a pressure of $p^* = 80.0\ bar$ is selected, which corresponds to the superctitical regime. A contour plot of the compressibility factor $Z = p^*/(\rho^* R^* T^*)$ is provided in figure 1.4.

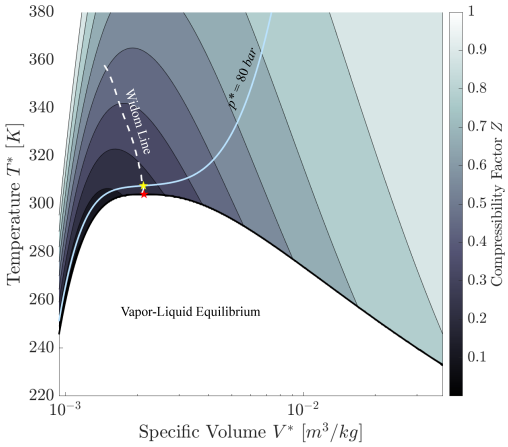


Figure 1.4: Contour plot of compressibility factor $Z$ as a function of specific volume $V^*$ and temperature $T^*$. The Widom line is marked by the white dashed line and the $p^* = 80.0\ bar$ isobar, by the light blue line. The critical point is marked by ($\star$), whereas the pseudo-critical point by ($\star$).

By identifying the point of maximum heat capacity $C_p$ along the $p = 80.0\ bar$ isobar, the pseudo-critical point is found at $T^*_{pc} = 307.77\ K$. The line that is formed by identifying the pseudo-critical points on all supercritical isobars, defines the *Widom line* and corresponds to a region where highly non-ideal behaviour is exhibited by the fluid [33], [27]. The low compressibility factor values around the Widom line in figure 1.4 also support this statement, since $Z = 1.0$ corresponds to ideal gas. When the temperature of carbon dioxide is increased from below the pseudo-critical point to a temperature above the pseudo-critical point, the fluid exhibits a dramatic change from dense, liquid-like to vapor-like behaviour. The thermodynamic and transport properties undergo enormous variations, as well.

Direct numerical simulations are performed for various temperatures along the $p^* = 80\ bar$ isobar for carbon dioxide and the effects of non-ideal behaviour on boundary layer stability are examined.

## 1.4. THESIS OUTLINE

**Chapter 2** includes the mathematical description and the governing equations that define the problem.

**Chapter 3** presents the tools that have been developed and used for the mathematical modelling of the problem, as well as the solution methods that are incorporated.

**Chapter 4** provides an analytical explanation of the numerical parameters that are utilized for the configuration of the direct numerical simulations.

**Chapter 5** presents the results of direct numerical simulations for an ideal gas. In this chapter the computational parameters of the code are varied and the influence of each parameter is determined.

**Chapter 6** presents the results of direct numerical simulations for a non-ideal gas. The stability of non-ideal boundary layers is investigated in this chapter.

**Chapter 7** summarizes the work presented and provides recommendations for aspects that require further investigation, based on the results of this study.

# 2

# GOVERNING EQUATIONS

The mathematical description of the present study will be provided in this chapter. The basis behind the concepts that are utilised, are the flow conservation equations that are modified to produce a self-similar solution, which will be used as the base flow, and the equations that are required for the Linear Stability Theory.

## 2.1. FLOW CONSERVATION EQUATIONS

A fluid flow is mathematically described by the conservation laws of mass, momentum and energy, also known as the Navier-Stokes equations. In differential and dimensionless form they are expressed as

$$\left.\begin{aligned} \frac{\partial \rho}{\partial t} + \frac{\partial (\rho u_j)}{\partial x_j} &= 0, \\ \frac{\partial (\rho u_i)}{\partial t} + \frac{\partial (\rho u_i u_j + p\delta_{ij} - \tau_{ij})}{\partial x_j} &= 0, \\ \frac{\partial (\rho E)}{\partial t} + \frac{\partial (\rho E u_j + p u_j + q_j - u_i \tau_{ij})}{\partial x_j} &= 0, \end{aligned}\right\} \tag{2.1}$$

where $u_i = (u, v, w)$ are the velocity components in streamwise, wall-normal and spanwise directions respectively and $x_i = (x, y, z)$ are the corresponding coordinates, with $t$ being the time. The fluid density and pressure are expressed by $\rho$ and $p$, respectively. The total internal energy is $E = e + u_i u_i/2$ where $e$ the internal energy. The viscous stress tensor, $\tau_{ij}$, and the heat flux vector, $q_j$, are given by

$$\left.\begin{aligned} \tau_{ij} &= \frac{\mu}{Re_\infty}\left(\frac{\partial u_i}{\partial x_j} + \frac{\partial u_j}{\partial x_i}\right) + \frac{\lambda}{Re_\infty}\delta_{ij}\frac{\partial u_k}{\partial x_k}, \\ q_j &= -\frac{\kappa}{Re_\infty Pr_\infty Ec_\infty}\frac{\partial T}{\partial x_j}. \end{aligned}\right\} \tag{2.2}$$

In equation (2.2), $\mu$ stands for the dynamic viscosity and $\lambda = \mu_b - 2/3\mu$ the second viscosity with $\mu_b$ the bulk viscosity. A study conducted by Ren et al. [28], showed that the

effect of $\mu_b$ is very limited in the linear stability for channel flows, hence for the results of the present study it is assumed that $\mu_b$ is equal to zero. In the expression for the heat flux vector $q_j$, $\kappa$ indicates the thermal conductivity and $T$ the fluid temperature.

Equations 2.1 and 2.2 have been non-dimensionalized by the following reference values

$$u = \frac{u^*}{u^*_\infty},\ x_i = \frac{x^*_i}{l^*_0},\ t = \frac{t^* u^*_\infty}{l^*_0},\ p = \frac{p^*}{\rho^*_\infty u^{*2}_\infty},\ \rho = \frac{\rho^*}{\rho^*_\infty},$$
$$T = \frac{T^*}{T^*_\infty},\ E = \frac{E^*}{u^{*2}_\infty}, \mu = \frac{\mu^*}{\mu^*_\infty},\ \kappa = \frac{\kappa^*}{\kappa^*_\infty}. \tag{2.3}$$

The superscript $*$ indicates dimensional values, while subscript $\infty$ the value of a variable in the free-stream. The characteristic length scale that is selected for a particular flow is expressed as $l^*_0$.

In fluid dynamics, a flow can be characterised by dimensionless parameters that result from scaling analysis. Flows with similarities in the values of these parameters, will exhibit similar behaviour. The most important dimensionless parameters for a flow over a flat plate are listed below, based on free-stream quantities

$$\text{Reynolds Number}: Re_\infty = \frac{\text{Inertial Forces}}{\text{Viscous Forces}} = \frac{\rho^*_\infty u^*_\infty l^*_0}{\mu^*_\infty}, \tag{2.4}$$

$$\text{Prandtl Number}: Pr_\infty = \frac{\text{Momentum Diffussivity}}{\text{Thermal Diffussivity}} = \frac{C^*_{p\infty}\mu^*_\infty}{\kappa^*_\infty}, \tag{2.5}$$

$$\text{Eckert Number}: Ec_\infty = \frac{\text{Kinetic Energy}}{\text{Enthalpy}} = \frac{u^{*2}_\infty}{C^*_{p\infty} T^*_\infty}, \tag{2.6}$$

$$\text{Mach Number}: Ma_\infty = \frac{\text{Flow Velocity}}{\text{Speed of Sound}} = \frac{u^*_\infty}{c^*_\infty}. \tag{2.7}$$

In the above equations $C_p$ stands for the specific heat capacity of the fluid and $c$ for the speed of sound. It is, also, noted that for an ideal gas $Ec_\infty = (\gamma - 1)Ma^2_\infty$, where $\gamma$ is the ratio of specific heat capacities.

A description of the physical significance for each of the dimensionless parameters is given below

- The Reynolds number ($Re$) is used to express the dominance of inertial forces in a flow, over the viscous forces. In general, increasing the Reynolds number will result to transition to turbulence.
- The Prandtl number ($Pr$) provides information about the dominant heat transfer mechanism in a medium. In substances with high Prandtl number, convective heat transfer is more effective than heat conduction whereas in substances with low Prandtl number, conduction of heat is dominant. In boundary layers, a high Prandtl number ($Pr > 1$) indicates that the velocity boundary layer is thicker compared to the thermal boundary layer, since momentum dissipates through the fluid at a higher rate compared to heat.

- The Eckert number ($Ec$) can be used to express the effect of viscous heat dissipation in viscous flows. Higher Eckert numbers imply that viscous heating will be prominent in the flow and in non-ideal fluids this causes gradients in the thermodynamic and transport properties.
- The Mach number ($Ma$) is a measure of the compressibility effects on the flow. For flows with $Ma < 0.3$ these effects are considered negligible, hence the flow is incompressible.

Another important parameter, in the present analysis, is $\delta^*$, which is used to express the order of magnitude of the boundary layer thickness. The value of this parameter is calculated by

$$\delta^* = \sqrt{\frac{\mu^*_\infty x^*}{u^*_\infty \rho^*_\infty}}, \tag{2.8}$$

which leads to the following formulation for the Reynolds number, by setting $l^*_0 = \delta^*$;

$$Re_\delta = \frac{\rho^*_\infty u^*_\infty \delta^*}{\mu^*_\infty} = \sqrt{\frac{\rho^*_\infty u^*_\infty x^*}{\mu^*_\infty}} = \sqrt{Re_x}. \tag{2.9}$$

Other parameters, associated with the boundary layer can be expressed in terms of the order of magnitude of the boundary layer thickness. For example the displacement thickness $\delta^*_1 \approx 1.721\delta^*$ and the momentum thickness $\delta^*_2 \approx 0.664\delta^*$ can be obtained by applying the Blasius solution on an incompressible flow [31]. The analytical expression for each of these quantities is provided below

$$\delta^*_1 = \int_0^\infty \left(1 - \frac{\rho^* u^*}{\rho^*_\infty u^*_\infty}\right) dy^*, \; \delta^*_2 = \int_0^\infty \frac{\rho^* u^*}{\rho^*_\infty u^*_\infty}\left(1 - \frac{u^*}{u^*_\infty}\right) dy^*. \tag{2.10}$$

## 2.2. LAMINAR BASE FLOW

For the investigation of boundary layer stability, it is essential to utilize a self-similar solution, for a flow over a flat plate, that will serve as the base flow for the Linear Stability Theory and as the initial condition for the Direct Numerical Simulations.

### 2.2.1. SIMPLIFICATION OF CONSERVATION EQUATIONS

Prior to the wider employment of computational methods, the numerical solution of the Navier-Stokes equations had been nearly impossible. However the necessity for such solutions, led to the simplification of the conservation equations through order-of-magnitude analysis. Consequently, for a flow over a flat plate, a simpler form of the Navier-Stokes equations was derived for viscous flows. The following derivation can be found in [1].

Considering the flow over a flat plate, two important length scales characterize the flow. One is the boundary layer thickness $\delta^*$ and the other is the length of the plate $L^*$. The first assumption in this analysis is that the boundary layer thickness is extremely small compared to the length of the plate, hence

$$\delta^* << L^*. \tag{2.11}$$

In two dimensional, steady form the continuity equation is written as

$$\frac{\partial(\rho u)}{\partial x} + \frac{\partial(\rho v)}{\partial y} = 0. \tag{2.12}$$

The streamwise coordinate $x^*$, varies from 0 to $L^*$, while the wall-normal coordinate $y^*$ varies from 0 to $\delta^*$. By assuming that $L*$ is a unit length, $x = O(1)$ and $y = O(\delta^*)$. Considering that the streamwise velocity $u$ ranges from 0 at the wall to 1 in the free-stream, similarly for the density $\rho$ and by scaling equation 2.12 appropriately, the following expression results

$$\frac{[O(1)][O(1)]}{O(1)} + \frac{[O(1)][v]}{O(\delta^*)} = 0. \tag{2.13}$$

The wall normal velocity $v$, needs to scale with $\delta^*$, so that the continuity equation is satisfied. Hence $v = O(\delta^*)$.

The steady streamwise momentum equation is expressed as

$$\rho u\frac{\partial u}{\partial x} + \rho v\frac{\partial u}{\partial y} = -\frac{\partial p}{\partial x} + \frac{1}{Re_\infty}\frac{\partial}{\partial y}\left[\mu\left(\frac{\partial v}{\partial x} + \frac{\partial u}{\partial y}\right)\right], \tag{2.14}$$

and scaling each term separately, gives the following

$$\rho u\frac{\partial u}{\partial x} = O(1),\ \rho v\frac{\partial u}{\partial y} = O(1),\ \frac{\partial p}{\partial x} = O(1),$$
$$\frac{\partial}{\partial y}\left(\mu\frac{\partial v}{\partial x}\right) = O(1), \frac{\partial}{\partial y}\left(\mu\frac{\partial u}{\partial y}\right) = O\left(\frac{1}{\delta^{*2}}\right).$$

Additionally, it is assumed that the Reynolds number is large enough, hence

$$\frac{1}{Re_\infty} = O(\delta^{*2}),$$

and equation 2.14 can be written in order-of-magnitude form as,

$$O(1) + O(1) = -O(1) + O(\delta^{*2})\left[O(1) + O\left(\frac{1}{\delta^{*2}}\right)\right]. \tag{2.15}$$

From equation 2.15, it observed that the term $(1/Re_\infty)\partial/\partial y(\mu\,\partial v/\partial x)$ scales with $\delta^{*2}$, and can be neglected, since it is of a lower order of magnitude compared to the other terms. The final form of the momentum equation in the streamwise direction becomes, then

$$\rho u\frac{\partial u}{\partial x} + \rho v\frac{\partial u}{\partial y} = -\frac{\partial p}{\partial x} + \frac{1}{Re_\infty}\frac{\partial}{\partial y}\left(\mu\frac{\partial u}{\partial y}\right). \tag{2.16}$$

By applying a similar order-of-magnitude analysis on the momentum in the wall-normal direction and the energy conservation equations, the final form of the conservation equations in dimensional form, for boundary layers, is

$$\left.\begin{aligned}
\frac{\partial\left(\rho^* u^*\right)}{\partial x^*}+\frac{\partial\left(\rho^* v^*\right)}{\partial y^*}&=0,\\
\rho^* u^*\frac{\partial u^*}{\partial x^*}+\rho^* v^*\frac{\partial u^*}{\partial y^*}+\frac{\mathrm{d}p^*_\infty}{\mathrm{d}x^*}-\frac{\partial}{\partial y^*}\left(\mu^*\frac{\partial u^*}{\partial y^*}\right)&=0,\\
\frac{\partial p^*}{\partial y^*}&=0,\\
\rho^* u^*\frac{\partial h^*}{\partial x^*}+\rho^* v^*\frac{\partial h^*}{\partial y^*}-u^*\frac{\mathrm{d}p^*_\infty}{\mathrm{d}x^*}-\frac{\partial}{\partial y^*}\left(\kappa^*\frac{\partial T^*}{\partial y^*}\right)-\mu^*\left(\frac{\partial u^*}{\partial y^*}\right)^2&=0.
\end{aligned}\right\} \tag{2.17}$$

### 2.2.2. SELF-SIMILAR SOLUTION

For a better explanation of the concept of a self-similar solution, figure 2.1 is provided. In the physical plane, the flow variables are a function of both, the stream-wise and the wall-normal coordinates. In fugure 2.1, the stream-wise velocity component is plotted on the left, at two different stream-wise locations and it is evident that the profile is different at each location. By introducing a transformation on the physical coordinates $x$ and $y$, it is possible to obtain a solution that is independent of the stream-wise location, as shown on the right part of figure 2.1.

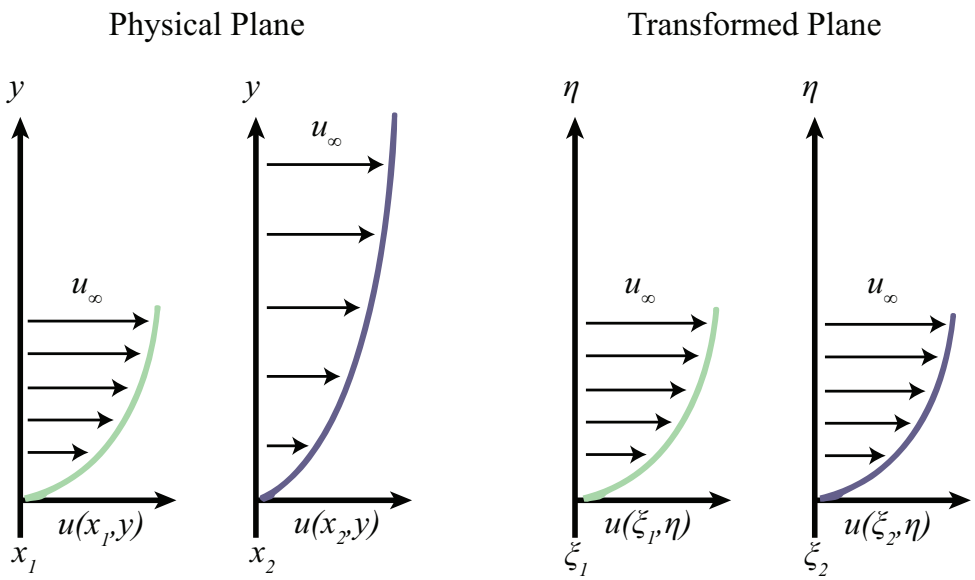


Figure 2.1: Illustration of a self-similar transformation.

The transformation that will be used for the purposes of the present study, is based on the work of Dorodnitsyn [6] in the 1940s and was later refined by Levy [13] and Lees [11]. The physical coordinates $x$ and $y$ are mapped to the transformed coordinates $\xi$ and $\eta$, respectively in order to produce a self-similar solution. In Anderson Jr. [1] this

transformation is referred to as the Lees-Dorodnitsyn transformation and is formulated as

$$\left.\begin{aligned} \mathrm{d}\xi &= \rho^*_\infty \mu^*_\infty u^*_\infty \,\mathrm{d}x^*, \\ \mathrm{d}\eta &= \frac{\rho^* u^*_\infty}{\sqrt{2\xi}} \,\mathrm{d}y^*. \end{aligned}\right\} \tag{2.18}$$

Applying the transformation on equations 2.17, transforms the partial differential equations into ordinary differential equations. This is done in four steps.

1. Derivatives over independent variables $x^*$ and $y^*$ are transformed into derivatives over the transformed variables $\xi$ and $\eta$, using the chain rule.

2. Dependent variables are transformed by defining a function $f(\xi,\eta)$ such that

$$\frac{u^*}{u^*_\infty} = \frac{\partial f}{\partial \eta} \equiv f'. \tag{2.19}$$

3. Identify a correlation between the stream-function $\psi$ and $f$.

4. Apply the transformation on equations 2.17 and obtain the final form of the boundary layer equations for a self-similar solution.

Finally, the transformed self-similar boundary layer equation is

$$\left.\begin{aligned} \frac{\partial}{\partial\eta}\left(C_l \frac{\partial^2 f}{\partial\eta^2}\right) + f\frac{\partial^2 f}{\partial\eta^2} &= 0, \\ \frac{\partial}{\partial\eta}\left(\frac{C_l}{Pr_l}\frac{\partial g}{\partial\eta}\right) + f\frac{\partial g}{\partial\eta} + C_l \frac{u^{*2}_\infty}{h^*_{s\infty}}\left(\frac{\partial^2 f}{\partial\eta^2}\right)^2 &= 0, \end{aligned}\right\} \tag{2.20}$$

where

$$g = \frac{h^*_s}{h^*_{s,\infty}},\ C_l = \frac{\rho^*\mu^*}{\rho^*_\infty \mu^*_\infty},\ Pr_l = \frac{\mu^* C^*_p}{\kappa^*}. \tag{2.21}$$

In equations 2.20 and 2.21, $h^*_s$ stands for the local static enthalpy in $J/kg$ and $Pr_l$ is the local Prandtl number.

## 2.3. LINEAR STABILITY THEORY

The research of the field of fluid flow stability has its roots back in the 19$^{\text{th}}$ century, first studied by Reynolds and Rayleigh. For the better comprehension of modal growth and transition to turbulence, Linear Stability Theory is an appropriate method of approach to the problem of flow stability. Although this method does not provide a detailed description of flow patterns, it is extremely useful since it can predict the growth of small disturbances both in time and space, provided the corresponding base flow.

The main idea behind the derivation of the Linear Stability equations, lies behind the expression of flow variables as the summation of a mean value (denoted by 0) and a

fluctuation (denoted by $'$) , as shown below

$$\begin{aligned} u_i &= u_{i,0} + u_i^{'}, \\ \rho &= \rho_0 + \rho^{'}, \\ E &= E_0 + E', \\ T &= T_0 + T^{'}, \\ p &= p_0 + p^{'}, \\ \mu &= \mu_0 + \mu^{'}, \\ \kappa &= \kappa_0 + \kappa^{'}. \end{aligned} \tag{2.22}$$

Having expressed the flow variables as mentioned above, the following procedure is adapted. Firstly, the equations 2.22 are substituted in the conservation equations 2.1 and the terms containing only mean values are dropped by subtracting each corresponding conservation equation that only contains the mean of each parameter. Next, a parallel assumption is introduced for boundary layer flows. This assumes that the wall normal velocity component is zero at all wall normal locations, hence $v_0 = 0$. Also, it is assumed that the instabilities develop slowly in the stream-wise direction, in the sense that the length scale of the instabilities is much smaller than the length scale of the base flow. Finally, since the fluctuations are assumed to have a small value, all the non-linear terms, containing the products of fluctuation terms are omitted.

For compressible systems consisting of one single-phase, non chemically reacting substance, only two thermodynamic properties are required in order to fully define the thermodynamic state. In the current study, all the thermodynamic and transport properties are determined as functions of fluid density $\rho$ and temperature $T$.

The fluctuation terms for each quantity are expressed as

$$\boldsymbol{q}(x,y,z,t) = \hat{\boldsymbol{q}}(y)\exp\left(i\alpha x + i\beta z - i\omega t\right) + c.c, \tag{2.23}$$

where $c.c$ stands for the complex conjugate, and $\boldsymbol{q} = (\rho^{'}, u^{'}, v^{'}, w^{'}, T^{'})^T$ . The variables $\beta$ and $\omega$ are the span-wise wavenumber and angular frequency, respectively, while $\alpha$ is a complex number, of which the real part corresponds to the stream-wise wavenumber and the imaginary part corresponds to the local growth rate of the fluctuation. Expressing the Linearised Stability equations in terms of $\boldsymbol{q}$, gives

$$\begin{aligned} &\boldsymbol{L_t}\frac{\partial \boldsymbol{q}}{\partial t} + \boldsymbol{L_x}\frac{\partial \boldsymbol{q}}{\partial x} + \boldsymbol{L_y}\frac{\partial \boldsymbol{q}}{\partial y} + \boldsymbol{L_z}\frac{\partial \boldsymbol{q}}{\partial z} + \boldsymbol{L_q}\boldsymbol{q} \\ &\quad + \boldsymbol{V_{xx}}\frac{\partial^2 \boldsymbol{q}}{\partial x^2} + \boldsymbol{V_{xy}}\frac{\partial^2 \boldsymbol{q}}{\partial x \partial y} + \boldsymbol{V_{xz}}\frac{\partial^2 \boldsymbol{q}}{\partial x \partial z} + \boldsymbol{V_{yy}}\frac{\partial^2 \boldsymbol{q}}{\partial y^2} + \boldsymbol{V_{yz}}\frac{\partial^2 \boldsymbol{q}}{\partial y \partial z} + \boldsymbol{V_{zz}}\frac{\partial^2 \boldsymbol{q}}{\partial z^2} = 0, \end{aligned} \tag{2.24}$$

with $\boldsymbol{L_t}$, $\boldsymbol{L_x}$, $\boldsymbol{L_y}$, $\boldsymbol{L_z}$, $\boldsymbol{L_q}$, $\boldsymbol{V_{xx}}$, $\boldsymbol{V_{xy}}$, $\boldsymbol{V_{xz}}$, $\boldsymbol{V_{yy}}$, $\boldsymbol{V_{yz}}$ and $\boldsymbol{V_{zz}}$ being $5 \times 5$ matrices. Their full form can be found in Ren et. al [28]. Since the present study mainly focuses on the *spatial growth* of instabilities, $\beta$ and $\omega$ are prescribed variables and a solution of the resulting eigenvalue problem is obtained for $\alpha$.

# 3

# SOLUTION METHODS AND MATHEMATICAL APPROACH

The governing equations mentioned in chapter 2 are solved using the methods that are explained in detail in this chapter.

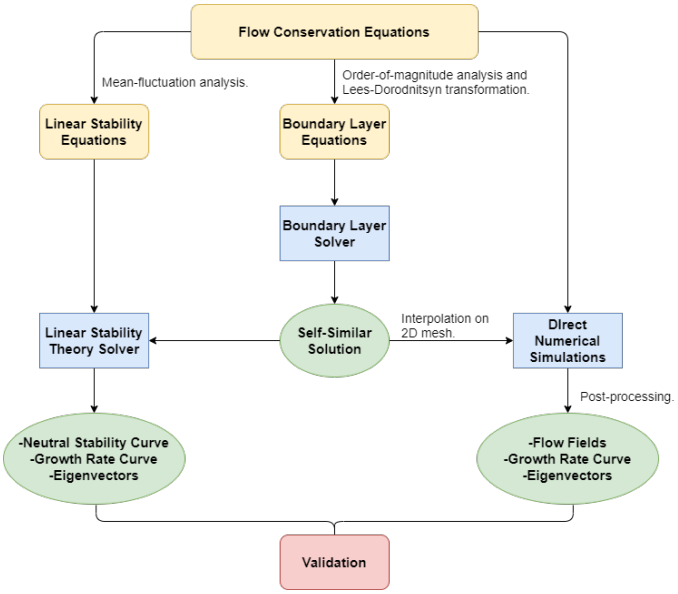


Figure 3.1: Workflow diagram of the present study.

Firstly, the boundary layer solver is used to obtain the self-similar solution for a flow over a flat plate. The self-similar solution is used by the Linear Stability solver in order to calculate the neutral stability curve which provides the growth rate of instabil-

ities at each stream-wise location. Also, the self-similar solution is interpolated on a two-dimensional mesh and the resulting flow field is used as the initial condition for the direct numerical simulations, which provide an accurate solution of the flow. By post-processing the resulting flow fields, it is possible to validate the results of the Linear Stability solver. This process is illustrated in figure 3.1.

## 3.1. SELF-SIMILAR SOLUTIONS AND LAMINAR BASE FLOW CALCULATION

For the calculation of the self-similar solution, a `MATLAB` script is utilized to numerically solve equations (2.20) in the transformed plane ($\xi$ and $\eta$ plane) and translate the solution back to the physical plane ($x$ and $y$ plane). The script was developed for the purposes of the present study.

### 3.1.1. BOUNDARY CONDITIONS

To fully define the physical problem, it is necessary to utilize the proper boundary conditions. In the case of boundary layers, the following conditions apply.

1. For isothermal wall

$$\left.\begin{aligned} u(y=0)=0,\ u(y\to\infty)=1,\\ T(y=0)=\frac{T^*_w}{T^*_\infty},\ T(y\to\infty)=1,\end{aligned}\right\}\ \text{in the physical plane} \tag{3.1}$$

$$\left.\begin{aligned} f(\eta=0)=f'(\eta=0)=0,\ f'(\eta\to\infty)=1,\\ g(\eta=0)=\frac{h^*_{s,w}}{h^*_{s,\infty}},\ g(\eta\to\infty)=1.\end{aligned}\right\}\ \text{in the transformed plane} \tag{3.2}$$

2. For adiabatic wall

$$\left.\begin{aligned} u(y=0)=0,\ u(y\to\infty)=1,\\ \left.\frac{\partial T}{\partial y}\right|_{(y=0)}=0,\ T(y\to\infty)=1,\end{aligned}\right\}\ \text{in the physical plane} \tag{3.3}$$

$$\left.\begin{aligned} f(\eta=0)=f'(\eta=0)=0,\ f'(\eta\to\infty)=1,\\ g'(\eta=0)=0,\ g(\eta\to\infty)=1.\end{aligned}\right\}\ \text{in the transformed plane} \tag{3.4}$$

In order to satisfy the free-stream boundary conditions ($\eta\to\infty$) , the numerical domain for $\eta$ needs to be long enough to ensure that the top boundary is far from the boundary layer.

### 3.1.2. THERMODYNAMIC PROPERTIES

To fully define the thermodynamic conditions of a flow, two thermodynamic properties should be known and an equation of state must be selected. In the present study results are provided for both, non-ideal and ideal gases, hence two different methods are employed for the definition of the flow conditions which will be explained in this section.

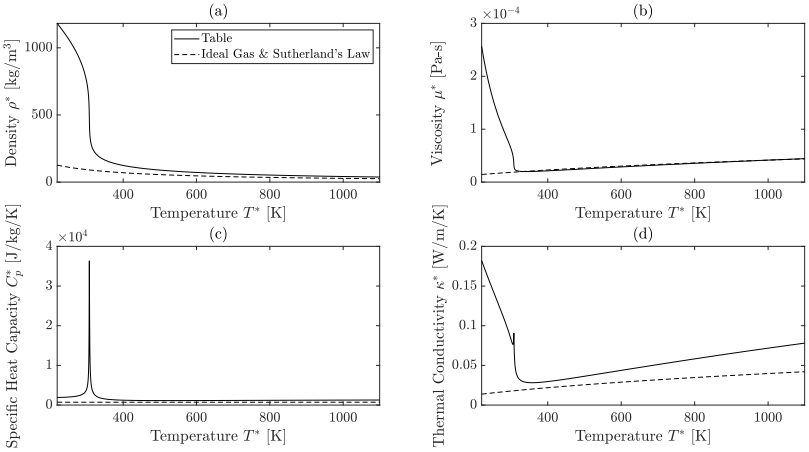


Figure 3.2: Graphical representation of one-dimensional property tables for Carbon Dioxide at $p^* = 80bar$ and comparison with Ideal Gas equation of state. Properties are plotted as functions of fluid temperature. Plots present (a) fluid density $\rho^*$, (b) viscosity $\mu^*$, (c) specific heat capacity $C_p^*$ and (d) thermal conductivity $\kappa^*$.

**Ideal Gas Equation of State**

For gases that exhibit ideal behaviour, an *Ideal Gas* equation of state is utilized for the calculation of the thermodynamic properties and *Sutherland's Law* for viscosity as presented below.

$$\left.\begin{aligned} p^* &= \rho^* R^* T^*, \\ h_s^* &= C_p^* T^*, \end{aligned}\right\} \text{Ideal Gas Equation of State} \tag{3.5}$$

$$\left.\frac{\mu^*}{\mu_{ref}^*} = \left(\frac{T^*}{T_{ref}}\right)^{1.5} \frac{T_{ref}^* + S^*}{T^* + S^*},\right\} \text{Sutherland's Law for Viscosity} \tag{3.6}$$

where $R^*$ is the ideal gas constant which is set to $287.1 J/kgK$ and $S^*$ is the Sutherland constant which has a value of $101K$. Reference values $\mu_{ref}^*$ and $T_{ref}^*$ are set to $1.789 \times 10^{-5} Pa\ s$ and $288K$, respectively. All the selected values correspond to air that exhibits ideal gas behaviour. The solution of equations (2.20) provides the local static enthalpy value, therefore one more thermodynamic property needs to be provided for the calculation of the other properties. Hence, it is assumed that the pressure is constant

along the wall-normal direction, and equal to $1atm$, to fully define the thermodynamic state. Finally, constant Prandtl number ($Pr_l$) and ratio of specific heats ($\gamma$) are assumed with values set at 0.75 and 1.4 respectively.

**One-Dimensional Table Interpolation for Non-Ideal Gases**

One of the main objectives of the present study is to investigate the stability of fluid flows close to the pseudo-critical point, where non-ideal behaviour is exhibited, hence the *Ideal Gas* law is no longer applicable. In this case, to calculate the thermodynamic properties, table interpolation is utilized. The tables are generated by `REFPROP` for Carbon Dioxide at $p^* = 80bar$, using the *GERG 2004* equation of state. Since the boundary layer equations (2.20) are derived based on the assumption that the pressure is fixed at a certain value, all properties are functions of only one thermodynamic variable, as shown in figure 3.2. A complete formulation of the equation of state and transport property models can be found in [10].

### 3.1.3. NUMERICAL METHODS

Since 2.20 is a system of second and third order ODEs, it is decomposed into a system of first order ODEs as follows,

$$\left.\begin{aligned} f' &= F, \\ F' &= \frac{A}{C_l}, \\ A' &= -\frac{f\,A}{C_l}, \\ g' &= \frac{Pr_l}{C_l} B, \\ B' &= -\frac{Pr_l}{C_l} f\,B - \frac{h^*_{s\infty}}{C_l\,u^{*2}_\infty} A^2. \end{aligned}\right\} \tag{3.7}$$

For the numerical integration of equations (3.7), a fourth order Runge-Kutta scheme is utilized as formulated below, for $f'$;

$$\begin{aligned} \frac{\mathrm{d}f}{\mathrm{d}\eta} &= f'(\eta, F), \\ f_{n+1} &= f_n + \frac{1}{6}\Delta\eta(k_{f,1} + 2k_{f,2} + 2k_{f,3} + k_{f,4}), \end{aligned} \tag{3.8}$$

with $\Delta\eta$ the step of the discretized $\eta$ coordinate and terms $k_{f,i}$ defined as;

$$
\begin{aligned}
k_{f,1} &= f'\left(\eta_n, F_n\right), \\
k_{f,2} &= f'\left(\eta_n + \frac{\Delta\eta}{2}, F_n + \Delta\eta\frac{k_{F,1}}{2}\right), \\
k_{f,3} &= f'\left(\eta_n + \frac{\Delta\eta}{2}, F_n + \Delta\eta\frac{k_{F,2}}{2}\right), \\
k_{f,4} &= f'\left(\eta_n + \Delta\eta, F_n + \Delta\eta k_{F,3}\right).
\end{aligned}
$$

Equations (3.7) need to be solved simultaneously. For the discretization of each of the left-hand side terms, the RK-4 scheme is applied. Terms $k_{\sim,i}$ are evaluated for *all* left-hand side variables before proceeding to the calculation of $k_{\sim,i}$, where $\sim$ corresponds to each of the left-hand side variables. In the case where a left-hand side variable is a function of more than one of the other left-hand side variables, the evaluation of $k_i$ is modified accordingly. For instance, to evaluate $k_{A,3}$, the following expression is used,

$$
k_{A,3} = A'\left[\eta_n + \frac{\Delta\eta}{2}, f_n + \Delta\eta\frac{k_{f,2}}{2}, A_n + \Delta\eta\frac{k_{A,2}}{2}, C_l\left(g_n + \Delta\eta\frac{k_{g,2}}{2}\right)\right].
$$

The system of equations (3.7) consists of five ODEs, hence for the numerical integration of the system, five *wall* boundary conditions are required. According to equations (3.2) and (3.4), only three boundary conditions are imposed at the wall, therefore the two remaining boundary conditions need to be assumed. To achieve that, a *shooting* method is employed, which makes use of the free-stream boundary conditions in order to estimate proper values for the remaining wall boundary conditions. The *shooting* method is applied by the following procedure, as described in Anderson Jr. [1]. An illustration of the shooting method is provided in figure 3.3.

1. Values for $f''(\eta = 0)$ and $g'(\eta = 0)$ for isothermal wall are assumed, or for $f''(\eta = 0)$ and $g(\eta = 0)$ for adiabatic wall. Values between 0.5 and 1.0 are good initial guesses.

2. Using the selected integration scheme (`RK-4` for this case), the system of equations is integrated along $\eta$.

3. If the resulting values of $f(\eta \to \infty)$ and $g(\eta \to \infty)$ match the free-stream boundary conditions, then the self-similar solution has been calculated. Otherwise, new values for the wall boundary conditions need to be assumed and the steps are repeated until the free-stream boundary conditions are satisfied. To determine an appropriate set of new wall values after each iteration, the built-in `MATLAB` function `lsqnonlin` is utilized.

The transformed wall-normal coordinate $\eta$ is discretized into 2000 equidistant grid points and the maximum value ($\eta_{max}$) is set to 10, which is found to be sufficiently far from the boundary layer.

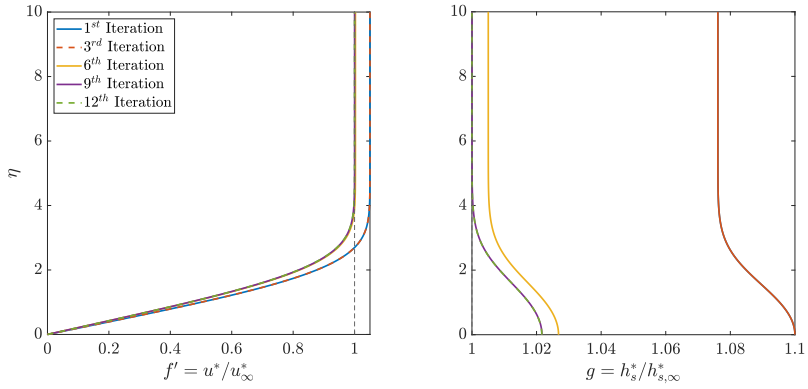


Figure 3.3: Shooting method applied on the normalized stream-wise velocity $u^*/u^*_\infty$ and normalized enthalpy $h_s/h_{s,\infty}$. The velocity gradient and enthalpy at the wall are altered after each iteration until the free-stream boundary conditions are satisfied.

### 3.1.4. TWO-DIMENSIONAL BASE FLOW

The numerical integration of the system of equations (2.20) provides the desired self-similar solution, which means that the velocity, temperature, density and viscosity profiles are calculated along $\eta$. To obtain the two-dimensional profiles, it is necessary to transform the self-similar solution back to the physical plane. Rearranging equations (2.18) and combining with (2.8), results to

$$\frac{y^*}{\delta^*} = \int_0^{\eta_{max}} \frac{\sqrt{2}}{\rho} \mathrm{d}\eta, \tag{3.9}$$

which allows the mapping of each point from the $\eta$ domain to the $y^*/\delta^*$ domain. For the numerical integration of equation (3.9), an Explicit Euler scheme is employed, as shown below.

$$\begin{aligned} \frac{\mathrm{d}f}{\mathrm{d}\eta} &= f'(\eta, f), \\ f_{n+1} &= f_n + \Delta\eta\, f'\left(\eta_n, f_n\right). \end{aligned} \tag{3.10}$$

An example of this transformation is provided in figure 3.4.

Since $\delta^*$ is only a function of $x^*$, the one-dimensional profiles along the new coordinate $y^*/\delta^*$ can be easily translated into two-dimensional. Firstly, the two-dimensional computational domain is determined in terms of dimensions and the distance from the leading edge (which corresponds to the location of the *inlet*). By calculating the value of $\delta^*$ at each stream-wise location of the computational domain, the self-similar solution is mapped and interpolated, using spline interpolation, on the two-dimensional grid that is used for the direct numerical simulations. The details regarding the type of grid are discussed in section 4.1.

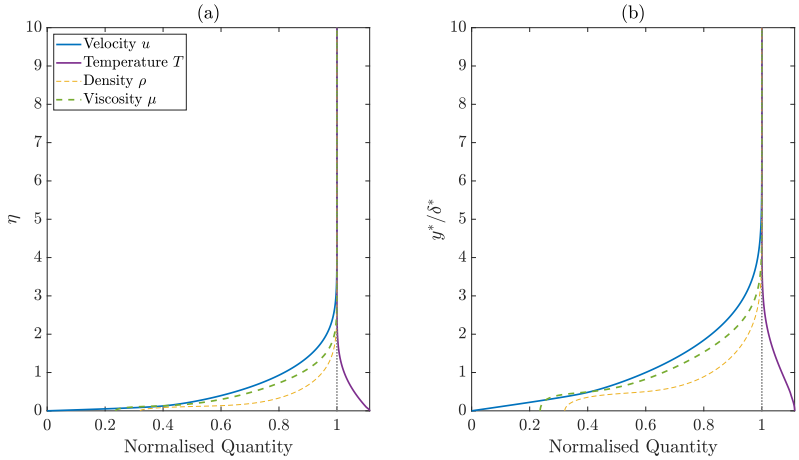


Figure 3.4: Self-similar solution for supercritical carbon dioxide at $T^*_\infty = 280K$ and $Ec_\infty = 0.20$, using table interpolation. Plot (a) presents the normalised quantities along $\eta$ and plot (b) the profiles mapped on $y^*/\delta^*$.

To obtain the two-dimensional profile for the wall-normal velocity component $v$, the steady-state form of the continuity equation is used as shown below;

$$\frac{\partial(\rho v)}{\partial y} = -\frac{\partial(\rho u)}{\partial x}. \tag{3.11}$$

To evaluate the right-hand side of the equation, a $2^{nd}$ Order Central finite difference scheme is incorporated, using the interpolated two-dimensional profiles of $u$ and $\rho$. The left-hand side is integrated using an Explicit Euler scheme as described by equation (3.10).

The calculated two-dimensional profiles serve as the base flow and are used as the initial condition for the direct numerical simulations. Specifically, the stream-wise and wall-normal velocity fields, along with the density and temperature are required. The example of figure 3.4 is presented in two-dimensional form in figure 3.5.

At this point it is convenient to determine the value of a new parameter, $\delta^*_{99,in}$ which will serve as the characteristic length scale $l^*_0$ for all the simulations presented in this study. This parameter expresses the *actual* thickness of the boundary layer, at the *inlet* of the computational domain. It corresponds to the wall-normal distance at which the stream-wise velocity component has a value of $u = 0.99$ and it is computed numerically. This parameter is, also, used to normalize the flow coordinates. Hence, $Re_\infty$ is defined as;

$$Re_\infty = \frac{\rho^*_\infty u^*_\infty \delta^*_{99,in}}{\mu^*_\infty}. \tag{3.12}$$

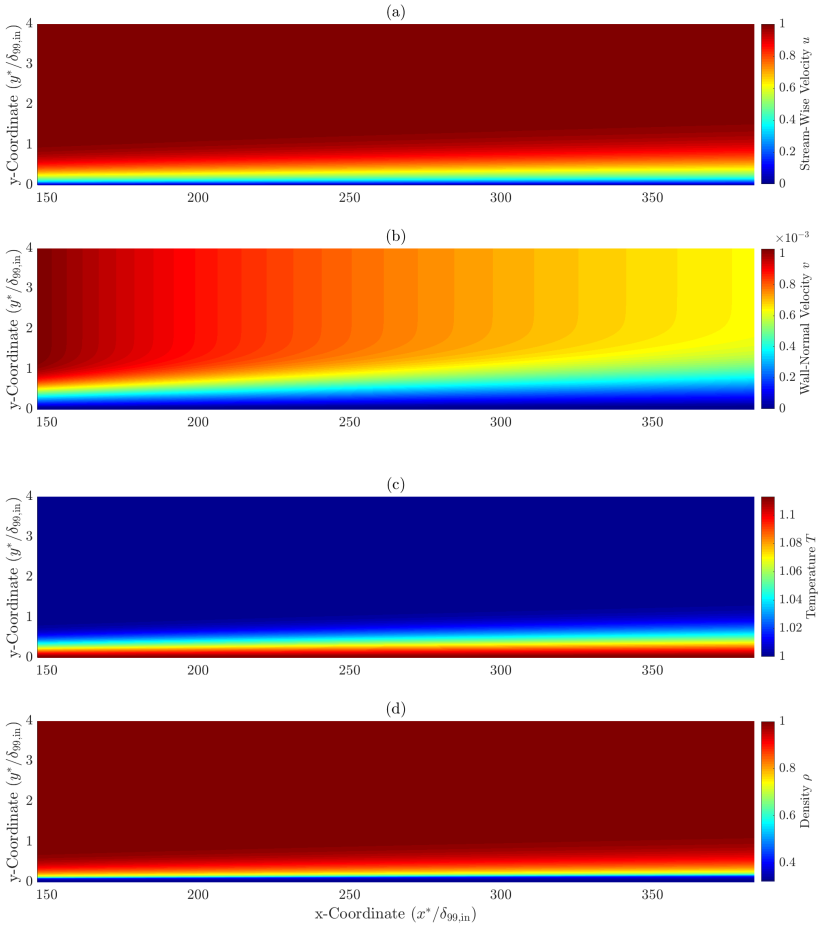


Figure 3.5: Example of two-dimensional flow profiles for supercritical carbon dioxide at $T^*_\infty = 280K$ and $Ec_\infty = 0.20$. Plots present (a) stream-wise velocity component $u$, (b) wall-normal velocity component $v$, (c) Temperature $T$ and (d) density $\rho$ profiles.

## 3.2. LINEAR STABILITY THEORY SOLVER

The eigenvalue problem defined by equation (2.24), is solved using a `MATLAB` script, developed by Dr. ir. Jie Ren. More details about the numerical techniques can be found in [28].

The spatial discretization in the $y$ direction utilizes Chebyshev collocation points and differentiation matrices to discretize the equations.

For the solution of the eigenvalue problem, the independent thermodynamic properties are $\rho_0$ and $T_0$. The thermodynamic ($E_0$ and $p_0$) and transport ($\mu_0$ and $\kappa_0$) properties as well as their first and second derivatives with respect to $\rho_0$ and $T_0$ are obtained from the `REFPROP` library using *GERG 2004* equation of state. For the case of ideal gases,

an *Ideal Gas* equation of state and *Sutherland's Law* for viscosity are used as described by equations (3.5) and (3.6).

By providing values of $\omega$, $Re_\delta$ and $\beta$ the stability equations (2.24) are solved as an eigenvalue problem, resulting to an *eigenspectrum* that consists of all the *eigenmodes* of that particular flow. A typical eigenspectrum is presented in figure 3.6a for a boundary layer flow.

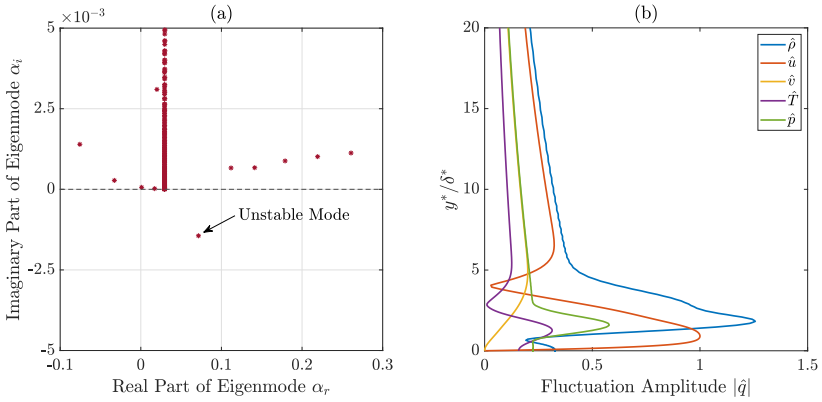


Figure 3.6: (a) Eigenspectrum for a supercritical carbon dioxide boundary layer with $T^*_\infty = 320K$, $Ec_\infty = 0.10$, $Re_\delta = 1400$, $F = 21 \times 10^{-6}$ and $\beta = 0$. Eigenmodes are represented by (*). (b) The eigenvector corresponding to the unstable mode. Values are normalised with respect to the maximum amplitude of the stream-wise velocity component fluctuation $u'$.

The vertically aligned modes are referred to as the *entropy/ vorticity* modes, whereas the continuous modes with greater and lower real parts, are the *fast* and *slow acoustic* modes, respectively. The unstable modes appear as discrete points in the eigenspectrum with negative imaginary part, as indicated in figure 3.6a. All modes are excited when the flow is perturbed, however only the *unstable* modes will grow in space and time. It is noted that some of the modes are not physical and could still appear on the eigenspectrum diagram even though convergence has not been achieved.

For every eigenmode exists a corresponding eigenvector, which represents the amplitude of the fluctuations $\hat{q}$ along the $y$ direction, for each quantity. These profiles can be validated with results obtained from DNS. Figure 3.6b is provided to illustrate a typical eigenvector that corresponds to an unstable mode.

As previously mentioned, the absolute value of the imaginary part of an eigenvalue, corresponds to the local growth rate of the perturbation. From this point on, the growth rate of instabilities will be referred to as $\alpha_i$, for brevity. By identifying the imaginary parts of the unstable modes for a range of $F$ and $Re_\delta$, the *Stability Diagram* is constructed. A contour plot of the growth rate as function of $F = \omega/Re_\infty$ and $Re_\delta$ is provided in figure 3.7. By selecting a value for $F$, it is possible to plot $\alpha_i$ as a function of $Re_\delta$, observing the growth and decay of instabilities along the stream-wise direction. These plots are validated with results obtained by DNS.

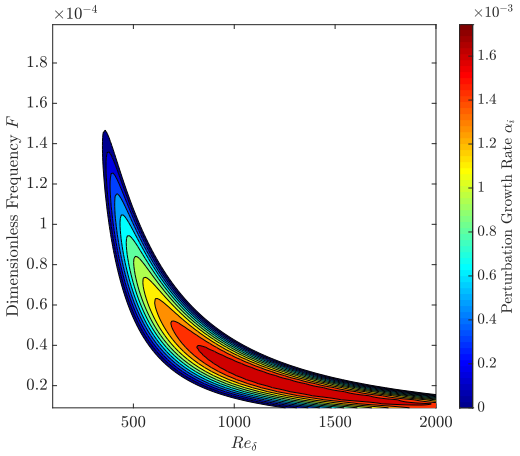


Figure 3.7: Stability diagram representing perturbation growth rate $\alpha_i$ as a function of $F$ and $Re_\delta$ for supercritical carbon dioxide with $T^*_\infty = 320$ and $Ec_\infty = 0.10$.

The contour that corresponds to a growth rate $\alpha_i = 0$, defines the *Neutral Stability Curve* and separates the stable from the unstable region in the stability diagram. A flow is characterized as more unstable if the extent of the neutral stability curve and the maximum growth rate that is observed in the stability diagram, are larger.

# 4

# DIRECT NUMERICAL SIMULATIONS

The direct numerical simulations are performed using an in-house `FORTRAN` code which was initially developed by Dr. ir. Rene Pecnik and ir. Simone Silvestri for the simulation of compressible turbulent channel flows. For the purposes of this study, new *boundary conditions* and a *table interpolation* tool for the calculation of thermodynamic properties are implemented, so that the simulations of non-ideal boundary layers are possible.

The flow conservation equations (2.1) are numerically solved, completely resolving flow structures at all scales, hence direct numerical simulations is a computationally expensive method that requires high spatial and temporal resolution. To study the stability of a boundary layer flow, the domain is truncated to the region of interest and a low-amplitude, periodic perturbation is introduced to trigger the growth of instabilities. Once the simulations are finished, the resulting flow fields are post-processed in order to validate the growth-rate curve predicted by the Linear Stability Theory.

## 4.1. COMPUTATIONAL GRID AND NUMERICAL SCHEMES

For the numerical integration of equations (2.1), a Cartesian *collocated* grid arrangement is used. That means that the values of each quantity are calculated at the corners of the computational grid cell. In this application the grid is *equidistant* in the stream-wise and span-wise directions, however in the wall-normal direction the grid is *fine* closer to the wall and gradually becomes *coarser* towards the free-stream. This is achieved by the positioning the wall-normal grid points according to the following expression,

$$\begin{aligned} \zeta &= \frac{1}{2}\frac{j-1}{j_{max}-1} - \frac{1}{2}, \\ y(j) &= L_y\left[1 + \frac{\tanh(\zeta s_f)}{\tanh(0.5 S_f)}\right], \end{aligned} \tag{4.1}$$

where $L_y$ is the total domain length in the wall-normal direction and $S_f$ is a stretching factor that makes the grid finer towards the wall when increased.

For the spatial discretization, a standard sixth-order central finite difference scheme is employed for the calculation of first derivatives and a fourth-order central scheme for the second derivatives. Close to the boundaries, the order is decreased accordingly. Specifically,

- For $i = 3$ and $i = i_{max} - 2$: $4^{th}$ Order Central Scheme for $1^{st}$ derivatives and $4^{th}$ Order Central Scheme for $2^{nd}$ derivatives.
- For $i = 2$ and $i = i_{max} - 1$: $2^{nd}$ Order Central Scheme for $1^{st}$ derivatives and $2^{nd}$ Order Central Scheme for $2^{nd}$ derivatives.
- For $i = 1$: $2^{nd}$ Order Forward Scheme for $1^{st}$ derivatives and $2^{nd}$ Order Forward Scheme for $2^{nd}$ derivatives.
- For $i = i_{max}$: $2^{nd}$ Order Backward Scheme for $1^{st}$ derivatives and $2^{nd}$ Order Backward Scheme for $2^{nd}$ derivatives.

A two-dimensional example of the computational grid is provided in figure 4.1, along with the spatial discretization schemes that are described above, applied in the wall-normal direction.

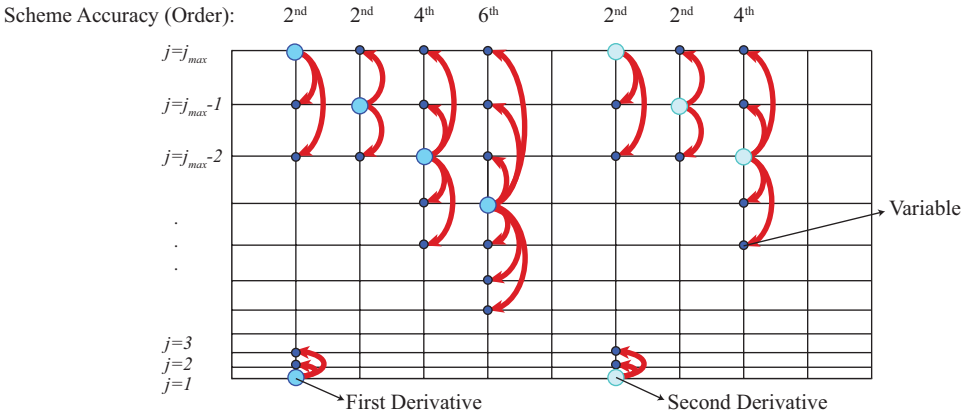


Figure 4.1: Schematic of the two-dimensional computational grid. The spatial discretization schemes are illustrated for the calculation of first and second derivatives, along the wall-normal direction.

A generalized conservative approximation method, proposed by Pirozzoli [24] is employed for the evaluation of the convective terms. This method is based on the application of standard central finite difference schemes on split forms of the convective terms, guaranteeing numerical stability and high energy conservation. This implies that no additional filters need to be applied, making the simulations more computationally efficient.

For the temporal integration an explicit third-order Runge-Kutta scheme is used, as formulated below;

$$\frac{\mathrm{d}f}{\mathrm{d}t} = f'(t,f),$$
$$f_{n+1} = f_n + \frac{1}{6}\Delta t(k_1 + 2k_2 + k_3), \tag{4.2}$$

with $\Delta t$ being the time step and terms $k_i$ defined as;

$$k_1 = f'\left(t_n, f_n\right),$$
$$k_2 = f'\left(t_n + \frac{\Delta t}{2}, f_n + k_1\frac{\Delta t}{2}\right),$$
$$k_3 = f'\left(t_n + \Delta t, f_n - k_1\Delta t + 2k_2\Delta t\right).$$

## 4.2. BOUNDARY CONDITIONS

Many applications of direct numerical simulations are performed using periodic boundary conditions, as is the case of a fully turbulent channel flow. However, boundary layer flows cannot be simulated using this kind of boundary conditions since spacial periodicity is not exhibited by the flow. For the simulation of non-periodic flows, inlet and outlet boundaries must be treated accordingly. To determine the appropriate equations that can be applied at the flow boundaries, an inviscid characteristic wave analysis was first carried out by Thompson [35] and later, Poinsot and Lele [26] derived a formulation that can be easily implemented in direct numerical simulations, considering ideal gas flows. A generalized form of the boundary conditions is provided by Nora Okongo and Josette Bellan [23], allowing the utilization of characteristic wave boundary conditions for non-ideal gas simulations. The methods developed by these authors is implemented for the purposes of this study, along with some alternatives which are also presented in this section.

### 4.2.1. INVISCID CHARACTERISTIC WAVE ANALYSIS

The main purpose of the characteristic analysis is to provide an alternative method of calculating the convective terms at the domain boundaries, since their exact calculation requires information from the outside the computational domain. The convective terms are expressed in terms of characteristic wave amplitude variations with information obtained from the interior of the domain and the conservation equations are solved at the boundaries.

The amplitude variations of characteristic waves crossing a boundary are expressed by $\mathscr{L}_i$. For waves travelling along the stream-wise direction, they are calculated using

the following expressions:

$$\mathscr{L}_1 = \lambda_1 \left( \frac{\partial p}{\partial x} - \rho c \frac{\partial u}{\partial x} \right), \tag{4.3}$$

$$\mathscr{L}_2 = \lambda_2 \left( \frac{\partial p}{\partial x} - c^2 \frac{\partial \rho}{\partial x} \right), \tag{4.4}$$

$$\mathscr{L}_3 = \lambda_3 \frac{\partial v}{\partial x}, \tag{4.5}$$

$$\mathscr{L}_4 = \lambda_4 \frac{\partial w}{\partial x}, \tag{4.6}$$

$$\mathscr{L}_5 = \lambda_5 \left( \frac{\partial p}{\partial x} + \rho c \frac{\partial u}{\partial x} \right), \tag{4.7}$$

with $\lambda_i$ being the wave velocities given by:

$$\lambda_1 = u - c, \tag{4.8}$$

$$\lambda_2 = u, \tag{4.9}$$

$$\lambda_3 = u, \tag{4.10}$$

$$\lambda_4 = u, \tag{4.11}$$

$$\lambda_5 = u + c. \tag{4.12}$$

For sub-sonic flows, sound waves travel at velocities $\lambda_1$ and $\lambda_5$ in the negative and positive stream-wise direction, $\lambda_2$ is the velocity of entropy waves and $\lambda_3$ and $\lambda_4$ are the velocities at which $v$ and $w$ will travel. The spatial derivatives that are present in these expressions, are calculated using one-sided schemes so that information from the interior domain is obtained.

To incorporate the wave amplitude variations in the flow conservation equations, vector $\boldsymbol{d}$ is introduced and is calculated by,

$$d_1 = \frac{1}{c^2} \left( \frac{\mathscr{L}_5 + \mathscr{L}_1}{2} - \mathscr{L}_2 \right), \tag{4.13}$$

$$d_2 = \frac{\mathscr{L}_5 - \mathscr{L}_1}{2\rho c}, \tag{4.14}$$

$$d_3 = \mathscr{L}_3, \tag{4.15}$$

$$d_4 = \mathscr{L}_4, \tag{4.16}$$

$$d_5 = \frac{\mathscr{L}_2}{c^2}. \tag{4.17}$$

The elements of $\boldsymbol{d}$ are used to substitute the corresponding convective terms in equations (2.1), hence at a boundary that is normal to the stream-wise direction, the conservation equations become,

$$\frac{\partial \rho}{\partial t} + d_1 + \frac{\partial (\rho v)}{\partial y} + \frac{\partial (\rho w)}{\partial z} = 0, \tag{4.18}$$

$$\frac{\partial (\rho u)}{\partial t} + u d_1 + \rho d_2 + \frac{\partial (\rho uv)}{\partial y} + \frac{\partial (\rho uw)}{\partial z} = \frac{\partial \tau_{1j}}{\partial x_j}, \tag{4.19}$$

$$\frac{\partial (\rho v)}{\partial t} + u d_1 + \rho d_3 + \frac{\partial (\rho vv)}{\partial y} + \frac{\partial (\rho vw)}{\partial z} = -\frac{\partial p}{\partial y} + \frac{\partial \tau_{2j}}{\partial x_j}, \tag{4.20}$$

$$\frac{\partial (\rho w)}{\partial t} + u d_1 + \rho d_4 + \frac{\partial (\rho wv)}{\partial y} + \frac{\partial (\rho ww)}{\partial z} = -\frac{\partial p}{\partial z} + \frac{\partial \tau_{3j}}{\partial x_j}, \tag{4.21}$$

$$\frac{\partial (\rho E)}{\partial t} + h_t d_1 + \frac{\partial (\rho h_t v)}{\partial y} + \frac{\partial (\rho h_t w)}{\partial z} + \rho u d_2 + \rho v d_3 + \rho w d_4 + \frac{C_p}{\alpha_V} d_5 = \frac{\partial (u_i \tau_{ij})}{\partial x_j} - \frac{\partial q_j}{\partial x_j}, \tag{4.22}$$

with $h_t$ the total enthalpy, calculated as $h_t = E + p/\rho$ and $\alpha_V$ the thermal expansion coefficient given by $\alpha_V = 1/V(\partial V/\partial T)_p$ with $V$ being the specific volume. It is worth mentioning that the pressure gradient along the stream-wise direction $\partial p/\partial x$ is accounted for while calculating $d_2$ and is not included in equation (4.19). It is noted that for waves crossing boundaries normal to other directions, the above equations need to be adjusted accordingly, by taking the derivatives along the desired direction and substituting the corresponding convective terms in equations (2.1).

### 4.2.2. IMPLEMENTATION

Depending on the *type* of boundary condition, the calculation of $\mathscr{L}_i$ might differ from equations (4.4) to (4.7). Also for some cases, some of the equations (4.18) to (4.22) are not used to advance the solution in time. The different types of boundary conditions are presented below.

- **Inlet boundary conditions**

  At the inlet of the domain *two* different methods are utilised for the implementation of the of boundary conditions. The influence of each method on the results if the simulations is discussed in later chapters. The first method is primarily based on *inviscid characteristic wave analysis* and is referred to as *Non-Reflective* boundary condition or *NRBC*, for brevity. The other method employs interpolation of variables from the interior domain to advance the inlet variables in time, in this study referred to as the *Standard* boundary condition.

  1. **Non-Reflective Condition**

     The density $\rho$ and all velocity components $u_i$ are kept fixed, hence equations (4.18) to (4.21) are not used to advance the variables in time.

     Amplitude variation of $\mathscr{L}_1$ is determined from equation (4.4) and the interior, since this is the only wave that travels outside of the domain. All other amplitude variations are set to zero except from $\mathscr{L}_5$ which is set to be $\mathscr{L}_5 = \mathscr{L}_1$.

     Equation (4.22) is used to advance $\rho E$ in time.

2. **Standard Condition**

   This method is implemented as described in [39] and [40] and is only applicable to boundary layer simulations.

   Velocity components at the inlet are kept fixed and the pressure is extrapolated from the interior domain using second-order extrapolation close to the wall and zeroth-order in the free-stream, as described by the following equations:

$$p(x_{i=1}) = b_1 p(x_{i=2}) + b_2 p(x_{i=3}) + b_3 p(x_{i=4}), \tag{4.23}$$
$$\boldsymbol{b} = [1 - u(x_{i=1})]\boldsymbol{b_w} + u(x_{i=1})\boldsymbol{b_{fs}},$$

   where $\boldsymbol{b_w} = [3\ -3\ 1]$ and $\boldsymbol{b_{fs}} = [1\ 0\ 0]$.

   - For an adiabatic wall, density $\rho$ at the inlet is kept fixed and $\rho E$ is advanced in time by using the equation of state, since two thermodynamic properties are known ($\rho$ and $p$).
   - For an isothermal wall, temperature $T$ at the inlet is kept fixed while $\rho$ and $\rho E$ are advanced in time by using the equation of state, provided that $T$ and $p$ are known.

- **No-slip Wall Boundary Conditions**

  The wall boundary conditions are implemented in a similar manner as the inlet boundary conditions. A *Fully-Reflective* condition is considered, which is based on inviscid characteristic wave analysis along with a Standard condition. For both of these conditions, all velocity components are set to zero, since a no-slip condition applies, hence equations (4.19) to (4.21) are not used.

  1. **Fully-Reflective Condition**

     Since the wall-normal velocity component $v_w$ is equal to zero, $\mathscr{L}_2 = \mathscr{L}_3 = \mathscr{L}_4 = 0$. The outgoing wave amplitude variation $\mathscr{L}_1$, is calculated using equation (4.4) and the interior. The reflected wave amplitude is, then, $\mathscr{L}_5 = \mathscr{L}_1$.

     - For an adiabatic wall, the wall normal heat flux in equation (4.22) is equal to zero, as shown below:

$$\frac{\partial T}{\partial y} = 0. \tag{4.24}$$

       To advance $\rho$ and $\rho E$ in time, equations (4.18) and (4.22) are used.
     - For an isothermal wall, since the wall temperature is fixed, equation (4.22) is discarded and only equation (4.18) is used to advance $\rho$ in time.

  2. **Standard Condition**

     This type of boundary condition, also derives from inviscid characteristic analysis, however the implementation does not involve integrating equations (4.18) and (4.22). By equating $\mathscr{L}_5$ to $\mathscr{L}_1$, the following condition results, at the wall:

$$\frac{\partial P}{\partial y} = 0. \tag{4.25}$$

     The pressure at the wall is set so that condition 4.25 is satisfied.

- For an adiabatic wall, the temperature is set so that condition 4.24 is satisfied.
- For an isothermal wall the wall temperature is fixed.

To advance $\rho$ and $\rho E$ in time, the equation of state is used, provided that $p$ and $T$ are known.

- **Outlet Boundary Condition**

  The same type of boundary condition is applied at the top boundary (free-stream) and the outlet. Equations (4.18) to (4.22) are used to advance all the variables in time.

  The wave amplitude variation of the reflected wave is calculated using the following equations:

$$\mathscr{L}_1 = \mathscr{K}(p - p_\infty), \tag{4.26}$$

$$\mathscr{K} = \sigma_{BC}\frac{(1 - Ma_\infty^2)c}{L}, \tag{4.27}$$

  where $p_\infty$ is the value of the free-stream pressure and is assumed to have a constant value, $\sigma_{BC}$ is a constant and $L$ is the domain length in the direction normal to the boundary (i.e. for the outlet $L$ corresponds t $L_x$ and for the free-stream boundary it corresponds to $L_y$). By setting the value of $\sigma_{BC}$ equal to zero, the condition becomes *perfectly non-reflective* since $\mathscr{L}_1$ becomes zero. For the purpose of this study a value of 0.25 is used for the free-stream boundary and 0.0 for the outlet of the domain.

  The other amplitude variations are calculated by equations (4.5) to (4.7) and the interior.

- **Span-wise Boundary Condition**

  In the span-wise direction, it is assumed that the flow is periodic, hence a *periodic boundary condition* is implemented for the case of three-dimensional simulations.

- **Periodic Blowing and Suction**

  In studies of flow stability, it is necessary to artificially introduce periodic blowing and suction (briefly referred to as *perturbation*) inside the computational domain, in order to trigger the physical instabilities that will eventually develop into turbulence. The intensity (amplitude) of the perturbation determines whether the instabilities grow and flow transits to turbulence or decay as predicted by Linear Stability. Large amplitudes might trigger stronger primary instabilities that will later develop to turbulence, following one of the paths mentioned in section 1.3.1, while a small amplitude will trigger weak instabilities that will decay further downstream.

  To implement the perturbation, the flow receives a wall-normal velocity component in a narrow strip between $x_1$ and $x_2$ at the wall, according to the following equations, as used in [30].

$$v_w(x,z,t) = A_1 f(x)\sin(\omega_1 t) + A_2 f(x) g(z)\sin(\omega_2 t), \tag{4.28}$$

$$f(x) = \begin{cases} 15.1875\xi^5 - 35.4375\xi^4 + 20.25\xi^3 & \text{for } x_1 \le x \le x_m \\ -15.1875\xi^5 + 35.4375\xi^4 - 20.25\xi^3 & \text{for } x_m \le x \le x_2 \end{cases}, \tag{4.29}$$

$$\xi = \begin{cases} \frac{x-x_1}{x_m-x_1} \text{ for } x_1 \le x \le x_m \\ \frac{x_2-x}{x_2-x_m} \text{ for } x_m \le x \le x_2 \end{cases}, \tag{4.30}$$

$$g(z) = \cos\left(\frac{2\pi z}{\lambda_0}\right), \tag{4.31}$$

where $x_m = (x_1 + x_2)/2$, $\omega_1$ is the fundamental angular frequency of oscillation and $\omega_2$ is an additional frequency which can be a harmonic of $\omega_1$ and $\lambda_0$ is the spanwise wavenumber. In two-dimensional simulations the second term of equation (4.28) is neglected.

Angular frequency $\omega$ is related to the dimensionless frequency $F$, as follows

$$F = \frac{2\pi F^* \mu^*_\infty}{\rho^*_\infty U^{*2}_\infty} = \frac{\omega}{Re_\infty}. \tag{4.32}$$

The time step that is used for time integration is based on the fundamental angular frequency of the perturbation, so that the an equal amount of samples of the flow fields is saved during each forcing period.

$$\Delta t = \frac{2\pi}{K_t \omega_1}. \tag{4.33}$$

Factor $K_t$ is a multiple of the amount of samples that is saved during each forcing period and is selected so that the resulting $CFL$ number [5] of the simulation is 0.8, at maximum, which implies numerical stability.

## 4.3. COMPUTATIONAL SPONGE IMPLEMENTATION

Because the derivation of inviscid characteristic boundary conditions, relies heavily on the assumption of an inviscid flow, inlet and outlet boundary conditions are not completely non-reflective. In fact they might introduce non-physical oscillations that affect the flow field. To tackle this issue, computational *sponges* are introduced at the boundaries, to damp the incident and reflected waves. Sponges are implemented by adding one extra term in right-hand side of each of the conservation equations (2.1), as shown below:

$$\left.\begin{aligned} \frac{\partial \rho}{\partial t} + \frac{\partial (\rho u_j)}{\partial x_j} &= \sigma\left(\rho_{ref} - \rho\right), \\ \frac{\partial (\rho u_i)}{\partial t} + \frac{\partial (\rho u_i u_j + p\delta_{ij} - \tau_{ij})}{\partial x_j} &= \sigma\left[(\rho u_i)_{ref} - \rho u_i\right], \\ \frac{\partial (\rho E)}{\partial t} + \frac{\partial (\rho E u_j + p u_j + q_j - u_i \tau_{ij})}{\partial x_j} &= \sigma\left[(\rho E)_{ref} - \rho E\right], \end{aligned}\right\} \tag{4.34}$$

where all reference values are the base flow values and $\sigma$ is the sponge *damping coefficient*, which is a function of $x$ or $y$, depending on which direction the damped waves are travelling towards. In this case $\sigma$ is selected to have a quadratic profile, hence for a sponge acting close to the outlet, it is given by,

$$\sigma(x) = \sigma_{max}\left(\frac{x - L_x + L_{sp}}{L_{sp}}\right)^2 \text{ for } x \geq L_x - L_{sp}, \tag{4.35}$$

where $L_{sp}$ is the sponge length. Equation (4.35) suggests that $\sigma$ increases towards the outlet, where the maximum damping occurs. For a sponge that is acting close to the inlet, equation (4.35) is modified so that the maximum $\sigma$ value corresponds to the inlet.

To measure the total sponge strength, Ali Mani [18] introduces $\eta_{targ}$ which is calculated by

$$\eta_{targ} = -20\frac{2\log e}{1 - Ma_\infty^2}\int_0^{L_{sp}} \sigma(x)dx, \tag{4.36}$$

and expresses the sound-sound target reflectivity of the sponge in $dB$. For a quadratic sponge, expression (4.36) becomes,

$$\eta_{targ} = -20\frac{2\log e}{1 - Ma_\infty^2}\left(\frac{\sigma_{max}L_{sp}}{3}\right). \tag{4.37}$$

The effect of varying $\eta_{targ}$ on the resulting flow fields is discussed in later chapters. In the present study, sponges are applied at the inlet, the outlet and free-stream boundaries.

## 4.4. THERMODYNAMIC PROPERTIES

To fully define the thermodynamic conditions of the flow $\rho$ and $E$ are used since they are calculated by integrating equations (2.1). As mentioned in section 3.1.2, results are presented for both ideal and non-ideal gases, hence both cases are implemented in the `FORTRAN` code.

### 4.4.1. IDEAL GAS EQUATION OF STATE

For ideal gases equations (3.5) are used to calculate thermodynamic properties and equation (3.6) is used to calculate viscosity, in their dimensionless form. However, since the integration of conservation equations provides $\rho E$ and $\rho$, the temperature is calculated using

$$T = \frac{\gamma - 1}{R}E. \tag{4.38}$$

Thermal conductivity $\kappa$ is calculated by assuming constant $Pr$ and $C_p$ in the whole domain, hence

$$\kappa = \frac{\gamma R}{(\gamma - 1)Pr_\infty}\mu. \tag{4.39}$$

### 4.4.2. TWO-DIMENSIONAL TABLE INTERPOLATION FOR NON-IDEAL GASES

For the simulation of non-ideal boundary layer flows, a *table interpolation* tool is developed for *two dimensional* tables. Interpolations are performed using $4^{th}$ order Lagrange

polynonomials in two directions, to calculate the thermodynamic ($h$, $T$, $p$, $C_p$ and $\alpha_V$) and transport ($\mu$, $\kappa$ and $c$) properties that are required, provided $\rho$ and $E$.

Tables are generated using A `MATLAB` script was developed for the generation of the tables that contain the thermodynamic properties which utilizes data from `REFPROP` library and *GERG 2004* equation of state. The range and resolution of the tables are adjusted suitably for each case, ensuring the desired accuracy. Examples of the generated tables are presented in figure 4.2 in contour form. Tables are generated according to the following procedure.

1. Vectors are generated containing the desired $\rho^*$ and $E^*$ values, referred to as $\boldsymbol{\rho}_{\boldsymbol{v}}^*$ and $\boldsymbol{E}_{\boldsymbol{v}}^*$.

2. A vector containing $T^*$ ranging from 220 $K$ to 500 $K$ is generated with $\Delta T^* = 0.1$ $K$ (which is a high resolution). This vector is referred to as $\boldsymbol{T}_{\boldsymbol{v}}^*$

3. The saturation line is calculated as a function of $\boldsymbol{\rho}_{\boldsymbol{v}}^*$ and $\boldsymbol{T}_{\boldsymbol{v}}^*$, resulting to a new vector $\boldsymbol{T}_{\boldsymbol{sat}}^*$.

4. For each element of $\boldsymbol{\rho}_{\boldsymbol{v}}^*$, all the values of $\boldsymbol{T}_{\boldsymbol{v}}^*$ that are greater than the corresponding value of $\boldsymbol{T}_{\boldsymbol{sat}}^*$ are provided to `REFPROP`. This is necessary, since directly providing a pair of $\rho^*$ and $E^*$, introduces convergence issues near the saturation line. The values of $E^*$ and all the desired thermodynamic and transport properties are returned. At this point a vector $\boldsymbol{E}_{\boldsymbol{interp}}^*$ is generated, which is a function of one element of $\boldsymbol{\rho}_{\boldsymbol{v}}^*$ and all the elements of $T_v^*$. All other properties are also stored in the same manner, i.e. $\boldsymbol{p}_{\boldsymbol{interp}}^*$ is the vector that contains $p^*$ as a function of $\boldsymbol{T}_{\boldsymbol{v}}^*$ and one particular $\rho^*$ value.

5. Each vector that contains a property as a function of $\boldsymbol{T}_{\boldsymbol{v}}^*$, is interpolated on the $\boldsymbol{E}_{\boldsymbol{v}}^*$ vector, using the $\boldsymbol{E}_{\boldsymbol{interp}}^*$ vector. This is repeated for all the values of $\boldsymbol{\rho}_{\boldsymbol{v}}^*$.

6. The saturation line is calculated as a function of $\boldsymbol{\rho}_{\boldsymbol{v}}^*$ and $\boldsymbol{E}_{\boldsymbol{v}}^*$, resulting to a new vector $\boldsymbol{E}_{\boldsymbol{sat}}^*$.

7. For each value of $\boldsymbol{\rho}_{\boldsymbol{v}}^*$, the tables are filled with zeros for every value of a property that corresponds to $E^* < E_{sat}^*$.

At the boundaries of the computational domain, it is necessary to define the thermodynamic state, based on a different pair of properties, other than $\rho$ and $E$. In the case where one of these properties ($\rho$ or $E$) is known, it is possible to perform the interpolation using the table of figure 4.2a, if $p$ is the second known property or 4.2b, if $T$ is the second known property.

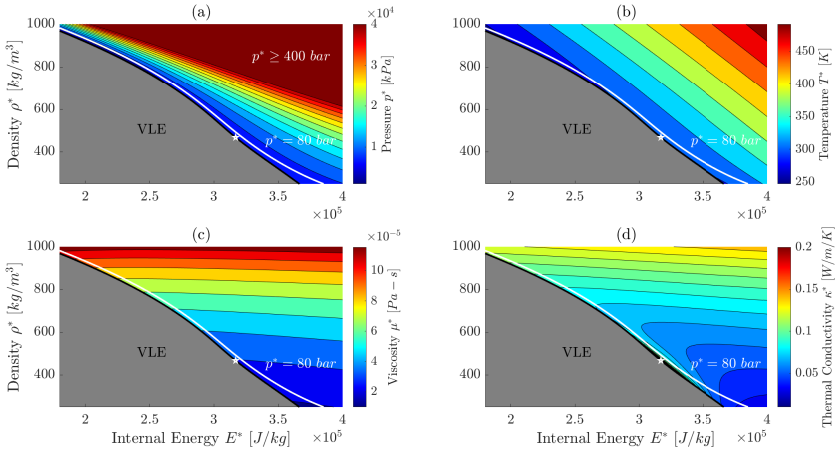


Figure 4.2: Graphical representation of two-dimensional property tables for Carbon Dioxide. Properties are plotted as functions of fluid density $\rho^*$ and internal energy $E^*$. Contours correspond to (a) pressure $p^*$, (b) temperature $T^*$, (c) viscosity $\mu^*$ and (d) thermal conductivity $\kappa^*$. The white line indicates the 80 $bar$ isobar and ($\star$) the *Supercritical Point*.

In the case that neither $\rho$ nor $E$ are known, it is necessary to use a table that contains $p^*$ as a function of $\rho*$ and $T^*$, as shown in figure 4.3. For known $T$ and $p$, it is possible to calculate $\rho$ and using the table of figure 4.2b $E$ is computed. Once both $\rho$ and $E$ are known, it is possible to interpolate for all the thermodynamic and transport properties required.

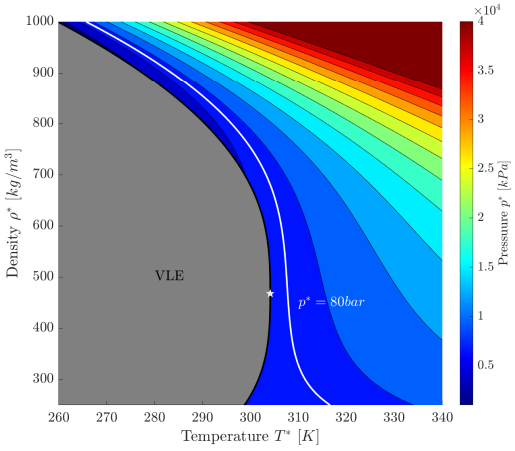


Figure 4.3: Graphical representation of two-dimensional property tables for carbon dioxide. Pressure $p^*$ is plotted as a function of fluid density $\rho^*$ and temperature $T^*$. The white line indicates the 80 $bar$ isobar and ($\star$) the *Supercritical Point*.

# 5

# IDEAL GAS SIMULATIONS

In this chapter, results are presented for the simulations of an *Ideal Gas* boundary layer for atmospheric air. The main purpose of this chapter is to investigate how the utilization of different computational implements (boundary conditions, sponges and grid-related parameters), affects the results of the direct numerical simulations. This is performed by comparing the post-processed results with the growth rate $\alpha_i$ profile that is calculated from Linear Stability Theory or by examining and comparing the flow profiles that are calculated in each case. For the purpose of this investigation, *one* set of flow conditions is selected and the simulations are performed with varying values associated with the computational implements. The guidelines that are determined will, then, be followed to perform the non-ideal gas simulations, which will be presented in the next chapter.

## 5.1. SELF-SIMILAR SOLUTION AND FLOW PARAMETERS

For the simulations presented this chapter, a boundary layer over an *adiabatic* wall is selected with $T^*_\infty = 300\ K$, $Pr_\infty = 0.75$ and $\gamma = 1.4$. Figure 5.1 provides the self-similar solutions of flows characterized by these parameters, with varying $Ec_\infty$, as a reference.

From the plots of figure 5.1, it is evident that viscous heating, increases the wall temperature. This effect becomes more intense with increasing $Ec_\infty$. Temperature increase, leads to a drop in density, making compressibility effects more significant for larger $Ec_\infty$. The viscosity follows an exponential relationship with temperature, as suggested by Sutherland's law in equation (3.6), hence it increases with temperature. As a result, the boundary layer thickness increases for greater $Ec_\infty$ values.

To perform the Direct Numerical simulations, the case of $Ec_\infty = 0.05$ is selected, and marked in figure 5.1 with a red solid line. For this case, compressibility effects are minor, which is justified by the relatively low $Ma_\infty$, which has a value of 0.35. This is a case of sub-sonic flow, which is, also, suitable for studying the effectiveness of inviscid characteristic wave boundary conditions.

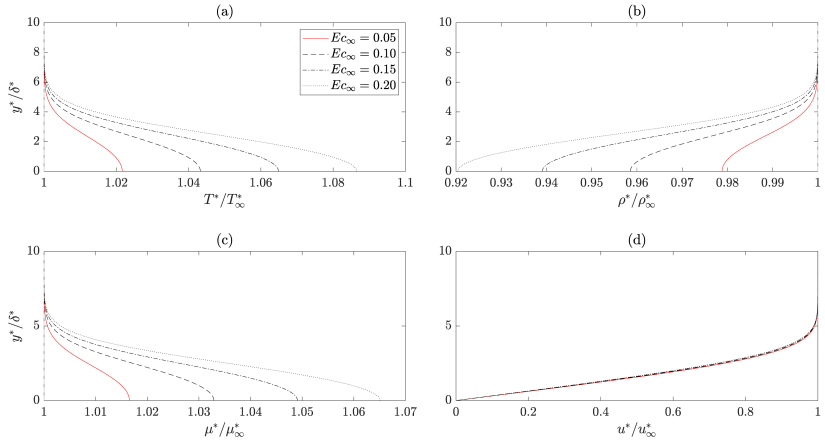


Figure 5.1: Self-similar solutions for Ideal Gas at $T^*_\infty = 300K$, $Pr_\infty = 0.75$ and $\gamma = 1.4$. Panels contain (a) temperature, (b) density, (c) viscosity and (d) stream-wise velocity, normalized by the free-stream values, as functions of the wall-normal coordinate $y^*$ normalized by $\delta^*$.

## 5.2. POST-PROCESSING

Once the DNS are completed, the following procedures are followed for the processing of the resulting data, so that they can be compared to the LST predictions. To avoid confusion, it is noted that the stream-wise and wall-normal locations in the LST are determined by $Re_\delta$ and $y^*/\delta^*$, respectively, whereas in the DNS by $x^*/\delta^*_{99,in}$ and $y^*/\delta^*_{99,in}$. To compare the results between the two methods, the coordinates are transformed accordingly.

### 5.2.1. CALCULATION OF FLUCTUATION AMPLITUDE AND GROWTH RATE

To compare the results of the direct numerical simulations with the results of the LST, it is first necessary to analyse the flow fields after the flow has reached temporal *periodicity*. Periodicity is achieved when the simulations run for a sufficient amount of time steps, which varies according to the case. To determine whether this is achieved, the flow fields are Fourier-transformed and observed until the amplitude of the subharmonic is at least one order of magnitude lower than the fundamental perturbation.

Once a periodic solution is reached, one hundred samples of each quantity are averaged within two forcing periods to obtain the *mean profile* $q_0$. To obtain the fluctuation $q'$ of a variable, the mean profile is subtracted from each sample. Fluctuations are Fourier-transformed in time to obtain the fluctuation amplitude $|\hat{q}|_1$ at every location within the domain. Subscript 1 corresponds to the fundamental mode, that inherits the frequency of the perturbation.

To calculate the growth rate of instabilities $\alpha_i$ in the stream-wise direction, the following equation is used,

$$\alpha_i(x) = -\frac{Re_\delta}{Re_\infty}\frac{1}{|\hat{q}|_1^{max}}\frac{\partial |\hat{q}|_1^{max}}{\partial x}, \tag{5.1}$$

where $|\hat{q}|_1^{max}$ stands for the maximum amplitude fluctuation along the $y$ direction, at

one specific $x$ location.

### 5.2.2. FILTERING

In certain occasions, the resulting growth rate profiles exhibit oscillatory features which are filtered out. To perform the filtering, local averaging of the fluctuation amplitude is utilized, along the stream-wise direction according to the following equation,

$$|\hat{q}|_{1,i}^{filtered} = \frac{1}{2N+1} \sum_{c=-N}^{N} |\hat{q}|_{1,i+c}^{unfiltered}, \tag{5.2}$$

where index $i$ corresponds to the index of the grid point in the stream-wise direction and $N$ is a constant that corresponds to the number of points that the are used for the averaging in one direction. For this study $N = 3$, hence the averaging is performed by utilizing three points behind and three points ahead of point $i$.

## 5.3. REFERENCE VALUES FOR DNS AND VALIDATION OF GROWTH RATE PREDICTED BY LST

For all the cases that are presented in this chapter, the values presented in table 5.1 are used, changing one value at a time, to investigate how the results will be affected. The case that utilizes the values of table 5.1 unchanged, is called the *Reference Case*.

Table 5.1: Values Used for the Direct Numerical Simulation of the Reference Case.

| **Computational Grid Values** | | | **Time Stepping** | |
|---|---|---|---|---|
| $L_x$ | | 967.95 | $K_t$ | 20000 |
| $L_y$ | | 20.0 | $n_{steps}$ | 1000000 |
| $n_x$ | | 2112 | **Perturbation Related Parameters** | |
| $n_y$ | | 200 | $F$ | $33 \times 10^{-6}$ |
| $S_f$ | | 4.0 | $A_1$ | $0.5 \times 10^{-6}$ |
| **Computational Sponge Parameters** | | | $Re_\delta(x_m)$ | 680.0 |
| Inlet | $L_{sp}$ | 20.0 | $x_1 - x_2$ | 11.92 |
| | $\sigma_{max}$ | 0.5 | **Boundary Conditions** | |
| Outlet | $L_{sp}$ | 20.0 | Inlet | Standard, Adiabatic |
| | $\sigma_{max}$ | 0.5 | Wall | Standard, Adiabatic |
| Free-Stream | $L_{sp}$ | 1.0 | Outlet | NRBC, $\sigma_{bc} = 0.0$ |
| | $\sigma_{max}$ | 0.5 | Free-Stream | NRBC, $\sigma_{bc} = 0.25$ |

For the cases presented in this chapter, no filtering was applied during the post-processing, since it would remove features that are investigated in this chapter. The calculation of the growth rate of instabilities $\alpha_i$ is performed using samples for the wall-normal velocity.

The simulation that utilizes all the values of table 5.1, yields results that validate the predicted quantities of the Linear Stability Theory and can be used for the investigation of flow stability. Since all the cases that are presented in this chapter, are compared to

the Reference case, the post-processed results of the simulation are presented in figure 5.2.

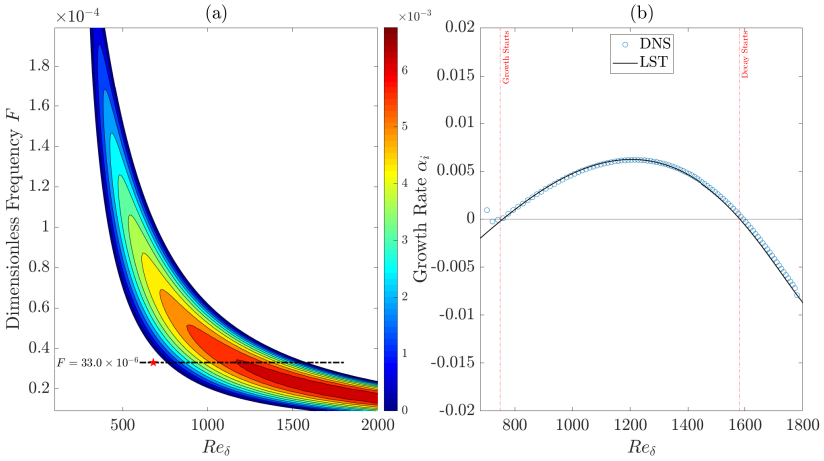


Figure 5.2: (a) Stability diagram for $T^*_\infty = 300K$ and $Ec_\infty = 0.05$. The span of the computational domain in the stream-wise direction is marked by the horizontal dashed line and the location of the perturbation by (⋆). (b) Growth rate profile using DNS and LST for $F = 33.0 \times 10^{-6}$.

To illustrate the development of the instabilities, a contour plot of the wall-normal velocity profile is provided in figure 5.3, which results from the DNS.

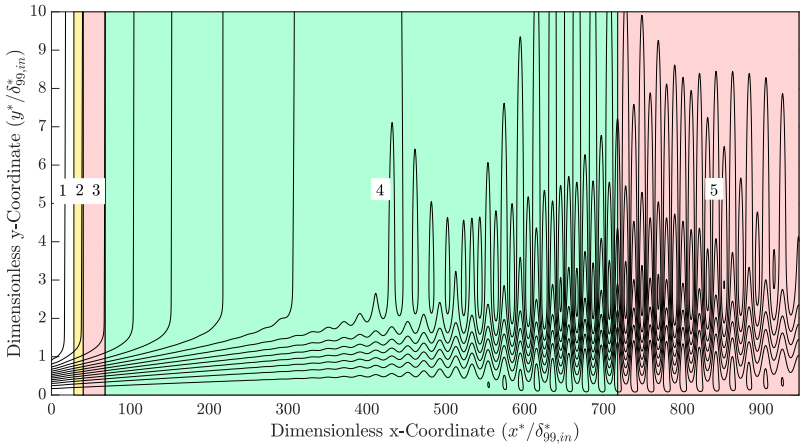


Figure 5.3: Contour lines of wall-normal velocity. The five colored regions correspond to a particular physical behaviour exhibited by the flow.

Five physical regions are identifiable in figure 5.3. At the inlet of the domain (region 1), the flow exhibits unperturbed behaviour. In region 2, the periodic suction and

blowing is introduced, hence the receptivity stage of the flow in which the T-S waves are excited. Modal decay is exhibited in region 3, before reaching modal growth in region 4 where the growth of instabilities starts to follow the LST prediction for positive $\alpha_i$. Finally, in region 5 the instabilities decay, as predicted by the LST in the region of negative $\alpha_i$.

The development of instabilities can, also, be illustrated by plotting the integral of the kinetic energy fluctuation along the y-direction, as shown in figure 5.4. This quantity is calculated by the following expression,

$$I'_{Ek} = \int_0^{L_y} E'_k dy = \frac{1}{2} \int_0^{L_y} \rho'(u'^2 + v'^2) dy, \tag{5.3}$$

where $I'_{Ek}$ stands for the integral of the kinetic energy fluctuation and $E_k$ is the kinetic energy.

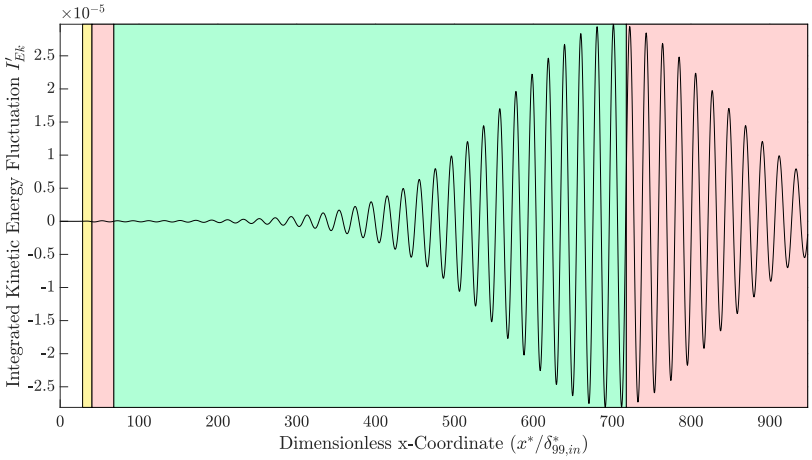


Figure 5.4: Integral of kinetic energy fluctuation $I'_{Ek}$ as a function of the stream-wise coordinate. The five colored regions correspond to a particular physical behaviour exhibited by the flow.

## 5.4. GRID INDEPENDENCY STUDY

To conduct a grid independency study, the spatial grid resolution is varied until the difference between the results becomes insignificant.

Initially, three cases of differing stream-wise resolution are considered. A *coarse mesh* case with $n_x = 1344$, a *medium mesh* case with $n_x = 2112$ and a *fine mesh* case with $n_x = 2880$. The resolution of all three cases in the wall-normal direction remains the same, using $n_y = 200$. To compare the results, the stream-wise growth rate profile that is calculated from the Direct Numerical Simulations is plotted and compared with the profile that is produced from Linear Stability Theory.

From figure 5.5 it is observed that the coarse mesh over-estimates the growth rate predicted by the LST, while with a fine mesh it is under-estimated. For the coarse case,

small oscillatory features are observed on the growth rate profile, which are an indication that the instabilities are not well resolved in the stream-wise direction. The medium mesh matches the growth rate profile, slightly deviating towards the outlet.

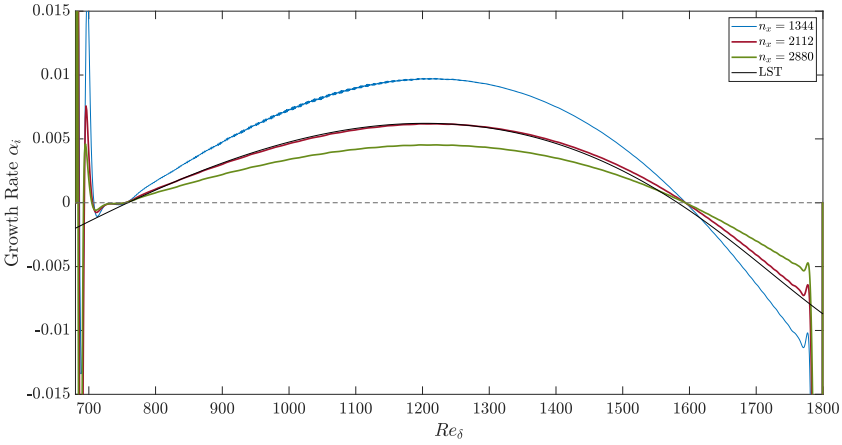


Figure 5.5: Growth rate profile $\alpha_i$ comparison between DNS results for three cases with different stream-wise resolution and LST for $F = 33.0 \times 10^{-6}$.

The real part of eigenvalue $\alpha$, that is calculated by the LST, corresponds to the local wave-number of the fluctuations. The local wavelength $\lambda_w$ is calculated by;

$$\lambda_w = \frac{2\pi}{\alpha_r} \frac{Re_\delta}{Re_\infty}. \tag{5.4}$$

In figure 5.6 $\lambda_w$ is provided as a function of $Re_\delta$.

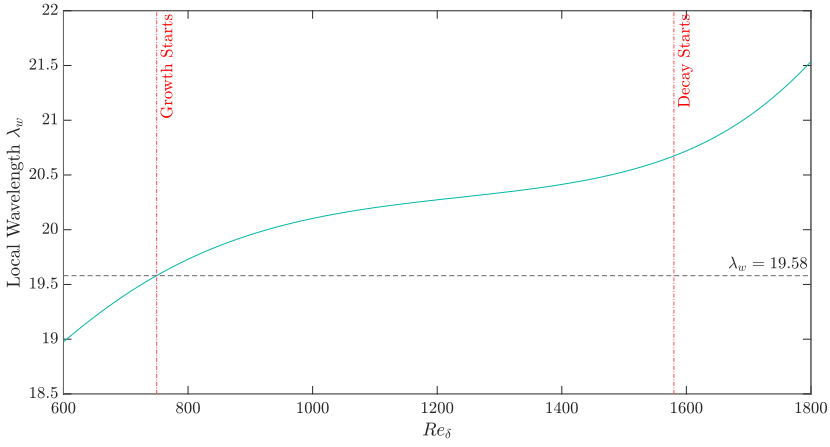


Figure 5.6: Local wavelength of instabilities as a function of $Re_\delta$ calculated by LST for $F = 33.0 \times 10^{-6}$.

Based on figure 5.6, the minimum wavelength that occurs inside the growth zone is $\lambda_{w,min} = 19.58$. For the coarse case, an instability with the minimum wavelength is resolved in 27 points in the stream-wise direction, in 42 for the medium and 58 points for the fine case.

To further investigate the effect that the grid resolution has on the calculation of the growth rate profile, a higher resolution in the wall-normal direction is used for the case of $n_x = 2880$ by making $n_y = 275$. The resulting profiles are presented in figure 5.7

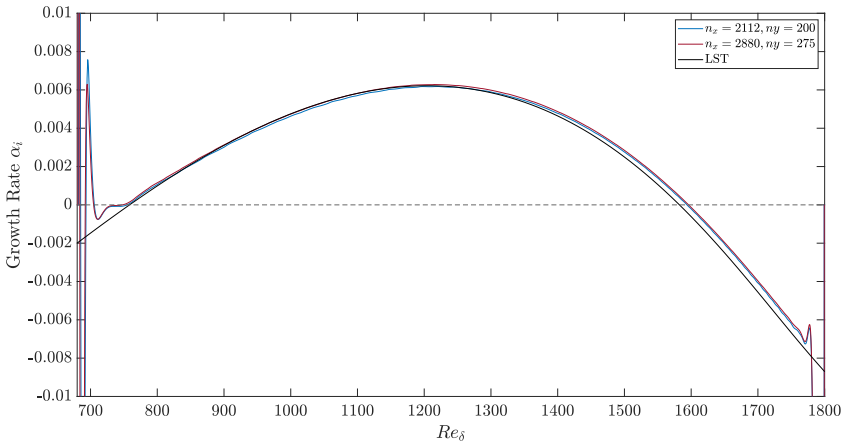


Figure 5.7: Growth rate profile $\alpha_i$ comparison between DNS results for $2112 \times 200$ and $2880 \times 275$ grids and LST for $F = 33.0 \times 10^{-6}$.

By increasing the grid resolution in both directions, the resulting growth rate profile validates the LST predicted profile, again with a slight deviation towards the outlet, which proves that spatial resolution is not the cause of the deviation. By comparing the two curves, a difference of $\sim 3\%$ is calculated. The medium grid case uses 422,400 computational points and the fine grid case uses 792,000 points, requiring almost *twice* the computational power to run the simulation. While improved accuracy is important, in this case the computational cost is relatively high.

## 5.5. INFLUENCE OF DOMAIN HEIGHT

Another factor that affects the results of the DNS is the length of the domain in the wall-normal direction. In this section results are presented for different domain heights by adjusting $L_y$ and $n_y$, maintaining similar spatial resolution.

Three cases are considered in this section. One case has a *low* domain height with $L_y = 8.0$ and $n_y = 80$, the second case has a *medium* domain height with $L_y = 14.0$ and $n_y = 140$ and the third case has a high domain height with $L_y = 20.0$ and $n_y = 200$. Again, the growth rate profile is plotted and the results are compared with the LST predicted profile in figure 5.8.

For the $L_y = 14.0$ case, the growth rate profile is similar to the profile calculated for $L_y = 20.0$ and matches the LST predicted profile. As observed in figure 5.8, low domain

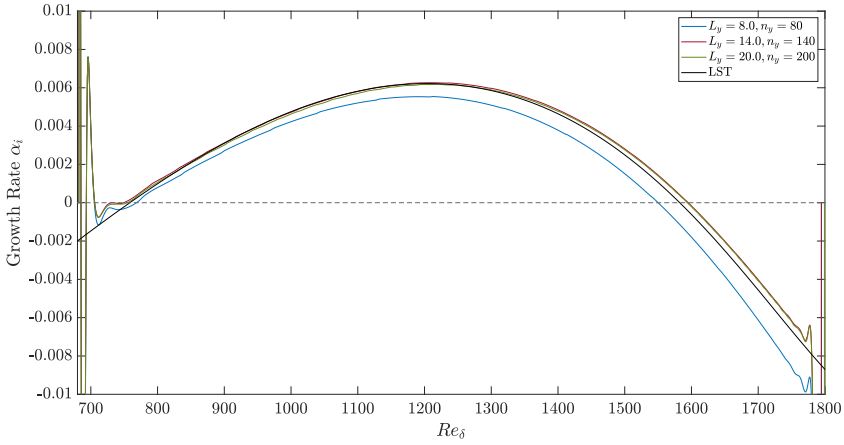


Figure 5.8: Growth rate profile $\alpha_i$ comparison between DNS results for $L_y = 8.0$, $L_y = 14.0$, $L_y = 20.0$ and LST for $F = 33.0 \times 10^{-6}$.

height causes a mismatch between the profiles that are calculated from DNS and LST. This effect can be investigated by looking at the amplitude of the instabilities along the $y$ direction, as shown in figure 5.9. The amplitudes of the fluctuations slightly differ, however since growth is exponential, significant deviation is observed on the growth rate curve.

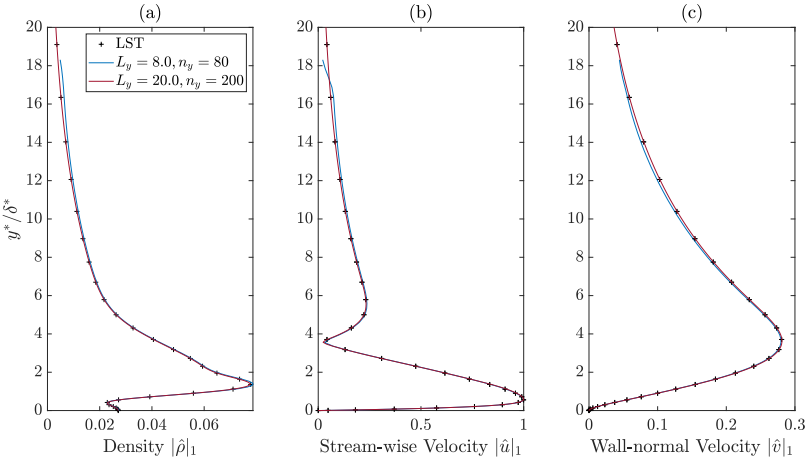


Figure 5.9: Fluctuation amplitude $|\hat{q}|_1$ obtained from DNS with different domain heights. In plots (a) the density fluctuations, in (b) the stream-wise and (c) the wall-normal velocity are presented. Profiles are compared with LST eigenvectors at $Re_\delta = 1300.07$. Values are normalised by the maximum amplitude of the stream-wise velocity $\hat{u}_{max}$. (Note: $L_y = y * /\delta^*_{99,in}$).

The free-stream boundary condition combined with the sponge that is implemented

at the top of the computational domain, causes the suppression of growing instabilities. The two dimensional profiles of $v$ are provided in figure 5.10 to illustrate this effect (case of $L_y = 14.0$ is not illustrated since the profile is similar to the case of $L_y = 20.0$).

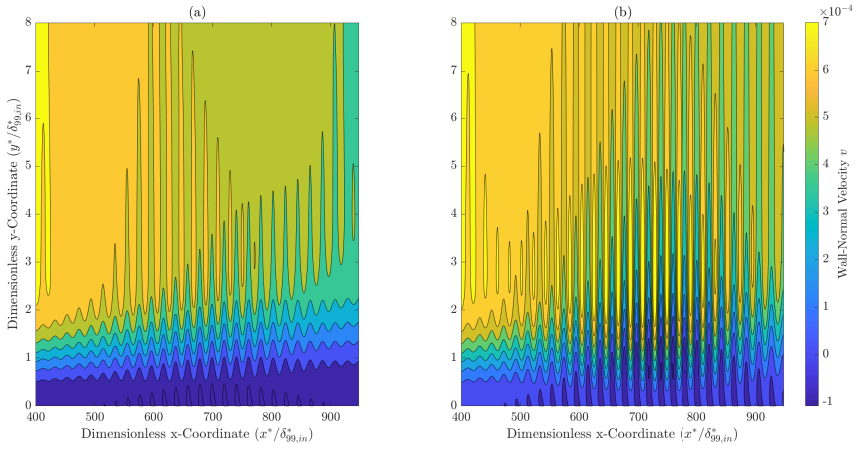


Figure 5.10: Two dimensional profile comparison of wall-normal velocity for (a) $L_y = 8.0$ and (b) $L_y = 20.0$.

These results lead to the conclusion that domain height needs to be large enough so that growing instabilities do not interfere with the free-stream boundary and the top sponge. The threshold domain height at which interference ceases to occur, depends on the flow properties and stability. Additional results are provided in Appendix A for non-ideal gas, supporting this observation.

## 5.6. INFLUENCE OF BOUNDARY CONDITIONS

### 5.6.1. INLET BOUNDARY CONDITIONS

As mentioned in section 4.2, two different methods are considered for the implementation of the inlet boundary conditions. Two simulations are set up, each utilizing a different inlet boundary condition, while both utilize an inlet sponge. To compare the two methods, the growth rate and the pressure fields close to the inlet are plotted.

According to figure 5.11, both methods can be used for the calculation of the growth rate profile. The difference between the profiles calculated with each individual method is $< 0.1\%$.

Figure 5.12 provides information about the pressure close to the inlet of the computational domain, at two different $y$ locations. The pressure exhibits spatial oscillatory behavior in both cases, although for the NRBC case it is more evident and extends for longer inside the domain. However, the amplitude of these oscillations is insignificant compared to the local value of the pressure (amplitude is $< 1 \times 10^{-4}\%$ of the local value). These oscillations do not advance in time, hence they do not influence the calculation of the growth rate. It is, also observed that the oscillations are more evident inside the boundary layer, rather than in the free-stream. This behaviour results from the assump-

tion of inviscid flow in the derivation of characteristic boundary conditions since the flow is highly viscous inside the boundary layer.

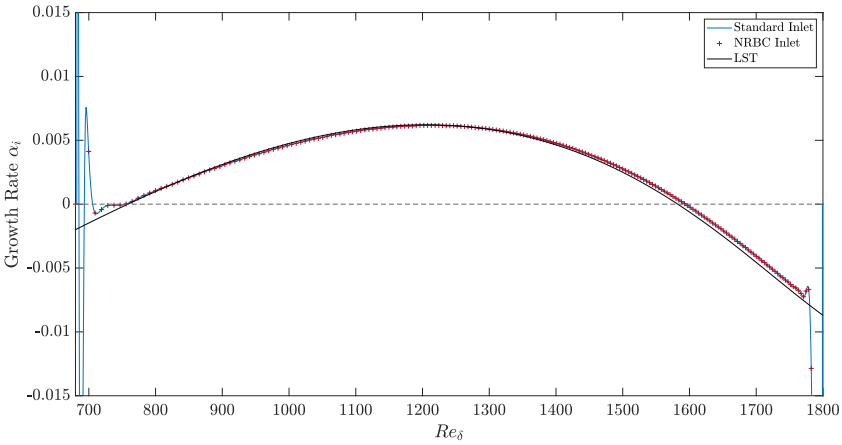


Figure 5.11: Growth rate profile $\alpha_i$ comparison between DNS results for Standard Inlet, NRBC and LST for $F = 33.0 \times 10^{-6}$.

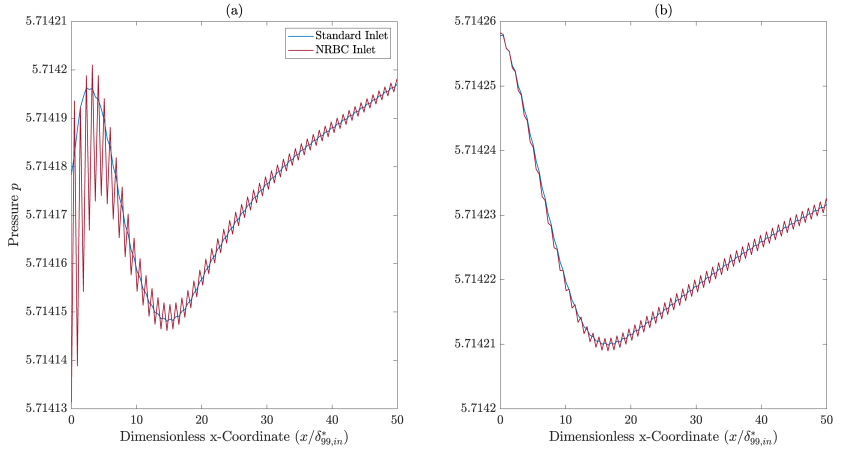


Figure 5.12: Pressure profile comparison for Standard Inlet Boundary Conditions and Non-Reflective Boundary Conditions. Plots (a) corresponds to $y = 0.15$ and (b) to $y = 10.37$.

### 5.6.2. WALL BOUNDARY CONDITIONS

To compare the two types of adiabatic wall boundary conditions (Standard and FRBC), two simulations, each utilizing a different type of boundary condition, are set up. For the comparison of these methods, the growth rate profile is provided for both cases. Addi-

tionally, the wall-normal fluctuation amplitude profiles are plotted for further comparison.

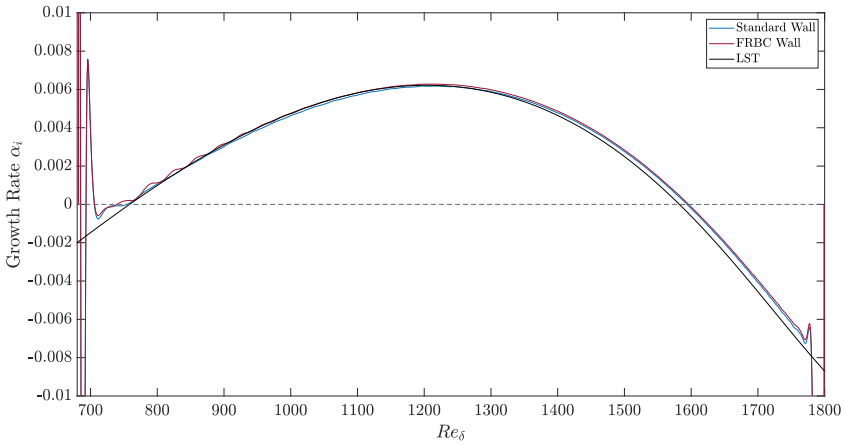


Figure 5.13: Growth rate profile $\alpha_i$ comparison between DNS results for Standard Adiabatic Wall, FRBC and LST for $F = 33.0 \times 10^{-6}$.

As observed in figure 5.13, the utilization of FRBC causes some transient behaviour near the beginning of the growth zone which translates to an oscillatory behaviour in the growth rate profile. The Standard condition matches the LST predicted profile without causing amplitude variations in the flow. It can, also, be observed that the growth rate calculated using an FRBC is slightly higher than using a Standard condition.

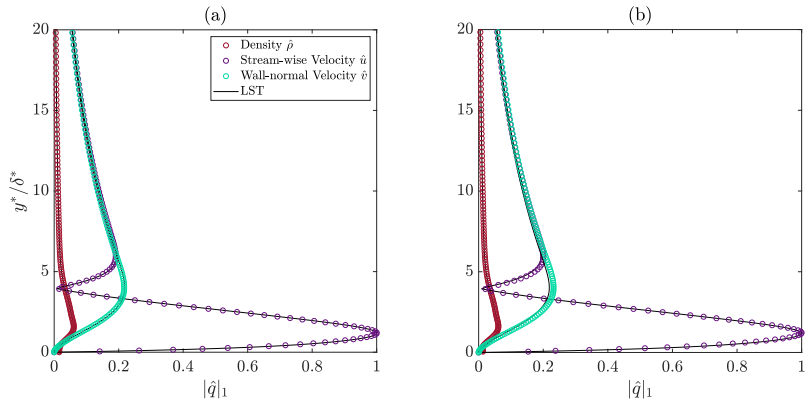


Figure 5.14: Fluctuation amplitude $|\hat{q}|_1$ obtained from DNS using (a) Standard Condition and (b) FRBC at the bottom of the computational domain. Profiles are compared with LST eigenvectors at $Re_\delta = 876.37$. Values are normalised by the maximum amplitude of the stream-wise velocity $\hat{u}_{max}$.

To further investigate the cause of the oscillations in the growth rate profile, the amplitudes of the fluctuations along the $y$-direction for the two cases are provided and validated with the eigenvectors from LST, in figure 5.14.

Although slight differences might be observed between the two cases, the amplitudes of the fluctuations are matched to the LST predicted profiles. By plotting the Fourier transformation of one of the flow variables, it is possible to determine whether unwanted noise is introduced into the sampled time period. The Fourier transformation for the density $\rho'$ in the two cases is presented in figure 5.15.

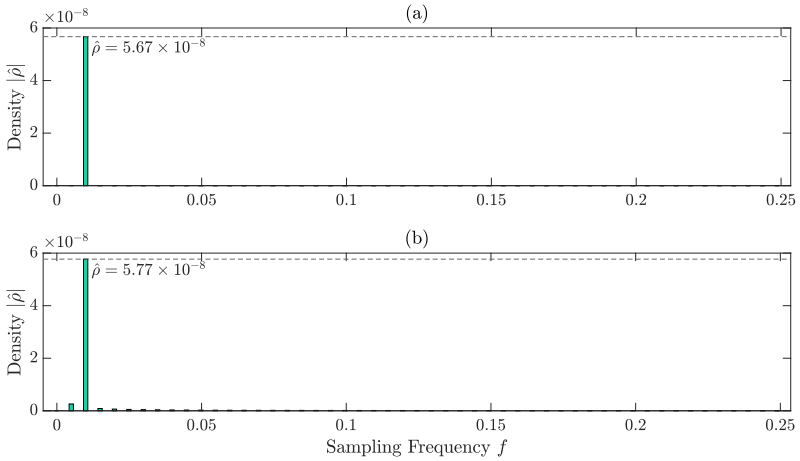


Figure 5.15: Fourier transformation of $\rho'$ for DNS using (a) Standard Condition and (b) FRBC at the bottom of the computational domain at $Re_\delta = 876.37$ and $y = 1.19$.

Based figure 5.15 it can be inferred that using an FRBC introduces numerical noise in the simulation, which is not the case for the Standard condition. In figure 5.15a all the harmonics have decayed, leaving only the fundamental mode, which allows for a correct estimation of the amplitude. The same does not occur in 5.15b, where some spectral leakage is observed indicating the presence of noise in the sampled period, leading to a less accurate calculation of the amplitude of the perturbation.

## 5.7. INFLUENCE OF COMPUTATIONAL SPONGES

### 5.7.1. INLET SPONGE

To investigate the influence of including a sponge at the inlet of the domain, two simulations are set up. One simulation utilizes a sponge at the inlet, while the other does not. For comparison, the growth rate profiles are presented for each simulation, as well as the pressure profiles close to the inlet of the domain. The values for $\eta_{targ}$ that are presented in this section are calculated using equation 4.36.

The utilization of a sponge at the inlet of the domain does not influence the resulting growth rate of instabilities, as shown in figure 5.16. The percentage difference between the results of the two simulations is $< 0.1\%$. Pressure profiles at the domain inlet are

compared in figure 5.17.

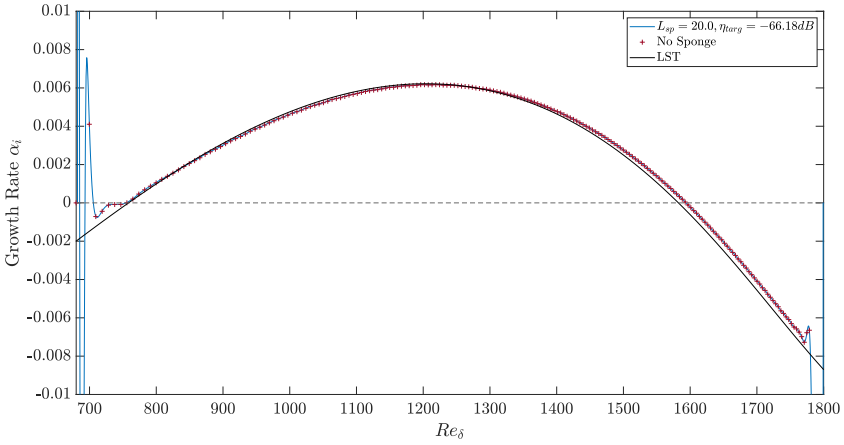


Figure 5.16: Growth rate profile $\alpha_i$ comparison between DNS results with an active and inactive sponge at the inlet and LST for $F = 33.0 \times 10^{-6}$.

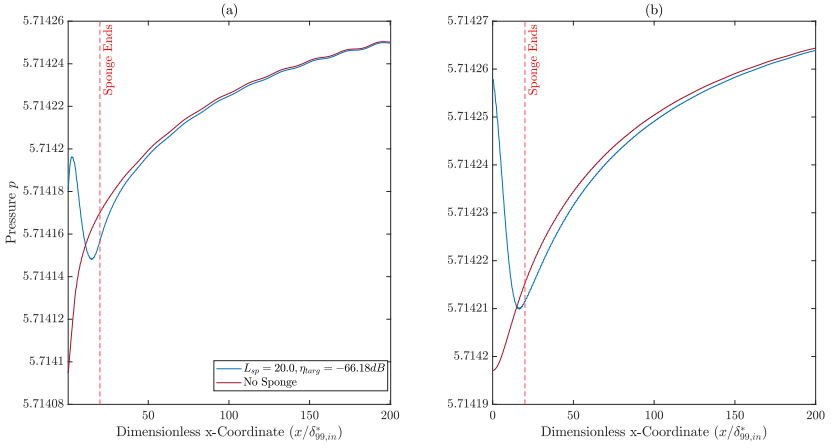


Figure 5.17: Pressure profile comparison for active and inactive inlet sponge. Plots (a) corresponds to $y = 0.15$ and (b) to $y = 10.37$.

The inlet pressure differs slightly ($\sim 0.001\%$) at the boundary between the two cases, and converges further downstream. A pressure drop is, also, observed in the region where the sponge is present. This mismatch appears to be insignificant and constant in time, hence not influencing the calculation of the growth rate.

### 5.7.2. FREE-STREAM SPONGE

Two simulations are compared to examine the impact of including a sponge at the top of the computational domain. Again, one simulation utilizes a sponge while the other does not. For comparison the growth rate profile is provided for the two cases in figure 5.18.

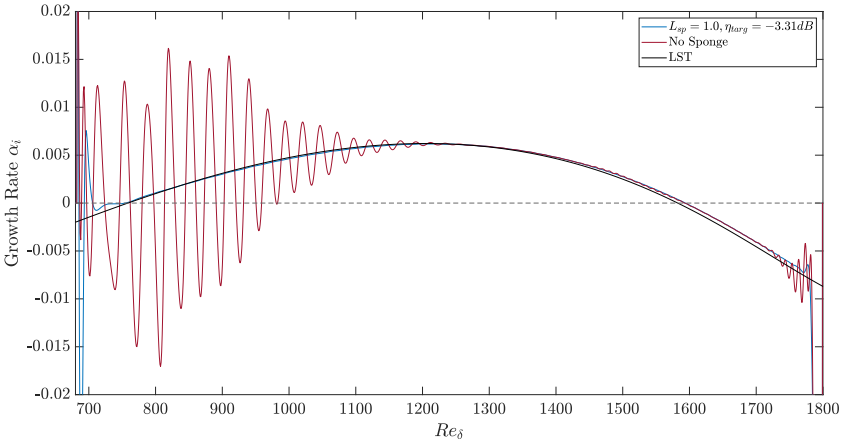


Figure 5.18: Growth rate profile $\alpha_i$ comparison between DNS results with and without sponge at the top of the computational domain and LST for $F = 33.0 \times 10^{-6}$.

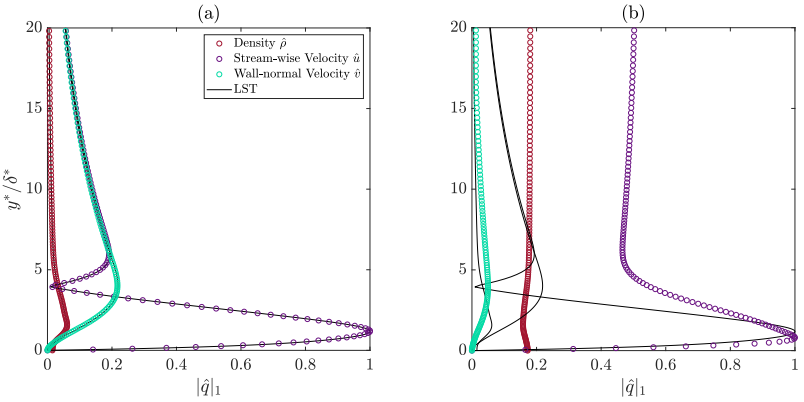


Figure 5.19: Fluctuation amplitude $|\hat{q}|_1$ obtained from DNS (a) with and (b) without a sponge at the top of the computational domain. Profiles are compared with LST eigenvectors at $Re_\delta = 876.37$. Values are normalised by the maximum amplitude of the stream-wise velocity $\hat{u}_{max}$

Based on figure 5.18, not implementing a sponge at the top of the domain has a large influence on the resulting growth rate. Large oscillations appear at the beginning of the

growth zone as well as close to the domain outlet. These oscillations are indications of transient phenomena occurring inside the domain, which interfere with the flow. The interference causes inaccuracies in the calculation of the amplitude of the physical instabilities using Fourier transformation.

Figure 5.19 presents the amplitude of the fluctuations along the $y$ direction within the region that the oscillations are observed on the growth rate diagram. In figure 5.19b the case that does not use a sponge, does not validate the profiles that are predicted by the LST, which confirms that the amplitude of the fluctuations is miscalculated. The Fourier transformation of the for the density in the two cases is provided in figure 5.20.

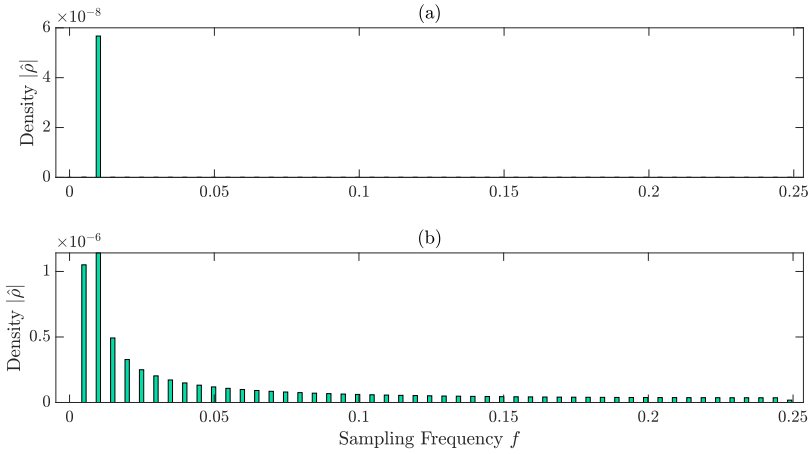


Figure 5.20: Fourier transformation of $\rho'$ for DNS (a) with and (b) without a sponge at the top of the computational domain at $Re_\delta = 876.37$ and $y = 1.19$.

Based on the bar charts of figure 5.20, it is evident that modal decay does not occur in the case of no sponge implementation, due to the occurrence of transient behaviour caused by reflections at the top boundary. This leads to miscalculation of the amplitude of the instabilities as can be seen by comparing the peak values in figures 5.20a and 5.20b.

### 5.7.3. OUTLET SPONGE

Sponge implementation at the outlet of the domain is used to avoid reflections from the boundary. To study the effectiveness of sponges, four cases of varying length $L_{sp}$ and strength $\eta_{targ}$ are considered. Additionally, results are presented for a case without a sponge at the outlet of the domain.

Initially, the growth rate profiles are compared for the considered cases, as shown in figure 5.21. By omitting to use a sponge at the outlet of the domain, oscillations appear close to the boundary, indicating non-physical transient behaviour. It is, also, observed that the inlet of the domain is affected, since oscillations are more evident before the growth zone, compared to the sponged cases. One possible explanation for these observations is that waves reflected from the outlet, travel upstream and interfere with the inlet boundary and sponge.

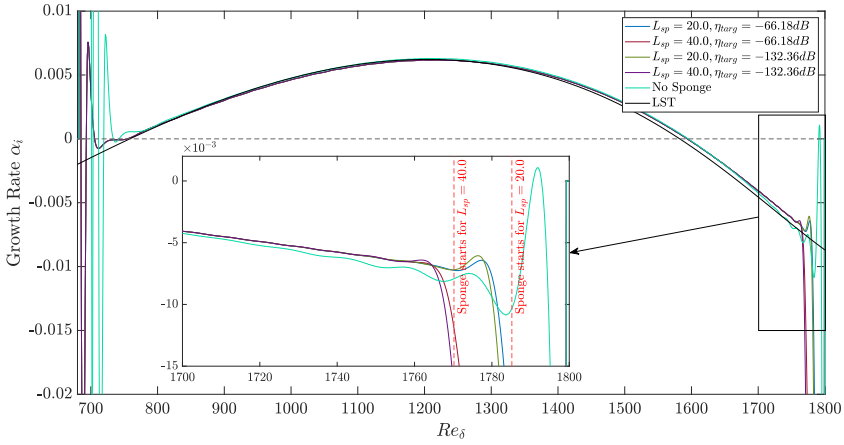


Figure 5.21: Growth rate profile $\alpha_i$ comparison between DNS results with varying sponge properties at the outlet and LST for $F = 33.0 \times 10^{-6}$.

For the comparison of the sponged cases, an illustration of the damping of the pressure fluctuations is provided in figure 5.22. It can be inferred that for this particular flow all the sets of the used parameters can be used to calculate the growth rate of instabilities, according to figure 5.22. Based on the analysis of Ali Mani [18], the optimal set of parameters is, also, a function of the velocity (or $Ma$) and wavelength of the incident waves, hence more simulations should be set up, using different $Ma$ and perturbation frequencies ($F$) to obtain a better understanding of the sponge behaviour.

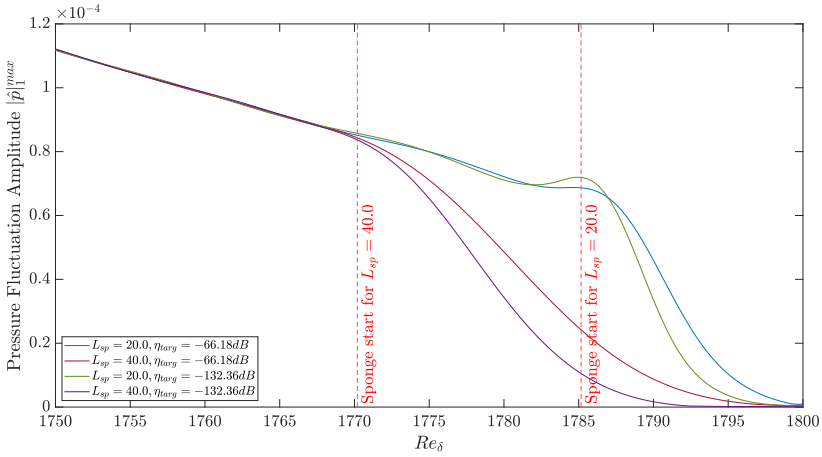


Figure 5.22: Pressure fluctuation amplitude $|\hat{p}|_1^{max}$ for varying sponge properties at the domain outlet.

What can be deduced from the present analysis, is that a small part of the domain

upstream of the sponge is affected by the damping of the sponge in all cases. However, for $L_{sp} = 20.0$ this "extra" space is longer compared to the case of $L_{sp} = 40.0$ and it appears to further increase for stronger sponges. Hence, it is easier to control the size of the domain that is affected by the sponge if $L_{sp}$ is higher, although longer sponges affect a bigger part of the domain. By looking at the slope of the growth rate curves, it is confirmed that stronger sponges damp incident waves more sharply.

In general, setting up a sponge is a trade-off between having a small part of the domain affected by the sponge, while maintaining an efficient damping of the incoming waves by selecting the appropriate sponge strength. Although in this case, a short and weak sponge appears to perform well, it is possible that in other cases this would not be the case. For example in cases where instabilities have higher amplitudes or in fully turbulent simulations, a longer and stronger sponge would be required to ensure that no reflections occur.

## 5.8. CONCLUSIONS

By examining the results presented in this chapter, some conclusions can be reached, which can serve as guidelines for the development of a DNS code.

- Based on figure 5.5, using a mesh not fine enough to resolve the growing instabilities in the stream-wise direction, cases an over-estimation of the growth rate, while oscillatory features might appear on the growth rate curve. To avoid an under-resolving mesh, a good starting point would be to identify the minimum wavelength $\lambda_{w,min}$ that occurs inside the growth zone, using the LST predictions and calculate the number of points that resolve the $\lambda_{w,min}$.
- From figures 5.5 and 5.7 it can be inferred that an increase of stream-wise resolution needs to be accompanied by an increase in the resolution of the wall-normal direction. In general, a finer mesh improves the accuracy of the simulations, however, increasing the mesh resolution leads to a high increase in the computational cost while the increase in accuracy is not significant.
- The results of section 5.5, suggest that domain height has a crucial role in DNS. It is important that the domain is high enough so that the amplitude of growing instabilities is not influenced by the free-stream boundary condition, or the sponge. A good practice would be to check the eigenvectors that are calculated from LST and select a domain height at which the amplitude of the fluctuations is low enough. For the cases that are presented in this study, a domain height of $L_y = 20.0$ is found to be sufficient.
- For the inlet of the domain, both Standard and NRBC can be utilized, according to section 5.6.1, if the purpose of the simulation is to obtain the growth rate curve. However, for boundary layers, a NRBC introduces oscillating patterns at the inlet of the domain which, although minimal, are not desired, hence a Standard condition is preferred in this case. It is possible that the source of oscillations lies in the assumption of inviscid flow during the inviscid characteristic wave analysis. Since a boundary layer flow is highly viscous, it is possible that the inlet is not modelled accurately.

- According to the results of section 5.6.2, a FRBC at the wall introduces some unwanted noise in the simulation. The effects of this noise appear as mild oscillations on the growth rate curve. A Standard boundary condition is preferred. The source of the noise should be further investigated. It would be possible that a FRBC can be noise-free if used with a different spatial discretization scheme (higher order schemes provide better accuracy, while lower order schemes are more stable), or a higher grid resolution along the y-direction.

- The inlet of the domain might not require the implementation of the sponge since no significant difference is observed on the growth rate profile shown in figure 5.16. However an inlet sponge damps waves that are reflected from the outlet or the free-stream of the domain, hence it is advised that the inlet of the domain is accompanied by a sponge to avoid the accumulation noise in the simulation.

- At the top of the computational domain the presence of a sponge is deemed necessary, as observed in the results of section 5.7.2. The free-stream boundary condition, introduces a significant amount of noise in the computational domain, which can be avoided by the implementation of a weak and short sponge at the top of the domain.

- From figure 5.21, it is inferred that the outlet of the domain requires a sponge since waves reflected from the domain outlet, propagate upstream, introducing noise in the computational domain. It is observed, that longer sponges with lower strength, damp the incident waves smoothly, compared to stronger and shorter sponges. However a longer sponge occupies larger space in the computational domain, meaning that there is an optimal combination of sponge strength and length, that yields the desired effect. Factors that should be accounted for, while implementing a sponge, are the velocity, amplitude and wavelength of the incident waves, according to Ali Mani [18].

# 6

# NON-IDEAL GAS SIMULATIONS

In this chapter, results of direct numerical simulations are presented for *non-ideal gas*. The results of the previous chapter are used as guidelines for the selection of parameters that are associated with DNS, in order to obtain proper results and validate the corresponding quantities that are predicted from Linear Stability Theory. As mentioned previously, flows of carbon dioxide at 80 $bar$ are studied to investigate the stability of boundary layer flows in the vicinity of the *Widom Line*.

## 6.1. SELF-SIMILAR SOLUTIONS

To illustrate the effects of a non-ideal gas, on a boundary layer figures 6.1 and 6.2 are provided for an *adiabatic* boundary layer. In the figures, cases with four different $T^*_\infty$ are shown, with $Ec_\infty$ varying from 0.05 to 0.20. The self-similar solutions are validated with results presented in Ren et al. [29], in Appendix C.

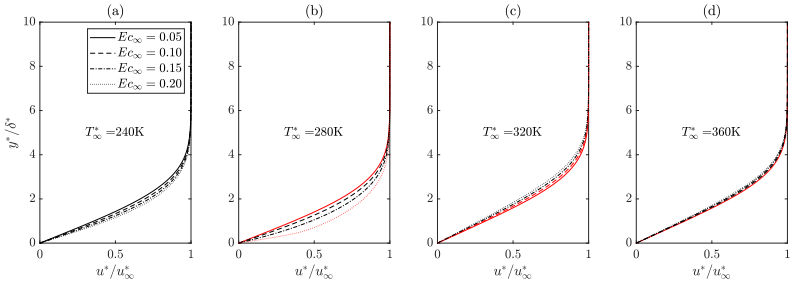


Figure 6.1: Self-similar solutions for stream-wise velocity $u$ as a function of $y^*/\delta^*$, for non-ideal gas flows at (a) $T^*_\infty = 240K$, (b) $T^*_\infty = 280K$, (c) $T^*_\infty = 320K$ and (d) $T^*_\infty = 360K$, for varying $Ec_\infty$. The stability of the cases marked in red is investigated using Direct Numerical Simulations.

It is worth pointing out the suitability of using $Ec_\infty$ over $Ma_\infty$ for measuring compressibility effects in non-ideal flows, as mentioned in Ren et al. [29]. Due to the sharp

drop of the speed of sound near the pseudo-critical point, the value of $Ma_\infty$ might significantly rise with increasing temperature (assuming a constant $u^*_\infty$) since $Ma$ is a function of $u^*$. On the other hand, $Ec$ is a function of $u^{*2}$, hence, an increase in temperature does not dramatically reduce the value of $Ec$, even if the change in $C^*_p$ is high.

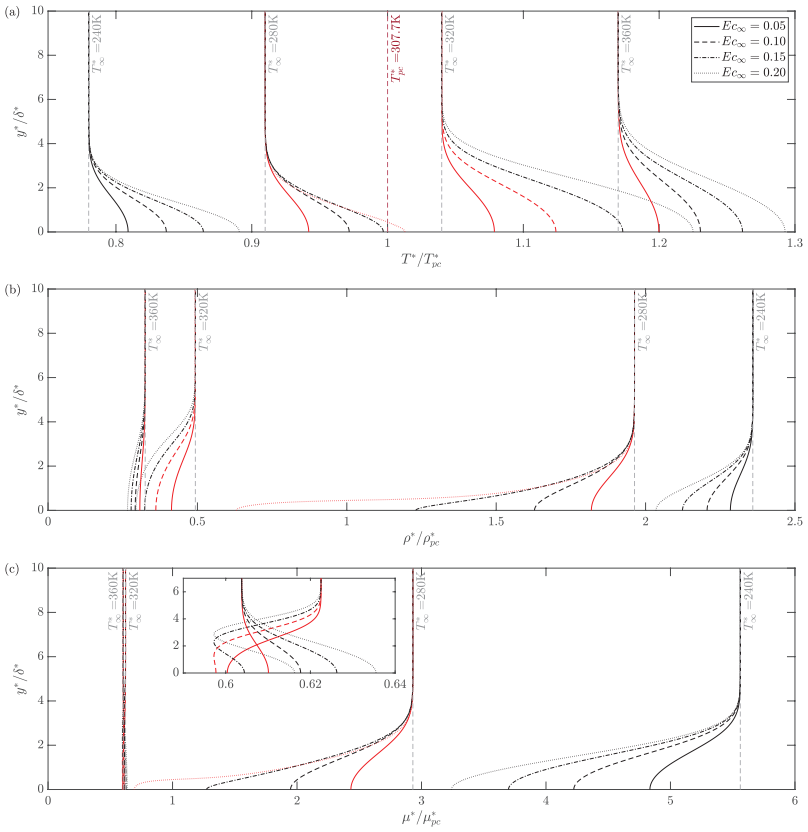


Figure 6.2: Self-similar solutions for flows at $T^*_\infty = 240K$, $T^*_\infty = 280K$, $T^*_\infty = 320K$ and $T^*_\infty = 360K$, for varying $Ec_\infty$. In panels (a) temperature, (b) density and (c) viscosity are provided, normalized by the corresponding values at the pseudo-critical point, as functions of $y^*/\delta^*$. The stability of the cases marked in red is investigated using Direct Numerical Simulations.

Below the pseudo-critical temperature $T^*_{pc} = 307.7\ K$, carbon dioxide exhibits a liquid-like, whereas, above the pseudo-critical point it exhibits a vapor-like behaviour. Based on the self-similar solutions shown in figure 6.1, the boundary layer thickness tends to decrease with increasing $Ec_\infty$ for the cases where $T^*_\infty < T^*_{pc}$, since viscous forces are weaker close to the wall due the drop of viscosity, whereas in the cases where $T^*_\infty > T^*_{pc}$, the opposite is observed, since viscosity variation is not as prominent.

In all cases, an increase of temperature is observed at the wall, due to viscous heating, leading to a drop in density. In the case of $T*_\infty = 280\ K, Ec^*_\infty = 0.20$, the temperature profile crosses the pseudo-critical temperature, hence the flow transits from suprecriti-

cal at the wall, to subcritical in the free-stream and a large density gradient is observed compared to the other cases. This case is referred to as *transcritical* and, also exhibits the most notable decrease in boundary layer thickness, due to non-ideal gas effects, as can be seen in figure 6.1b.

From figure 6.2c, it is observed that the viscosity decreases with increasing temperature for most cases, contrary to the case of an ideal gas. However, in the supercritical regime, the viscosity begins to increase, with temperature, although the variation is comparatively small.

## 6.2. VALIDATION OF LINEAR STABILITY THEORY PREDICTIONS

Stability diagrams are generated using Linear Stability Theory for the cases that are marked in red in figures 6.1 and 6.2. For each of the cases a forcing frequency $F$ is selected and direct numerical simulations are performed, to validate the corresponding growth rate profile. For further validation, the amplitudes of the fluctuations along the wall normal direction, are compared to the eigenvectors that correspond to the unstable modes of the flow. The numerical details for all the simulations that are presented in this section are tabulated in Appendix B.

### 6.2.1. THE SUPERCRITICAL CASES

For the supercritical regime three cases are examined and presented in this section. By using different sets of $T^*_\infty$ and $Ec_\infty$ it is possible to infer the influence of non-ideality and compressibility effects on the stability of the flow.

**Case 1:** $T^*_\infty = 320\ K$ and $Ec_\infty = 0.05$

For this flow $Ma_\infty = 0.97$ and $Pr_\infty = 1.75$. The stability diagram is provided in figure 6.3, along with the growth rate profile that results from the post-processed DNS.

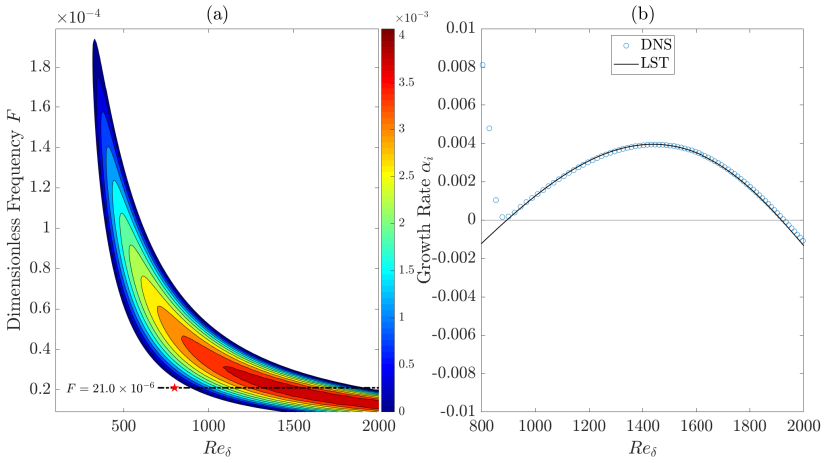


Figure 6.3: (a) Stability diagram for $T_\infty = 320K$ and $Ec_\infty = 0.05$. The span of the computational domain in the stream-wise direction is marked by the horizontal dashed line and the location of the perturbation by (⋆). (b) Growth rate profile using DNS and LST for $F = 21.0 \times 10^{-6}$.

The DNS calculated growth rate of instabilities validates the LST predicted profile sufficiently. It is noted that in this case the outlet of the domain extends to $Re_\delta = 2200.00$, and that the mismatch that is observed in the latter half of the growth rate profile, is less significant compared to the ideal gas case in figure 5.2.

By comparing figure 6.3 to figure 5.2 it is observed that non-ideal gas and compressibility ($Ma_\infty$ is higher in this case) effects tend to stabilize the flow, since the extent of the unstable region appears to be smaller in this case.

To validate the amplitude of the fluctuations along the wall normal direction $Re_\delta = 1399.73$ is selected. The resulting profiles are shown in figure 6.4.

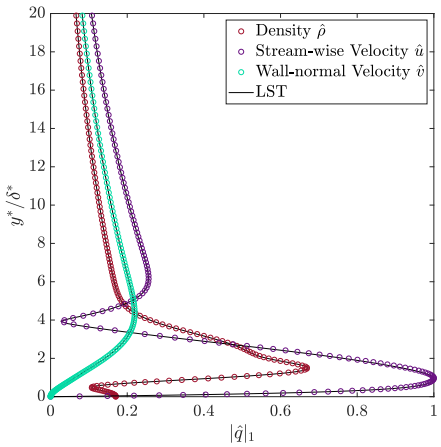


Figure 6.4: Fluctuation amplitude $|\hat{q}|_1$ obtained from DNS. Profiles are compared with LST eigenvectors at $Re_\delta = 1399.73$. Values are normalised by the maximum amplitude of the stream-wise velocity $\hat{u}_{max}$.

The fluctuations of stream-wise velocity dominate in this case, as is observed for an Ideal Gas. However the density fluctuation appears to have a much higher amplitude in this case, due to non-ideal gas and compressibility effects compared to what is shown in figure 5.14a.

**Case 2:** $T^*_\infty = 320\ K$ and $Ec_\infty = 0.10$

For this flow $Ma_\infty = 1.38$, which indicates a super-sonic flow, and $Pr_\infty = 1.75$. The stability diagram and corresponding growth rate validation with DNS are provided in figure 6.5.

For the removal of numerical oscillations on the growth rate curve a filter is applied in this case, using equation (5.2).The unfiltered amplitude of the fluctuations is provided in appendix E, along with the Fourier transformation of wall-normal velocity, to confirm that the results are noise-free.

In this case, the DNS-resulting growth rate under-estimates the LST predictions. The initial perturbation in this case, is implemented very close to the beginning of the growth zone hence the modal decay zone is skipped (zone 3 in figure 5.3) and the initial perturbation is partially inside the growth zone. This causes a strange behaviour in the growth of primary instabilities, as can be seen in figure E.1. Since growth is exponential, even a

small discrepancy in the amplitude, might lead to a significant difference in the growth of instabilities.

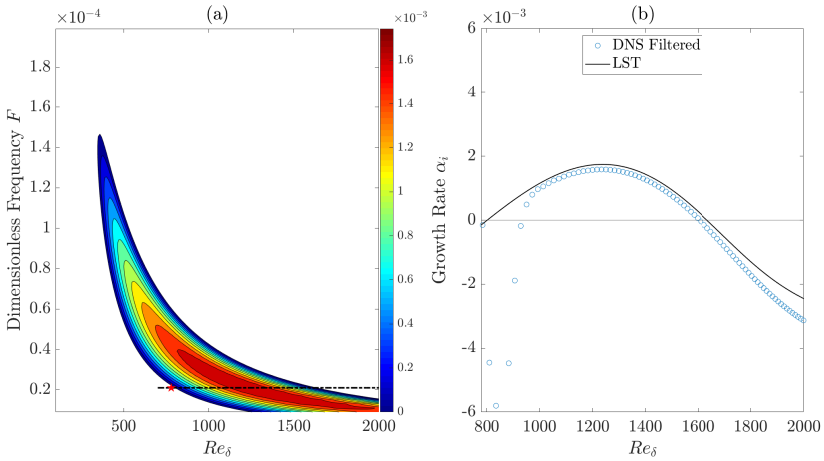


Figure 6.5: (a) Stability diagram for $T_\infty = 320K$ and $Ec_\infty = 0.10$. The span of the computational domain in the stream-wise direction is marked by the horizontal dashed line and the location of the perturbation by (⋆). (b) Growth rate profile using DNS and LST for $F = 21.0 \times 10^{-6}$.

It is evident that compressibility effects stabilize the flow in this case, by comparing figure 6.3a and figure 6.5a. Increasing the Eckert and, consequently, Mach numbers, results to a smaller unstable band in the stability diagram.

To validate the amplitude of the fluctuations along the wall normal direction $Re_\delta = 1399.73$ is selected. The resulting profiles are shown in figure 6.6.

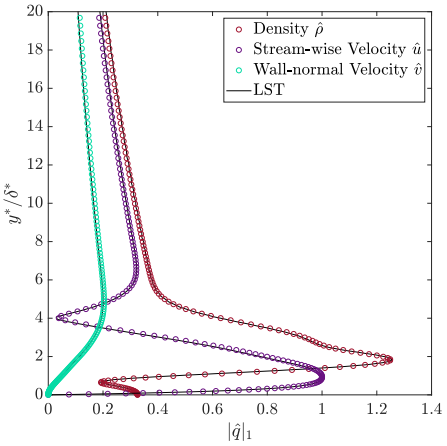


Figure 6.6: Fluctuation amplitude $|\hat{q}|_1$ obtained from DNS. Profiles are compared with LST eigenvectors at $Re_\delta = 1399.73$. Values are normalised by the maximum amplitude of the stream-wise velocity $\hat{u}_{max}$.

The amplitude of the fluctuations in this case, is dominated by the density fluctuation. This can be explained by looking at the linearized continuity equation,

$$(i\alpha u_0 - i\omega)\rho' + i\alpha\rho_0 u' + \frac{d\rho_0}{dy}v' + \rho_0\frac{dv'}{dy} = 0. \tag{6.1}$$

Increasing $Ec_\infty$ or bringing $T^*_\infty$ closer to the pseudo-critical point, the density gradient of the base flow $d\rho_0/dy$ becomes greater, hence the density fluctuation $\rho'$ requires a decrease to balance the equation, resulting to a greater amplitude. This effect is, also, illustrated in Ren et al. [29].

**Case 3:** $T^*_\infty = 360\ K$ and $Ec_\infty = 0.05$

The corresponding dimensionless numbers for this flow are $Ma_\infty = 0.61$ and $Pr_\infty = 1.03$. In figure 6.7, the stability diagram and corresponding growth rate validation with DNS are provided.

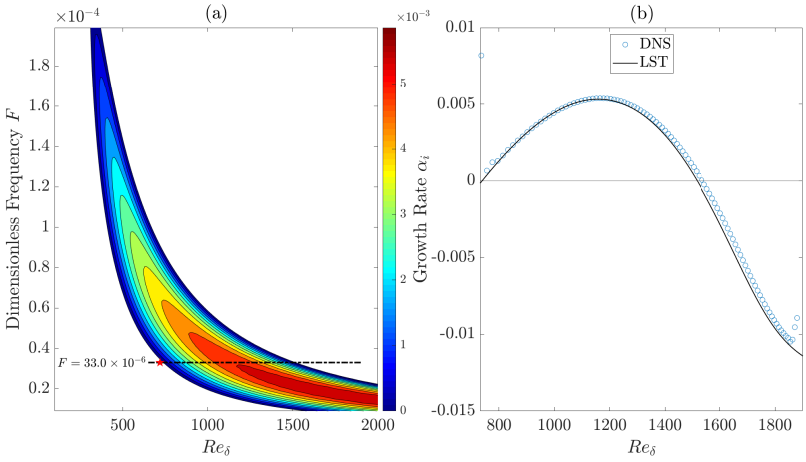


Figure 6.7: (a) Stability diagram for $T_\infty = 360K$ and $Ec_\infty = 0.05$. The span of the computational domain in the stream-wise direction is marked by the horizontal dashed line and the location of the perturbation by (⋆). (b) Growth rate profile using DNS and LST for $F = 33.0 \times 10^{-6}$.

The growth rate profile that is calculated by the DNS sufficiently validates the LST predicted profile, with a slight over-estimation in the latter half of the domain.

In this case, the free stream temperature has increased, hence the non-ideal gas effects are less prominent. This results to the destabilization of the flow, as is observed by comparing figures 6.3a and 6.7a.

To validate the amplitude of the fluctuations along the wall normal direction $Re_\delta = 1200.08$ is selected. The resulting profiles are shown in figure 6.8.

In this case, the fluctuation amplitudes are stream-wise velocity dominated, since compressibility and non-ideal gas effects are less prominent.

The LST-predicted growth rate and amplitude profiles presented in this section, are sufficiently validated by the DNS, confirming the predicted behaviour of the flow.

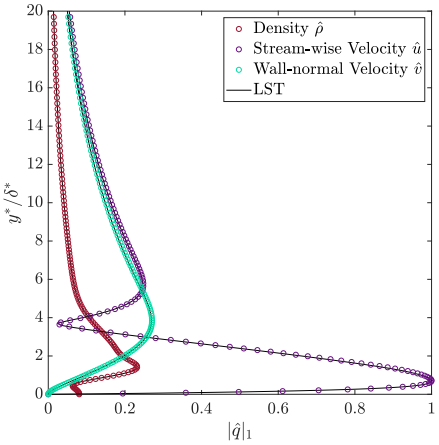


Figure 6.8: Fluctuation amplitude $|\hat{q}|_1$ obtained from DNS. Profiles are compared with LST eigenvectors at $Re_\delta = 1200.08$. Values are normalised by the maximum amplitude of the stream-wise velocity $\hat{u}_{max}$.

### 6.2.2. THE SUBCRITICAL CASE

In this section, direct numerical simulations are performed using the case of $T^*_\infty = 280\ K, Ec_\infty = 0.05$ for the validation of the growth rate profile and the eigenvectors that are provided by Linear Stability Theory.

For this particular flow $Ma_\infty = 0.33$ and $Pr_\infty = 2.13$. In figure 6.9, the stability diagram and the validation of the growth rate profile with DNS are provided.

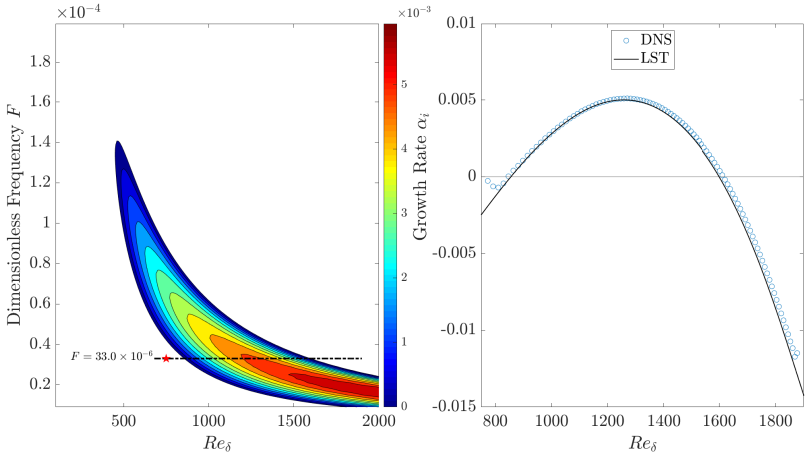


Figure 6.9: (a) Stability diagram for $T_\infty = 280K$ and $Ec_\infty = 0.05$. The span of the computational domain in the stream-wise direction is marked by the horizontal dashed line and the location of the perturbation by ($\star$). (b) Growth rate profile using DNS and LST for $F = 33.0 \times 10^{-6}$.

Again, the DNS-calculated growth rate validates the LST prediction, slightly overestimating the latter half of the profile.

Since the free-stream temperature is close to the pseudo-critical point, non-ideal gas effects stabilize the flow, hence the unstable zone appears smaller on the stability diagram, compared to the supercritical cases. In Ren et al. [29] it is proved that an increase in $Ec_\infty$ tends to stabilize the flow up to some point, before the reaching the transcritical case.

To validate the amplitude of the fluctuations along the wall normal direction $Re_\delta$ = 1300.39 is selected. The resulting profiles are shown in figure 6.10.

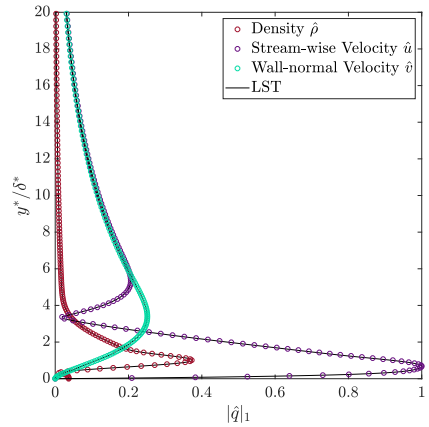


Figure 6.10: Fluctuation amplitude $|\hat{q}|_1$ obtained from DNS. Profiles are compared with LST eigenvectors at $Re_\delta$ = 1300.39. Values are normalised by the maximum amplitude of the stream-wise velocity $\hat{u}_{max}$.

The fluctuation amplitudes are dominated by the stream-wise velocity, which is an indication that compressibility effects are not prominent in this flow, as expected for a flow of low Eckert number.

### 6.2.3. THE TRANSCRITICAL CASE

For the case when $T^*_\infty$ = 280 and $Ec_\infty$ = 0.20, the coexistence of two unstable modes is predicted by the LST. On the stability diagram, Mode $I$ has a similar shape as for the subcritical regime, however Mode $II$ is much larger in size of the unstable zone and growth rate. Further investigation on the appearance of a second unstable mode is carried out by Ren en al. [29].

To validate this behaviour using DNS, a long computational domain is used, so that both modes are captured and a perturbation amplitude $A_1 = 1.0\times10^{-5}$. Stability diagram and validation of the growth rate curve are provided in figure 6.11

The DNS resulting growth rate is filtered during the post-processing to remove numerical oscillations. The unfiltered amplitude of the fluctuations is provided in appendix E, along with the Fourier transformation of wall-normal velocity, to confirm that the results are noise-free.

In general, a good match is obtained between the LST and DNS, however a mismatch

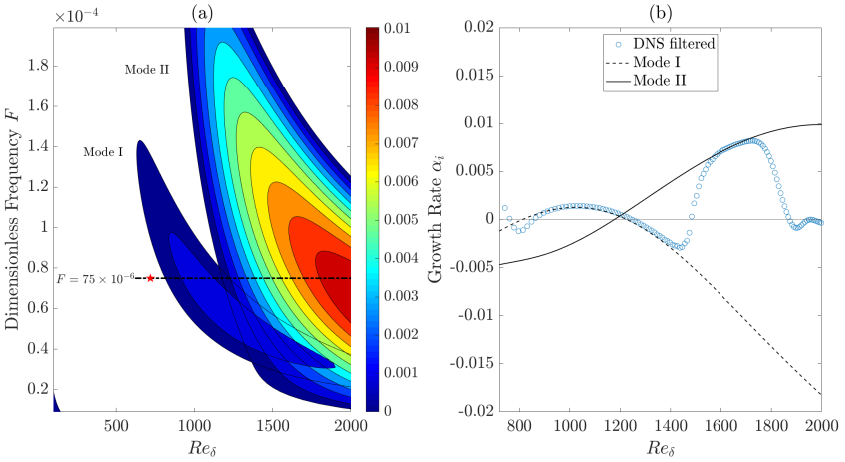


Figure 6.11: (a) Stability diagram for $T_\infty = 280K$ and $Ec_\infty = 0.20$, presenting the two unstable modes. The span of the computational domain in the stream-wise direction is marked by the horizontal dashed line and the location of the perturbation by (⋆). (b) Growth rate profile using DNS and LST for $F = 75.0 \times 10^{-6}$.

occurs after $Re_\delta = 1750.00$, where the growth rate drops to zero, indicating a constant amplitude of the growing instabilities. To further investigate the source of this mismatch, another simulation is set up, with a shorter domain length and a lower perturbation amplitude $A_1 = 1.0^{-8}$. The resulting growth rate curve is presented in figure 6.12.

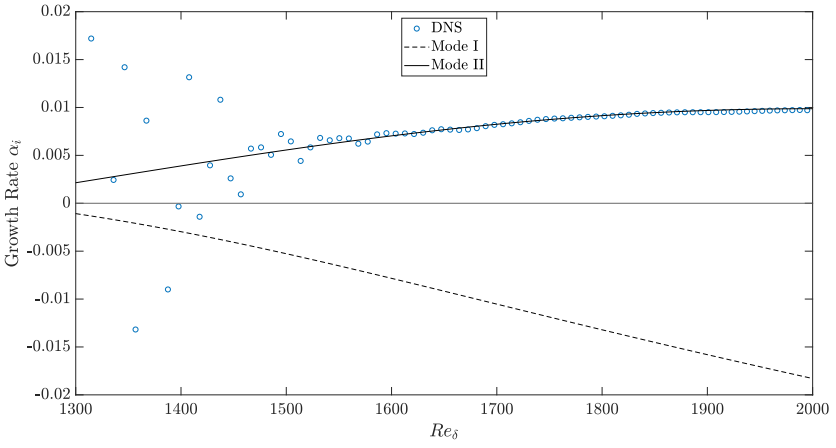


Figure 6.12: Validation of growth rate profile using DNS and LST for $F = 75.0 \times 10^{-6}$ on a shorter domain and lower perturbation amplitude.

It is worth pointing out that the initial perturbation is implemented at $Re_\delta = 1300.00$, hence inside the growth zone of the second mode. This causes oscillations on the growth

rate curve until $Re_\delta = 1700.00$, where the growth of instabilities starts to follow the LST predicted profile. Comparing the results presented in figures 6.11 and 6.12, it can be inferred that the excessive growth of instabilities, causes the amplitude to grow up to a certain point and then no further growth is observed; the flow reaches a new periodic state rather than a secondary instability. Since the amplitude of growing instabilities is directly related to the amplitude of the initial perturbation, this effect does not occur in the second case, where the amplitude of the perturbation is lower, and the instabilities keep growing beyond $Re_\delta = 1750.00$, as predicted by the LST. This indicates the occurrence of *non-linear* effects inside the flow field and prevent the further growth of instabilities, also referred to as non-linear saturation. Since the phenomenon is caused by non-linear mechanisms, it is not predicted by the LST. The Fourier transformation of the density is presented in figure 6.13 for the comparison of modal growth in the two cases.

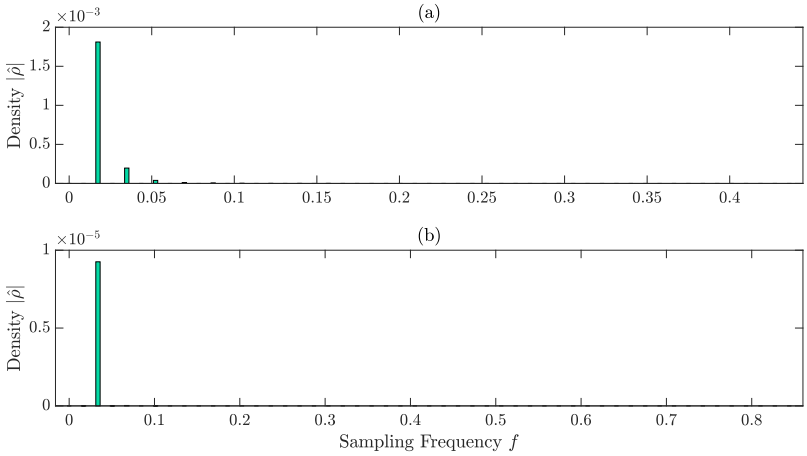


Figure 6.13: Fourier transformation of $\rho'$ for DNS using (a) $A_1 = 1.0 \times 10^{-5}$ and (b) $A_1 = 1.0 \times 10^{-8}$ at $Re_\delta = 1900.00$ and $y = 0.64$.

Based on figure 6.13 it is observed that in the case of $A_1 = 1.0 \times 10^{-5}$, the second, third and fourth harmonics begin to grow, which is not the case for $A_1 = 1.0 \times 10^{-8}$. It is also evident that the amplitude of growing instabilities, is heavily dependent on the amplitude of the perturbation, since the amplitude of the fundamental mode is two orders of magnitude larger in the first case, compared to the second case. Hence, it can be inferred that the excessive growth of primary instabilities, leads to the growth of superharmonic modes which tend to prevent the further growth of instabilities.

To illustrate the development of the instabilities in two modes, a contour plot of the wall-normal velocity profile is provided in figure 6.14. Six physical regions are numbered, each corresponding to a different behaviour. In region 1, the flow exhibits unperturbed behaviour whereas in region 2, the periodic suction and blowing is introduced, hence the receptivity stage of the flow. In region 3, modal decay is exhibited, before reaching modal growth in region 4 for the first mode. The modal switch occurs in region 5 and is succeeded by the excessive growth that occurs in the second mode, in region 6.

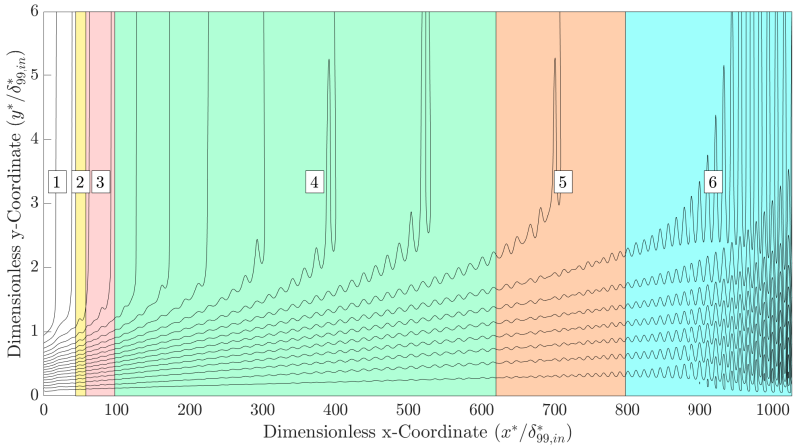


Figure 6.14: Contour lines of wall-normal velocity. The six colored regions correspond to a particular physical behaviour exhibited by the flow.

Eigenvectors are plotted in this case for both modes, in figure 6.15.

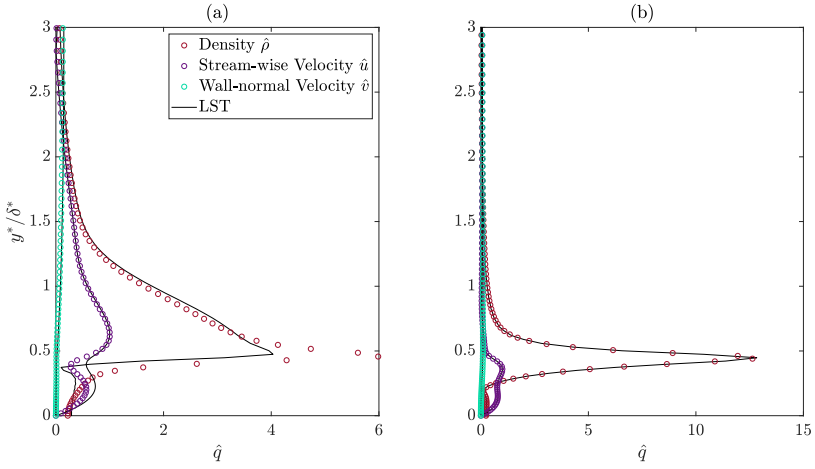


Figure 6.15: Fluctuation amplitudes $|\hat{q}|_1$ obtained from DNS. Profiles are compared with LST eigenvectors at (a) $Re_\delta$ = 1000.52 for Mode $I$ and (b) $Re_\delta$ = 1700.03 for Mode $II$. Values are normalised by the maximum amplitude of the stream-wise velocity $\hat{u}_{max}$.

The eigenvectors of the first mode are not validated sufficiently, possibly because the perturbation amplitude that is used in the DNS is relatively high, causing excessive growth of the instabilities, as is evident by the large deviation of $\hat{\rho}$ in figure 6.15a. The second mode eigenvectors are validated sufficiently by the DNS. In both cases, the density fluctuation dominated due to the large $\partial\rho_0/\partial y$ term in the base flow. From the LST predicted profiles, it is observed that in both modes $\hat{u}$ and $\hat{v}$ are similar, while $\hat{\rho}$ increases

drastically in the second mode, indicating that the existence of Mode $II$, occurs due to large variations of thermodynamic and transport properties [29].

## 6.3. CONCLUSIONS

The results presented in this chapter lead to the conclusions regarding the stability of non-ideal fluids and the validation of Linear Stability Theory predictions with Direct Numerical Simulations. A list of the conclusions is provided below.

- For the cases in which the base flow temperature profile does not cross the pseudo-critical point, stabilization of the flow occurs due to compressibility and non-ideal gas effects. Compressibility effects intensify by incresing $Ec_\infty$, while non-ideal gas effects occur the closer the free-stream temperature $T^*_\infty$ is to the pseudo-critical temperature $T^*_{pc}$. This is observed by comparing the corresponding stability diagrams for each case.

- For the transcritical case, a second mode appears on the stability diagram, which is comparatively more unstable than the first mode. The occurrence of this mode is caused by the large variations in thermodynamic properties, since the flow transits from supercritical at the wall to subcritical in the free-stream. This behaviour is validated with DNS, confirming the existence of a second mode.

- In the DNS of the transcritical case, the phenomenon of *non-linear saturation* occurs inside the second unstable mode. The excessive growth of primary instabilities, leads to the growth of higher harmonics, obstructing the further growth of the fundamental mode. Primary instabilities stop growing in space, thus the growth rate becomes zero. Since this phenomenon is caused by non-linear effects occurring in the flow field, it is not predicted by the LST. By lowering the amplitude of the initial perturbation, non-linear saturation is not exhibited by the flow and the amplitude of instabilities keeps growing in space, as predicted by the LST.

- The compressibility effects on the stability of the flow can be observed by inspecting the fluctuation amplitudes along the wall normal direction. For flows that exhibit large density gradients in the base flow, the amplitude of the density fluctuations are greater in magnitude that the other variables.

- For most cases the DNS validate the LST predictions sufficiently, although a slight mismatch is observed in the latter half of the growth rate curve. One possible explanation would be the non-parallel behaviour of the flow, which is assumed to be negligible in LST. However, non-parallel effects are less prominent far from the leading edge (the magnitude of wall-normal velocity exponentially drops with increasing $x$ 3.5b), which does not justify the mismatch at higher $Re_\delta$. In figures 6.3b and 6.12 it is observed that the mismatch is less evident, compared to the other cases. In both these cases, the outlet of the computational domain is located at $Re_\delta > 2000.00$ which indicates that the outlet boundary condition and sponge, affect the growth of instabilities, and can possibly cause a mismatch between the DNS and LST results.

- For cases in which the growth rate of instabilities is relatively low ($T^*_\infty = 320\ K, Ec_\infty = 0.10$ and first mode of $T^*_\infty = 280\ K, Ec_\infty = 0.20$), the amplitude of instabilities exhibits an oscillatory behaviour, which is filtered out. The origin of these oscillations is not entirely clear, based on the results of the present study, however several speculations can be made. One possibility is that the amplitude of the initial perturbation is too high, which could mean that the triggering of instabilities occurs at the limit before the non-linear regime. Another possibility is that the perturbation is implemented, very close to the growth zone. By placing the perturbation inside the modal decay zone, upstream of the growth zone, the triggered instabilities are physically damped before they begin to grow. Finally, it is possible that the present DNS do not capture lower amplitudes sufficiently, hence the computational parameters require further optimization. Parameters like the extent and strength of the sponges, the height and resolution of the domain, the thermodynamic table resolution or the numerical schemes that are used, could be adjusted.

# 7

# DISCUSSION

In this chapter, the methodology and results are summarized and suggestions for further research are provided.

## 7.1. SUMMARY

The main objective of this study is the development of a FORTRAN code that can be used for direct numerical simulations to study the stability and transition of non-ideal boundary layer flows. Boundary conditions, numerical sponges and thermodynamic table interpolation tools have been implemented on a code that was previously used to simulate Poiseuille channel flows for ideal gas. The code is tested on an ideal gas case, in order to study the effect of various sets of parameters and boundary conditions for the simulations of linear stability. To check the accuracy and reliability of the used methods, the results from the DNS are compared to the quantities predicted by Linear Stability Theory. After selecting the proper parameters for the DNS code, the stability of Carbon Dioxide boundary layers at 80 *bar* is investigated.

For the initialization of the DNS, the laminar base flow needs to be provided. To obtain the base flow, a MATLAB tool is developed to calculate the self-similar boundary layer solution and then interpolate on a two-dimensional mesh.

Boundary conditions are implemented using an inviscid characteristic wave analysis and some alternatives are provided for the inlet and the wall. Numerical sponges are employed at the inlet, outlet and free-stream boundaries to avoid reflections. A periodic suction and blowing is implemented to trigger the Tollmien-Schlichting waves that will initiate the development of instabilities. Finally, a Lagrange interpolation method is utilized for the calculation of thermodynamic properties using tables obtained from REFPROP library.

For the post-processing of the DNS results, a MATLAB script is used to obtain the Fourier transformation of the resulting flow fields, in order to calculate the growth rate of instabilities. In some cases, filtering is applied to remove numerical oscillations that might occur during the simulations.

The stability diagrams and eigenvectors are obtained by a MATLAB tool that has been developed by Jie Ren, and are utilized for the validation of the post-processed results obtained from the DNS.

From the DNS of the ideal gas boundary layer, it is inferred that the stream-wise resolution needs to be high enough to resolve the growing instabilities, while keeping in mind that an increase in stream-wise resolution needs to be accompanied by an increase in the wall-normal resolution. Also, the height of the domain plays an important role in the accurate calculation of the amplitude of growing instabilities. Inviscid characteristic boundary condtitions may be applied at the inlet, though, a standard implementation yields less oscillations. For the wall boundary condition it is preferred to use a standard implementation, since the inviscid characteristic option introduces mild numerical noise. It is, further, observed that the utilization of numerical sponges is necessary at the outlet and top of the computational domain, whereas optional for the inlet.

For the case of non-ideal gas, the stability of the flow is influenced by compressibility and non-ideal gas effects. Flows for which the temperature profile does not cross the pseudo-critical temperature, are stabilized when non-ideal gas ($T^*_\infty$ is close to $T^*_{pc}$) or compressibility (higher $Ec_\infty$) effects are present. In cases where compressibility effects are more intense, the density fluctuation amplitude becomes larger that the stream-wise velocity amplitude, due to the high density gradients and the balancing mechanism of the linearized continuity equation. In the case that the temperature profile crosses the pseudo-critical temperature (transcritical case), the flow exhibits destabilization through the appearance of a second unstable mode on the stability diagram. This behaviour is validated by the DNS, however for very large amplitudes of the growing instabilities, a behaviour that is not predicted by the LST is exhibited, since the growth of instabilities becomes zero, leading the flow to a new periodic state. This phenomenon does not occur for a lower amplitude of the initial perturbation.

## 7.2. PROPOSAL FOR FURTHER RESEARCH

The findings of this study, lead to new questions about the development of a DNS code and the stability of non-ideal boundary layer flows. Some suggestions for topics that require further investigation are listed in this section.

- This entire study is conducted for adiabatic wall boundary layers. A similar study can be conducted to investigate the stability of isothermal wall boundary layers. It would, also, be possible to study more complicated geometries and investigate the effects of curvature or surface roughness on the stability of flows.

- The investigation of Chapter 5, should be repeated using different flow conditions. It is already evident from the results presented in Chapter 6, that following the guidelines presented in this study is not sufficient for some cases, since the post processed result required filtering to validate the LST predictions. The possibility that some of the presented parameters are dependent on the flow conditions is high, and should be further investigated so that guidelines for the development of a DNS code that is used to study the stability and transition of flows can be drawn.

- The effect of oblique perturbations can be further investigated with DNS, by setting up three-dimensional simulations and using small perturbation amplitudes.
- The saturation in the growth rate of instabilities in the transcritical case, should be further investigated since the cause of this phenomenon is not entirely clear, based on the results of the present study. The mechanism that leads to constant amplitude of the growing instabilities should be identified, since it might obstruct the development of turbulence in larger simulations.
- To unveil the transitional behaviour of non-ideal boundary layers, simulations in three dimensions should be set up, using span-wise disturbances and higher perturbation amplitudes to trigger the instabilities, leading to a controlled transition to turbulence.

# A

# Domain Height Influence on DNS of Non-Ideal Gas

As supplementary material to the study conducted in section 5.5, figure A.1 is provided to illustrate the effect of varying the domain height for the case of supercritical Carbon Dioxide at $T^*_\infty = 320\ K$ and $Ec_\infty = 0.05$. Four cases are considered using $L_y = 8.0$, $L_y = 10.0$, $L_y = 14.0$ and $L_y = 20.0$.

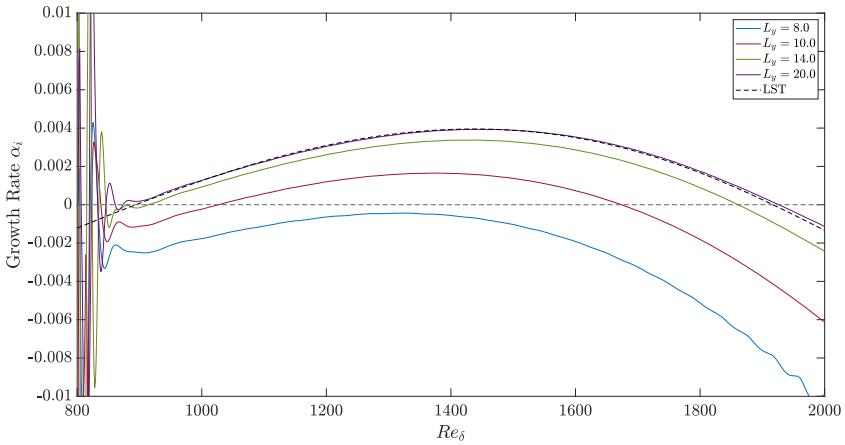


Figure A.1: Growth rate profile $\alpha_i$ comparison between DNS results for domain heights $L_y = 8.0$, $L_y = 10.0$, $L_y = 14.0$, $L_y = 20.0$ and LST for supercritical Carbon Dioxide at $T^*_\infty = 320\ K$, $Ec_\infty = 0.05$, and $F = 21.0 \times 10^{-6}$.

In this case the effects of a lower domain height are more severe than for the ideal gas case, since for height as low as $L_y = 8.0$, the growth rate has only negative values even in the range that the LST predicts positive values. The importance of using a high height domain is highlighted in this case.

# B

# COMPUTATIONAL PARAMETERS FOR DNS OF NON-IDEAL GAS

The values of the computational and flow parameters for the simulations that are presented in Chapter 5 are tabulated and provided in this appendix.

Table B.1: Values Used for the Direct Numerical Simulation of the $T^*_\infty = 320\ K, Ec_\infty = 0.05$ case.

| **Flow Parameters** | | | | | |
|---|---|---|---|---|---|
| $T^*_\infty$ | | 320.0 $K$ | $Ec_\infty$ | | 0.05 |
| $Ma_\infty$ | | 0.97 | $Pr_\infty$ | | 1.75 |
| $Re_{\delta,in}$ | | 700.00 | $Re_{\delta,out}$ | | 2200.00 |
| **Computational Grid Values** | | | **Time Stepping** | | |
| $L_x$ | | 1228.89 | $K_t$ | | 20000 |
| $L_y$ | | 20.0 | $n_{steps}$ | | 2000000 |
| $n_x$ | | 2112 | **Perturbation Related Parameters** | | |
| $n_y$ | | 200 | $F$ | | $21 \times 10^{-6}$ |
| $S_f$ | | 5.0 | $A_1$ | | $1.0 \times 10^{-5}$ |
| **Computational Sponge Parameters** | | | $Re_\delta(x_m)$ | | 800.0 |
| Inlet | $L_{sp}$ | 20.0 | $x_1 - x_2$ | | 15.13 |
| | $\sigma_{max}$ | 0.5 | **Boundary Conditions** | | |
| Outlet | $L_{sp}$ | 20.0 | Inlet | | Standard, Adiabatic |
| | $\sigma_{max}$ | 0.5 | Wall | | Standard, Adiabatic |
| Free-Stream | $L_{sp}$ | 1.0 | Outlet | | NRBC, $\sigma_{bc} = 0.0$ |
| | $\sigma_{max}$ | 0.5 | Free-Stream | | NRBC, $\sigma_{bc} = 0.25$ |
| **Thermodynamic Table Parameters** | | | | | |
| $\rho^*_{min}$ | 180.0 $kg/m^3$ | $E^*_{min}$ | $3.8 \times 10^5\ J/kg$ | $T^*_{min}$ | 300.0 $K$ |
| $\rho^*_{max}$ | 300.0 $kg/m^3$ | $E^*_{max}$ | $4.2 \times 10^5\ J/kg$ | $T^*_{max}$ | 340.0 $K$ |
| $n_\rho$ | 200 | $n_E$ | 200 | $n_T$ | 200 |

Table B.2: Values Used for the Direct Numerical Simulation of the $T^*_\infty = 320\ K, Ec_\infty = 0.10$ case.

| **Flow Parameters** | | | | | |
|---|---|---|---|---|---|
| $T^*_\infty$ | | 320.0 $K$ | $Ec_\infty$ | | 0.10 |
| $Ma_\infty$ | | 1.38 | $Pr_\infty$ | | 1.75 |
| $Re_{\delta,in}$ | | 700.00 | $Re_{\delta,out}$ | | 2200.00 |
| **Computational Grid Values** | | | **Time Stepping** | | |
| $L_x$ | | 1191.37 | $K_t$ | | 20000 |
| $L_y$ | | 20.0 | $n_{steps}$ | | 2000000 |
| $n_x$ | | 2112 | **Perturbation Related Parameters** | | |
| $n_y$ | | 200 | $F$ | | $21 \times 10^{-6}$ |
| $S_f$ | | 5.0 | $A_1$ | | $1.0 \times 10^{-5}$ |
| **Computational Sponge Parameters** | | | $Re_\delta(x_m)$ | | 780.0 |
| Inlet | $L_{sp}$ | 20.0 | $x_1 - x_2$ | | 14.67 |
| | $\sigma_{max}$ | 0.5 | **Boundary Conditions** | | |
| Outlet | $L_{sp}$ | 20.0 | Inlet | | Standard, Adiabatic |
| | $\sigma_{max}$ | 0.5 | Wall | | Standard, Adiabatic |
| Free-Stream | $L_{sp}$ | 1.0 | Outlet | | NRBC, $\sigma_{bc} = 0.0$ |
| | $\sigma_{max}$ | 0.5 | Free-Stream | | NRBC, $\sigma_{bc} = 0.25$ |
| **Thermodynamic Table Parameters** | | | | | |
| $\rho^*_{min}$ | 150.0 $kg/m^3$ | $E^*_{min}$ | $3.8 \times 10^5\ J/kg$ | $T^*_{min}$ | 300.0 $K$ |
| $\rho^*_{max}$ | 300.0 $kg/m^3$ | $E^*_{max}$ | $4.4 \times 10^5\ J/kg$ | $T^*_{max}$ | 360.0 $K$ |
| $n_\rho$ | 200 | $n_E$ | 200 | $n_T$ | 200 |

Table B.3: Values Used for the Direct Numerical Simulation of the $T^*_\infty = 360.0\ K, Ec_\infty = 0.05$ case.

| **Flow Parameters** | | | | | |
|---|---|---|---|---|---|
| $T^*_\infty$ | | 360.0 $K$ | $Ec_\infty$ | | 0.05 |
| $Ma_\infty$ | | 0.61 | $Pr_\infty$ | | 1.03 |
| $Re_{\delta,in}$ | | 650.00 | $Re_{\delta,out}$ | | 1900.00 |
| **Computational Grid Values** | | | **Time Stepping** | | |
| $L_x$ | | 982.56 | $K_t$ | | 20000 |
| $L_y$ | | 20.0 | $n_{steps}$ | | 2000000 |
| $n_x$ | | 2112 | **Perturbation Related Parameters** | | |
| $n_y$ | | 200 | $F$ | | $33 \times 10^{-6}$ |
| $S_f$ | | 4.0 | $A_1$ | | $1.0 \times 10^{-5}$ |
| **Computational Sponge Parameters** | | | $Re_\delta(x_m)$ | | 720.0 |
| Inlet | $L_{sp}$ | 20.0 | $x_1 - x_2$ | | 12.10 |
| | $\sigma_{max}$ | 0.5 | **Boundary Conditions** | | |
| Outlet | $L_{sp}$ | 20.0 | Inlet | | Standard, Adiabatic |
| | $\sigma_{max}$ | 0.5 | Wall | | Standard, Adiabatic |
| Free-Stream | $L_{sp}$ | 1.0 | Outlet | | NRBC, $\sigma_{bc} = 0.0$ |
| | $\sigma_{max}$ | 0.5 | Free-Stream | | NRBC, $\sigma_{bc} = 0.25$ |
| **Thermodynamic Table Parameters** | | | | | |
| $\rho^*_{min}$ | 130.0 $kg/m^3$ | $E^*_{min}$ | $4.3 \times 10^5\ J/kg$ | $T^*_{min}$ | 340.0 $K$ |
| $\rho^*_{max}$ | 170.0 $kg/m^3$ | $E^*_{max}$ | $4.7 \times 10^5\ J/kg$ | $T^*_{max}$ | 400.0 $K$ |
| $n_\rho$ | 200 | $n_E$ | 200 | $n_T$ | 200 |

Table B.4: Values Used for the Direct Numerical Simulation of the $T^*_\infty = 280\ K, Ec_\infty = 0.05$ case.

| **Flow Parameters** | | | | | |
|---|---|---|---|---|---|
| $T^*_\infty$ | | 280.0 $K$ | $Ec_\infty$ | | 0.05 |
| $Ma_\infty$ | | 0.33 | $Pr_\infty$ | | 2.13 |
| $Re_{\delta,in}$ | | 680.00 | $Re_{\delta,out}$ | | 1900.00 |
| **Computational Grid Values** | | | **Time Stepping** | | |
| $L_x$ | | 966.58 | $K_t$ | | 10000 |
| $L_y$ | | 20.0 | $n_{steps}$ | | 1000000 |
| $n_x$ | | 2112 | **Perturbation Related Parameters** | | |
| $n_y$ | | 200 | $F$ | | $33 \times 10^{-6}$ |
| $S_f$ | | 4.0 | $A_1$ | | $1.0 \times 10^{-5}$ |
| **Computational Sponge Parameters** | | | $Re_\delta(x_m)$ | | 750.0 |
| Inlet | $L_{sp}$ | 20.0 | $x_1 - x_2$ | | 11.90 |
| | $\sigma_{max}$ | 0.5 | **Boundary Conditions** | | |
| Outlet | $L_{sp}$ | 20.0 | Inlet | | Standard, Adiabatic |
| | $\sigma_{max}$ | 0.5 | Wall | | Standard, Adiabatic |
| Free-Stream | $L_{sp}$ | 1.0 | Outlet | | NRBC, $\sigma_{bc} = 0.0$ |
| | $\sigma_{max}$ | 0.5 | Free-Stream | | NRBC, $\sigma_{bc} = 0.25$ |
| **Thermodynamic Table Parameters** | | | | | |
| $\rho^*_{min}$ | 840.0 $kg/m^3$ | $E^*_{min}$ | $2.0 \times 10^5\ J/kg$ | $T^*_{min}$ | 260.0 $K$ |
| $\rho^*_{max}$ | 950.0 $kg/m^3$ | $E^*_{max}$ | $2.3 \times 10^5\ J/kg$ | $T^*_{max}$ | 300.0 $K$ |
| $n_\rho$ | 200 | $n_E$ | 200 | $n_T$ | 200 |

Table B.5: Values Used for the Direct Numerical Simulation of the $T^*_\infty = 280\ K, Ec_\infty = 0.20$ case.

| **Flow Parameters** | | | | | |
|---|---|---|---|---|---|
| $T^*_\infty$ | | 280.0 $K$ | $Ec_\infty$ | | 0.20 |
| $Ma_\infty$ | | 0.66 | $Pr_\infty$ | | 2.13 |
| $Re_{\delta,in}$ | | 620.00 | $Re_{\delta,out}$ | | 2100.00 |
| **Computational Grid Values** | | | **Time Stepping** | | |
| $L_x$ | | 1542.75 | $K_t$ | | 10000 |
| $L_y$ | | 20.0 | $n_{steps}$ | | 2000000 |
| $n_x$ | | 2880 | **Perturbation Related Parameters** | | |
| $n_y$ | | 200 | $F$ | | $75 \times 10^{-6}$ |
| $S_f$ | | 5.0 | $A_1$ | | $1.0 \times 10^{-5}$ |
| **Computational Sponge Parameters** | | | $Re_\delta(x_m)$ | | 720.0 |
| Inlet | $L_{sp}$ | 20.0 | $x_1 - x_2$ | | 13.93 |
| | $\sigma_{max}$ | 0.5 | **Boundary Conditions** | | |
| Outlet | $L_{sp}$ | 100.0 | Inlet | | Standard, Adiabatic |
| | $\sigma_{max}$ | 1.0 | Wall | | Standard, Adiabatic |
| Free-Stream | $L_{sp}$ | 2.0 | Outlet | | NRBC, $\sigma_{bc} = 0.0$ |
| | $\sigma_{max}$ | 1.0 | Free-Stream | | NRBC, $\sigma_{bc} = 0.25$ |
| **Thermodynamic Table Parameters** | | | | | |
| $\rho^*_{min}$ | 250.0 $kg/m^3$ | $E^*_{min}$ | $1.8 \times 10^5\ J/kg$ | $T^*_{min}$ | 260.0 $K$ |
| $\rho^*_{max}$ | 1000.0 $kg/m^3$ | $E^*_{max}$ | $4.0 \times 10^5\ J/kg$ | $T^*_{max}$ | 340.0 $K$ |
| $n_\rho$ | 800 | $n_E$ | 800 | $n_T$ | 800 |

Table B.6: Values Used for the Direct Numerical Simulation of the short $T^*_\infty = 280\ K, Ec_\infty = 0.20$ case with lower perturbation amplitude.

| **Flow Parameters** | | | | | |
|---|---|---|---|---|---|
| $T^*_\infty$ | | 280.0 $K$ | $Ec_\infty$ | | 0.20 |
| $Ma_\infty$ | | 0.66 | $Pr_\infty$ | | 2.13 |
| $Re_{\delta,in}$ | | 1200.00 | $Re_{\delta,out}$ | | 2100.00 |
| **Computational Grid Values** | | | **Time Stepping** | | |
| $L_x$ | | 588.07 | $K_t$ | | 10000 |
| $L_y$ | | 20.0 | $n_{steps}$ | | 2000000 |
| $n_x$ | | 2112 | **Perturbation Related Parameters** | | |
| $n_y$ | | 200 | $F$ | | $75 \times 10^{-6}$ |
| $S_f$ | | 5.0 | $A_1$ | | $1.0 \times 10^{-8}$ |
| **Computational Sponge Parameters** | | | $Re_\delta(x_m)$ | | 1300.0 |
| Inlet | $L_{sp}$ | 20.0 | $x_1 - x_2$ | | 13.93 |
| | $\sigma_{max}$ | 0.5 | **Boundary Conditions** | | |
| Outlet | $L_{sp}$ | 100.0 | Inlet | | Standard, Adiabatic |
| | $\sigma_{max}$ | 1.0 | Wall | | Standard, Adiabatic |
| Free-Stream | $L_{sp}$ | 2.0 | Outlet | | NRBC, $\sigma_{bc} = 0.0$ |
| | $\sigma_{max}$ | 1.0 | Free-Stream | | NRBC, $\sigma_{bc} = 0.25$ |
| **Thermodynamic Table Parameters** | | | | | |
| $\rho^*_{min}$ | 250.0 $kg/m^3$ | $E^*_{min}$ | $1.8 \times 10^5\ J/kg$ | $T^*_{min}$ | 260.0 $K$ |
| $\rho^*_{max}$ | 1000.0 $kg/m^3$ | $E^*_{max}$ | $4.0 \times 10^5\ J/kg$ | $T^*_{max}$ | 340.0 $K$ |
| $n_\rho$ | 800 | $n_E$ | 800 | $n_T$ | 800 |

# C

# VALIDATION OF NON-IDEAL GAS BASE FLOW WITH LITERATURE

The base flow profiles presented in section 6.1, are validated with the profiles presented in Ren et al. [29]. Some of the cases that are simulated in Chapter 5 are presented in figure C.1, validated with the reference profiles.

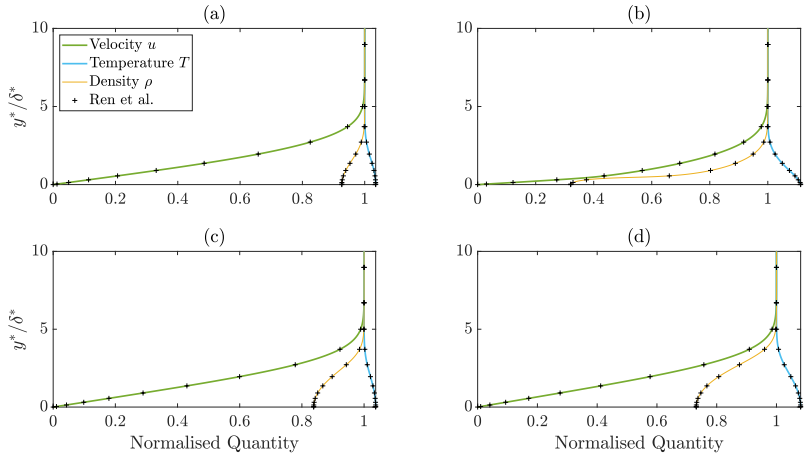


Figure C.1: Validation of base flow profiles for Carbon Dioxide at 80 bar for (a) $T^*_\infty = 280\ K$, $Ec_\infty = 0.05$, (b) $T^*_\infty = 280\ K$, $Ec_\infty = 0.20$, (c) $T^*_\infty = 320\ K$, $Ec_\infty = 0.05$ and (d) $T^*_\infty = 320\ K$, $Ec_\infty = 0.20$.

# D

# Influence of Table Resolution on the DNS of the Transcritical Case

The Direct Numerical Simulations of the transcritical case, have been performed using two different values for the resolution of the thermodynamic tables. To compare the two cases, figure D.1 is provided, presenting the growth rate profile. In the tables for these cases density ranges from 250.0 $kg/m^3$ to 1000.0 $kg/m^3$ and internal energy ranges from $1.8 \times 10^5$ $J/kg$ to $4.0 \times 10^5$ $J/kg$.

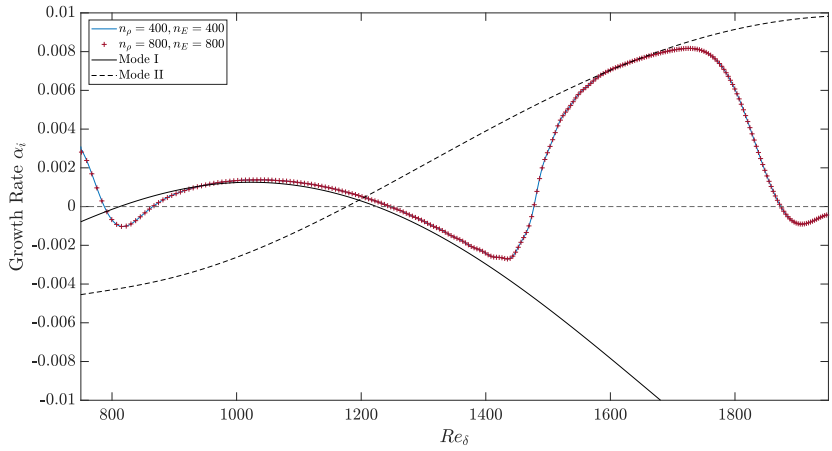


Figure D.1: Growth rate profile $\alpha_i$ comparison between DNS results for table resolution of 400 × 400 and 800 × 800, and LST for $T^*_\infty = 280, Ec_\infty = 0.20$.

According to the results of figure D.1, even the thermodynamic table with low reso-

lution is suitable for the simulation of the transcritical case. The growth rate calculated for the two cases is identical, hence tables do not require further refinement to produce accurate results.

# E

# Unfiltered Fluctuation Amplitudes for DNS

In chapter 6 the amplitude of fluctuation profiles that is calculated from the DNS, is filtered using equation (5.2) for the cases with $T^*_\infty = 320\ K, Ec_\infty = 0.10$ and $T^*_\infty = 280\ K, Ec_\infty = 0.20$. In this appendix, the unfiltered profiles are presented, along with the Fourier transformations of each case, to examine the possibility of transient phenomena occurring inside the computational domain.

- **Carbon dioxide at $T^*_\infty = 320\ K$ and $Ec_\infty = 0.10$**

  In figure E.1 the unfiltered fluctuation amplitude profiles of wall-normal velocity are presented, along with the resulting filtered result.

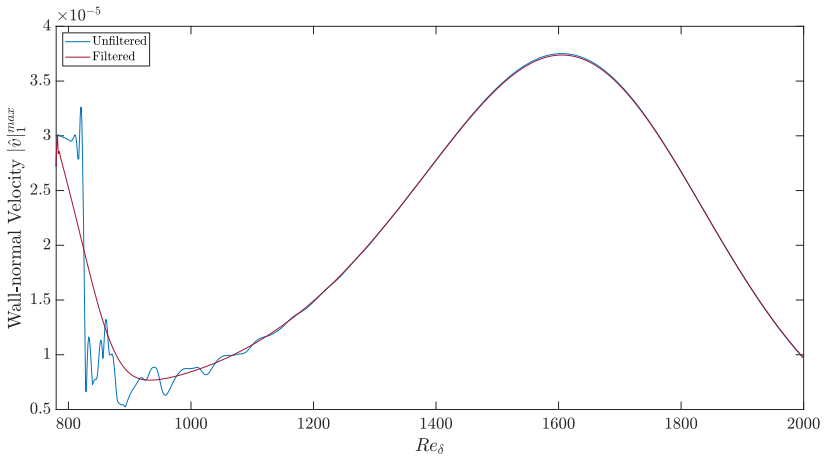


Figure E.1: Amplitude of wall-normal velocity fluctuations $|\hat{v}|_1^{max}$ before and after filtering for supercritical Carbon Dioxide at $T^*_\infty = 320\ K$, $Ec_\infty = 0.10$, and $F = 21.0 \times 10^{-6}$.

The fluctuation amplitude exhibits a strange behaviour from $Re_\delta = 780.00$ until $Re_\delta = 1250.00$. To investigate whether this behaviour is exhibited due to numerical noise, the Fourier-transformation of the wall-normal velocity is presented in figure E.2 for $Re_\delta = 900.00$ and $y = 0.64$.

Based on figure E.2, it can be inferred that the strange behaviour is not exhibited due to unwanted noise inside the computational domain, since only the fundamental mode is present.

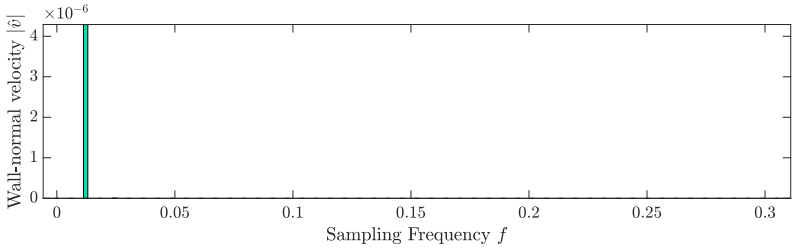


Figure E.2: Fourier transformation of $v'$ for DNS at $Re_\delta = 900.00$ and $y = 0.64$.

- **Carbon dioxide at $T^*_\infty = 280\ K$ and $Ec_\infty = 0.20$**

  The unfiltered amplitude fluctuation profile of the wall-normal velocity is presented in figure E.3.

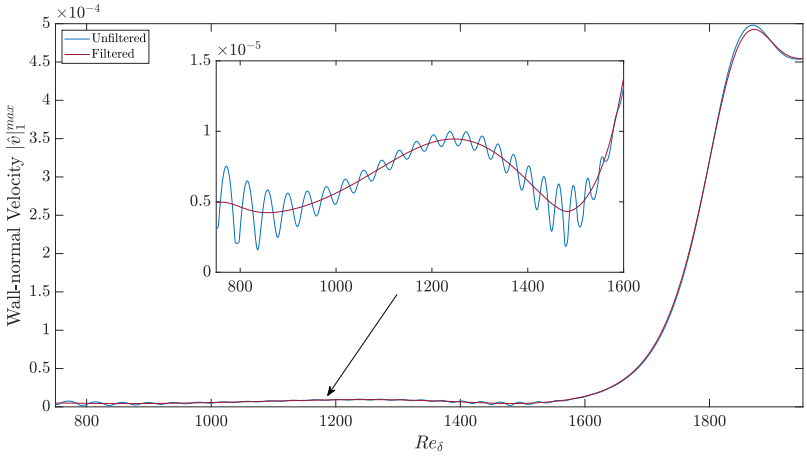


Figure E.3: Amplitude of wall-normal velocity fluctuations $|\hat{v}|_1^{max}$ before and after filtering for supercritical Carbon Dioxide at $T^*_\infty = 280\ K$, $Ec_\infty = 0.20$, and $F = 75.0 \times 10^{-6}$.

Oscillatory behaviour is exhibited inside the growth zone of the first mode, where the amplitude of the fluctuations is small, compared to the amplitude in the second mode. To identify whether the oscillatory behaviour results from noise, the

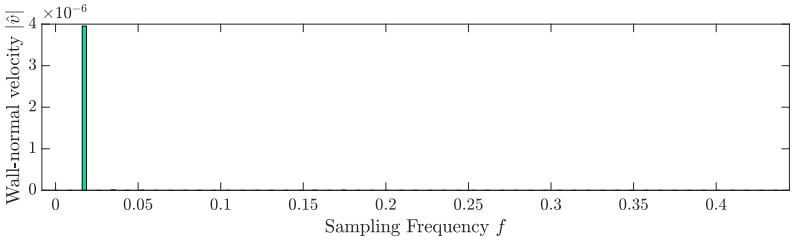


Figure E.4: Fourier transformation of $v'$ for DNS at $Re_\delta = 1000.52$ and $y = 0.64$.

Fourier transformation of the wall-normal velocity is provided in figure E.4 for $Re_\delta = 1000.52$ and $y = 0.64$.

Again, all modes, apart from the fundamental, have decayed, which indicates the absence of any transient phenomena occurring inside the computational domain.

# BIBLIOGRAPHY


[1] John Anderson. *Hypersonic and High Temperature Gas Dynamics*. Reston, UNITED STATES: American Institute of Aeronautics and Astronautics, 2000.

[2] Brady P. Brown and Brian M. Argrow. "Application of Bethe-Zel'dovich-Thompson Fluids in Organic Rankine Cycle Engines". en. In: *Journal of Propulsion and Power* 16.6 (Nov. 2000), pp. 1118–1124.

[3] Gerd Brunner. "Applications of Supercritical Fluids". In: *Annual Review of Chemical and Biomolecular Engineering* 1.1 (2010), pp. 321–342.

[4] C-L Chang et al. "Hypersonic boundary-layer stability with chemical reactions using PSE". In: *28th Fluid Dynamics Conference*. 1997, p. 2012.

[5] Richard Courant et al. *On the partial difference equations of mathematical physics*. eng. New York: Courant Institute of Mathematical Sciences, New York University, 1956.

[6] A Dorodnitsyn. "Laminar boundary layer in compressible fluid". In: *Dokl. Akad. Nauk SSSR*. Vol. 34. 8. 1942, pp. 213–219.

[7] Kenneth Franko, Robert MacCormack, and Sanjiva Lele. "Effects of Chemistry Modeling on Hypersonic Boundary Layer Linear Stability Prediction". In: *40th Fluid Dynamics Conference and Exhibit*. Fluid Dynamics and Co-located Conferences. American Institute of Aeronautics and Astronautics, June 2010.

[8] Heath Johnson and Graham Candler. "PSE analysis of reacting hypersonic boundary layer transition". In: *30th Fluid Dynamics Conference*. 1999, p. 3793.

[9] Soshi Kawai. "Direct numerical simulation of transcritical turbulent boundary layers at supercritical pressures with strong real fluid effects". en. In: *54th AIAA Aerospace Sciences Meeting*. American Institute of Aeronautics and Astronautics, Jan. 2016.

[10] Oliver Kunz, ed. *The GERG-2004 wide-range equation of state for natural gases and other mixtures*. en. Als Ms. gedr. Fortschritt-Berichte VDI Reihe 6, Energietechnik 557. OCLC: 180749106. Düsseldorf: VDI-Verl, 2007.

[11] Lester Lees. "Laminar heat transfer over blunt-nosed bodies at hypersonic flight speeds". In: *Journal of Jet Propulsion* 26.4 (1956), pp. 259–269.

[12] Lester Lees and Chia-Chiao Lin. *Investigation of the Stability of the Laminar Boundary Layer in a Compressible Fluid*. en. National Advisory Committee for Aeronautics, 1946.

[13] Solomon Levy. "Effect of large temperature changes (including viscous heating) upon laminar boundary layers with variable free-stream velocity". In: *Journal of the Aeronautical Sciences* 21.7 (1954), pp. 459–474.

[14] Ian Lyttle and Helen Reed. “Sensitivity of Second-Mode Linear Stability to Constitutive Models within Hypersonic Flow”. In: *43rd AIAA Aerospace Sciences Meeting and Exhibit*. _eprint: https://arc.aiaa.org/doi/pdf/10.2514/6.2005-889. American Institute of Aeronautics and Astronautics.

[15] Leslie M Mack. *Boundary-layer linear stability theory*. Tech. rep. California Inst of Tech Pasadena Jet Propulsion Lab, 1984.

[16] M. R. Malik and E. C. Anderson. “Real gas effects on hypersonic boundarylayer stability”. In: *Physics of Fluids A: Fluid Dynamics* 3.5 (May 1991). Publisher: American Institute of Physics, pp. 803–821.

[17] Mujeeb R. Malik. “Hypersonic Flight Transition Data Analysis Using Parabolized Stability Equations with Chemistry Effects”. In: *Journal of Spacecraft and Rockets* 40.3 (2003). Publisher: American Institute of Aeronautics and Astronautics _eprint: https://doi.org/10.2514/2.3968, pp. 332–344.

[18] Ali Mani. “Analysis and optimization of numerical sponge layers as a nonreflective boundary treatment”. en. In: *Journal of Computational Physics* 231.2 (Jan. 2012), pp. 704–716.

[19] Olaf Marxen, Gianluca Iaccarino, and Thierry E. Magin. “Direct numerical simulations of hypersonic boundary-layer transition with finite-rate chemistry”. en. In: *Journal of Fluid Mechanics* 755 (Sept. 2014), pp. 35–49.

[20] Olaf Marxen et al. “A method for the direct numerical simulation of hypersonic boundary-layer instability with finite-rate chemistry”. en. In: *Journal of Computational Physics* 255 (Dec. 2013), pp. 572–589.

[21] Mark V Morkovin. *Critical evaluation of transition from laminar to turbulent shear layers with emphasis on hypersonically traveling bodies*. Tech. rep. MARTIN MARIETTA CORP BALTIMORE MD RESEARCH INST FOR ADVANCED STUDIES, 1969.

[22] Clifton H. Mortensen and Xiaolin Zhong. “Real-Gas and Surface-Ablation Effects on Hypersonic Boundary-Layer Instability over a Blunt Cone”. In: *AIAA Journal* 54.3 (2016). Publisher: American Institute of Aeronautics and Astronautics _eprint: https://doi.org/10.2514/1.J054404, pp. 980–998.

[23] Nora Okong’o and Josette Bellan. “Consistent Boundary Conditions for Multicomponent Real Gas Mixtures Based on Characteristic Waves”. en. In: *Journal of Computational Physics* 176.2 (Mar. 2002), pp. 330–344.

[24] Sergio Pirozzoli. “Generalized conservative approximations of split convective derivative operators”. en. In: *Journal of Computational Physics* 229.19 (Sept. 2010), pp. 7180–7190.

[25] Marco Pizzarelli. “The status of the research on the heat transfer deterioration in supercritical fluids: A review”. en. In: *International Communications in Heat and Mass Transfer* 95 (July 2018), pp. 132–138.

[26] T. J Poinsot and S. K Lelef. “Boundary conditions for direct simulations of compressible viscous flows”. en. In: *Journal of Computational Physics* 101.1 (July 1992), pp. 104–129.

[27] Muralikrishna Raju et al. “Widom lines in binary mixtures of supercritical fluids”. In: *Scientific reports* 7.1 (2017), pp. 1–10.

[28] Jie Ren, Song Fu, and Rene Pecnik. “Linear instability of Poiseuille flows with highly non-ideal fluids”. en. In: *Journal of Fluid Mechanics* 859 (Jan. 2019). Publisher: Cambridge University Press, pp. 89–125.

[29] Jie Ren, Olaf Marxen, and Rene Pecnik. “Boundary-layer stability of supercritical fluids in the vicinity of the Widom line”. en. In: *Journal of Fluid Mechanics* 871 (July 2019). Publisher: Cambridge University Press, pp. 831–864.

[30] Taraneh Sayadi, Curtis W. Hamman, and Parviz Moin. “Direct numerical simulation of complete H-type and K-type transitions with implications for the dynamics of turbulent boundary layers”. en. In: *Journal of Fluid Mechanics* 724 (June 2013), pp. 480–509.

[31] Hermann Schlichting and Klaus Gersten. *Boundary-layer theory*. Springer, 2016.

[32] Peter J. Schmid and Dan S. Henningson. *Stability and Transition in Shear Flows*. en. Applied Mathematical Sciences. New York: Springer-Verlag, 2001.

[33] Francesco Sciortino et al. “Line of compressibility maxima in the phase diagram of supercooled water”. In: *Physical Review E* 55.1 (1997), p. 727.

[34] Christian Stemmer, Marcel Birrer, and Nikolaus A. Adams. “Disturbance Development in an Obstacle Wake in a Reacting Hypersonic Boundary Layer”. In: *Journal of Spacecraft and Rockets* 54.4 (2017). Publisher: American Institute of Aeronautics and Astronautics _eprint: https://doi.org/10.2514/1.A33708, pp. 945–960.

[35] Kevin W Thompson. “Time dependent boundary conditions for hyperbolic systems”. en. In: *Journal of Computational Physics* 68.1 (Jan. 1987), pp. 1–24.

[36] Paul Vladuchick. *Smoke from a cigarette*. URL: https://www.flickr.com/photos/vladdythephotogeek/ (visited on 02/01/2021).

[37] Xiaowen Wang. “Non-Equilibrium Effects on the Stability of a Mach 10 Flat-Plate Boundary Layer”. en. In: *8th AIAA Theoretical Fluid Mechanics Conference*. Denver, Colorado: American Institute of Aeronautics and Astronautics, June 2017.

[38] Xingjian Wang and Vigor Yang. “Supercritical Mixing and Combustion of Liquid-Oxygen/ Kerosene Bi-Swirl Injectors”. In: *Journal of Propulsion and Power* 33.2 (July 2016). Publisher: American Institute of Aeronautics and Astronautics, pp. 316–322.

[39] B. Wasistho. *Spatial Direct Numerical Simulation of Compressible Boundary Layer flow*. en. 1997.

[40] B. Wasistho, B. J. Geurts, and J. G. M. Kuerten. “Simulation techniques for spatially evolving instabilities in compressible flow over a flat plate”. en. In: *Computers & Fluids* 26.7 (Sept. 1997), pp. 713–739.